



HAL
open science

Conception and realization of spectral sorters

Ujwol Palanchoke

► **To cite this version:**

Ujwol Palanchoke. Conception and realization of spectral sorters. Optics / Photonic. Université Grenoble Alpes, 2015. English. NNT: 2015GREAT018 . tel-01179143

HAL Id: tel-01179143

<https://theses.hal.science/tel-01179143>

Submitted on 21 Jul 2015

HAL is a multi-disciplinary open access archive for the deposit and dissemination of scientific research documents, whether they are published or not. The documents may come from teaching and research institutions in France or abroad, or from public or private research centers.

L'archive ouverte pluridisciplinaire **HAL**, est destinée au dépôt et à la diffusion de documents scientifiques de niveau recherche, publiés ou non, émanant des établissements d'enseignement et de recherche français ou étrangers, des laboratoires publics ou privés.



leti

UNIVERSITÉ
GRENOBLE
ALPES

THÈSE

Pour obtenir le grade de

DOCTEUR DE L'UNIVERSITÉ GRENOBLE ALPES

Spécialité : **Optique et Radiofréquences**

Arrêté ministériel : 7 août 2006

Présentée par

Ujwol PALANCHOKE

Thèse dirigée par **Jean-Louis COUTAZ** et
codirigée par **Anne SENTENAC**

préparée au sein du **Laboratoire d'électronique et de technologie de
l'information (Leti), CEA Grenoble**
dans **l'École Doctorale d'Electronique, Electrotechnique,
Automatique, Traitement du Signal (EEATS)**

Conception et Réalisation de Trieur Spectraux pour l'Imagerie

Thèse soutenue publiquement le **9 janvier 2015**,
devant le jury composé de :

M. Xavier LETARTRE

Directeur de recherches au CNRS, INL Lyon, Rapporteur et Président du jury.

M. Riad HAIDAR

Ingénieur (HDR) à l'ONERA, Palaiseau, Rapporteur.

M. Jean-Louis COUTAZ

Professeur, IMEP-LAHC, Université de Savoie, Directeur de thèse, Membre.

Mme Anne SENTENAC

Directeur de recherches au CNRS, Institut Fresnel, Marseille, Co-directrice de
thèse, Membre.

M. Jérôme FAVIER

Ingénieur à ULIS, Veurey-Voroize, Membre.

M. Salim BOUTAMI

Ingénieur CEA-LETI, Grenoble, Encadrant de la thèse, Membre.

M. Flavien HIRIGOYEN

Ingénieur, ST Microelectronics, Crolles, Invité.

M. Serge GIDON

Ingénieur CEA-LETI, Co-encadrant de la thèse, Grenoble, Invité.



© Copyright by Ujwol Palanchoke 2015

All Rights Reserved

Dedicated to my school teacher " Kabita Yonzen"

List of Publications

List of Patent Deposited

1. U. Palanchoke, S. Boutami and J. Hazart, “Device for spectral filtering in the visible and infrared regions”, FR patent 12 57823 (2012), EP 2698654 A1 (2014), US 20140049812 A1 (2014)
2. U. Palanchoke, S. Boutami and S. Gidon, “Capteur photosensible”, FR patent 14 58128 (2014)
3. Palanchoke Ujwol, J.L Ouvrier-Buffet, S. Boutami, JJ. Yon, “Matrices de Bolomètres Sélectifs à Constante de Temps Thermiques Réduites”, FR patent 14 51091 (2014)

List of Conference Proceedings

1. Ujwol Palanchoke, Salim Boutami and Jerome Hazart, " CMOS-compatible metallic nanostructures for visible and infrared filtering," Proc. SPIE 8994, Photonic and Phononic Properties of Engineered Nanostructures IV, 89940Y (2014)
2. Ujwol Palanchoke, Salim Boutami, Serge Gidon, “Tailoring multi spectral absorption using CMOS compatible MIM resonator,” OPTRO, 2956084, (2014)

Abstract

The advancement and scaling effect in complementary metal oxide semiconductor (CMOS) and micro-electro-mechanical system (MEMS) technology has made possible to make smaller image sensors with higher density of imaging pixels to respond at the demand of low cost imagers. Generally, the higher pixel density in imaging system is achieved by shrinking the size of each pixel in an array. The shrinking of pixel dimension however deteriorates the optical efficiency and therefore impose the tradeoff between the performance and minimum achievable pixel size. As the pixel size continues to shrink and approach the dimensions comparable to the wavelength, the spectral separation techniques used in current generation imaging system should be revised and new design methodologies have to be explored. This dissertation explored different techniques that could be used to efficiently sort the band of different wavelengths, mainly in far-infrared ($8\mu m - 12\mu m$) and visible ($0.4\mu m - 0.7\mu m$) spectrum in different spatial locations. We introduced the concept of spectral sorting based on normalized optical efficiency (NOE). For given number of pixels (N) or detectors, we define the phenomenon of sorting if NOE of individual pixels, considering incidence power from all pixel domain, is greater than $1/N$. First we study differently sized optical patch antenna to efficiently sort the infrared light in different spatial locations using numerical techniques. Using array of such antennas we find the near perfect absorption of multiple wavelengths in infrared spectrum. The antenna arrays are fabricated and characterized in CEA-LETI platform to validate our study. We also report our study on using two differently sized Metal-Semiconductor-Metal

(MSM) nanostructures to achieve absorption higher than 50% in silicon detector for visible spectrum. Finally we present our study on grating based dielectric multi-layer structure for sorting of visible light which could enable to shrink the pixel size of visible imaging system to submicron dimension. We derived the comprehensive design strategy of such sorting structure and present the sorting structure designed to achieve optical efficiency as high as 80% in pixel size of as less as $0.5\mu m$.

Acknowledgement

I would like to thank all those who has supported me during the period of my thesis work and stay in Grenoble.

I would like to thank Dr. Jérôme Hazart for introducing me with the research topic and supervising me during first year of my research work in CEA-LETI, Grenoble. His suggestions during weekly discussion have been crucial step for understanding various numerical techniques. I would like to thank Serge Gidon, for accepting to be my supervisor during last two years of my research work. His suggestions and critical comments on the device design and results was crucial for the understanding of spectral sorting devices.

I would like to express my gratitude to my co-supervisor Dr. Salim Boutami for his guidance, constructive ideas, suggestions and continuous support during my work in LETI. Discussion on physics and device modeling with Dr. Boutami have provided a deeper insight into my understanding of spectral sorting. I would like to thank him especially for letting me free to explore different design ideas.

I would like to thank Pr. Jean-Louis Coutaz and Dr. Anne Sentenac for accepting to be my PhD thesis directors. I would like to thank especially Dr. Anne Sentenac for her discussion on physics of visible color sorting and letting me work in her lab at Institut Fresnel, Marseille.

My special thank goes to:

1. Wilfried Rabaud for involving me in project MIMBOPOP.

2. Stéphane Pocas for fabricating the infrared antenna array and SEM images.
3. Jean-Louis Ouvrier Bouffet and Jean-Jacques Yon for their discussion on technical and modeling issues on antenna arrays.
4. Névine Rochat for helping with the characterization of antenna arrays.

I would like to thank all my colleagues at LCNA lab in CEA-LETI, especially Yann Lee and Fabien Laulagnet for tolerating my bad singing and whistling for two long years, Vincent Reboud, Boris Caire Remonnay, Clément Chauveau and Audrey Bastard for providing me the escape route to refreshment by organizing a “pint in bar” when I desperately needed a refreshment. I would like to thank all my friends in Grenoble, for their help and making my life much easier. I would also like to thank all my friends in Nepal, for their support and late night skype conferences, which made me feel home. I would like to thank my cousin sister Shree Shrestha Thapa for supporting and listening me during my time of frustrations.

Last but not the least, I would like to express special gratitude to my parents Navaraj Palanchoke and Sahanshila Palanchoke, my grandmother Tulsimaya Palanchoke, my brother Prajwol Palanchoke and sister Soniya Palanchoke for their support throughout my entire study.

Contents

List of Publications	iii
Abstract	iv
Acknowledgement	vi
1 Introduction	1
1.1 Imaging technology and trend of array format	1
1.2 Small pixel size and optical efficiency	3
1.3 Concept of Spectral Sorting	6
1.4 Thesis Outline	8
2 Numerical study of optical patch antennas for infrared sorting	9
2.1 State of Art	9
2.2 Study of Optical patch antenna	11
2.2.1 Modeling of patch antenna	11
2.2.1.1 Resonance wavelength and field enhancement	11
2.2.1.2 Antenna effective cross section area	14
2.2.1.3 Antenna absorption at resonance	18

2.2.2	Numerical study of Single patch antenna	20
2.2.3	Antenna mutual coupling and its effect on absorption property	24
2.3	Spectral sorting and broadband absorption using patch antenna	28
2.3.1	Spectral Sorting using patch antenna array	28
2.3.2	Multi Spectral Absorption using periodic patch antenna array	32
2.3.2.1	Angular response periodic patch antenna array	37
2.4	Conclusion	40
3	Fabrication and Characterization of optical patch antenna array	41
3.1	Fabrication of optical patch antenna array	41
3.2	Characterization of antenna arrays	43
3.3	Dimensional variation and spectral response	46
3.3.1	Variation in Patch size	47
3.3.2	Rounding of patch edge	49
3.3.3	Variation in antenna stack slope	52
3.3.3.1	Target: Bottom width (W_{bottom})	53
3.3.3.2	Target: Top width (W_{top})	57
3.3.3.3	Target: Top width(W_{top}), different angles for etched top metal and excess core material	61
3.4	Comparison of realistic antenna modeling and experimental result . .	64
3.5	Conclusion	68
4	Sorting in Visible	69
4.1	Introduction	69

4.2	Metallic structures for sorting of visible light	71
4.2.1	Metal-Semiconductor-Metal Array on transparent substrate	71
4.2.2	Metal-Semiconductor-Metal Array with reflector	75
4.3	Dielectric based structure for sorting of visible light	79
4.3.1	Antireflection property of multilayer dielectric on Silicon	80
4.3.2	Grating based anti-reflection structure	85
4.3.3	Grating assisted sorting of visible light	91
4.4	Conclusion	101
5	Conclusion	102
A	Antenna Fundamentals	105
A.1	Antenna and Electromagnetic Radiation	105
A.2	Antenna Radiation Parameters	109
A.2.1	Radiation pattern	109
A.2.2	Antenna Directivity	110
A.2.3	Antenna Gain	111
A.2.4	Friis transmission equation and antenna aperture	112
A.2.5	Antenna Bandwidth and Quality factor	114
B	Dielectric Properties of Metal: Drude model	115
C	Expiremental Setup-Total Reflection	117
D	Review: Far Field Spectral Sorting	118
D.1	Fundamental color sorting- complementary color detection: Binary Phase Grating	118

D.2 Fundamental color sorting-Fundamental color detection: Multilevel	
Phase Grating	124
E Transfer Matrix Method	132
Bibliography	138

List of Figures

1.1	Pixel arrays (a) RGB Bayer's array in visible imaging system (reproduce from ref.[1] by Vladislav Jovan Jovanov), (b) bolometer pixel array in infrared imaging system	1
1.2	Trend of array format for different imaging technology for visible and infrared spectrum with respect to the complexity of silicon IC technology (taken from Ref. 2)	2
1.3	Incidence area considered for calculating NOE, (a) individual pixel (b) domain of two pixels	3
1.4	Reduction in pixel size	5
1.5	Spectral sorting of light incident on adjacent pixel to pixel of interest	7
2.1	State of Art 1D MIM sorter (a)taken from [2] (b) taken from[3] . . .	10
2.2	(a) Patch antenna with metal ground plate, with insulator width W, and height h. top metal thickness greater than skin depth is considered for the analysis (b) equivalent circuit model of patch antenna	12
2.3	Schematic for modeling antenna with coupled mode theory	15
2.4	Normalized cross section area of patch antenna resonating at $8.2\mu\text{m}$.	18
2.5	Two antennas with overlapped cross sections	20

2.6	(a) top view of simulation region (b) side view of simulation region (c) resonance wavelength and normalized absorption as a function of patch width (d) scattering cross section area and absorption cross section area normalized to patch area	22
2.7	Normalized cross section area and absorption as a function of spacer height of an isolated antenna with patch width (a) $1.2m$ (b) $1.4m$ and (c) $1.6m$	23
2.8	Absorption spectra of an antenna using optimal spacer thickness for given patch width (shown in inset). $4\mu m \times 4\mu m$ illumination spot size is used for calculation.	24
2.9	Patch antenna with patch width $1400nm$ arranged in different ar- rangement (a) single patch antenna at center ($S1$), (b) cross arrange- ment ($S2$), (c) plus arrangement ($S3$) with antenna-antenna separa- tion distance Sd' (d) absorption spectra of arrangement $S1$, $S2$ and $S3$	25
2.10	Absorption spectrum for different Sd' (a) antenna arrangement $S2$ (b) antenna arrangement $S3$	26
2.11	Antenna with width $W1$ surrounded by another antenna with width $W2$ (a) Cross arrangement (b) Plus arrangement, Absorption spectra with (c) $W1 : 1240nm$ $W2 : 1150nm$ (d) $W1 : 1400nm$ $W2 : 1200nm$.	27
2.12	(a) patch antennas with different width arranged in square lattice with center to center distance P' (b) absorption spectra of antenna array shown in (a) with $W1 : 1600nm$ $W2 = W4 : 1220nm$ $W3 :$ $1400nm$ and $P' : 2000nm$, magnetic field map corresponding to resonance wavelength of (c) $W2$ and $W4(\lambda = 8.5\mu m)$, (d) $W3(\lambda =$ $9.8\mu m)$ and (e) $W1(\lambda = 11.5\mu m)$	30

2.13	(a) patch antennas with different width arranged in square lattice with center to center distance P' (b) absorption spectra of antenna array shown in (a) with $W1 : 1685nm$ $W2 : 1240nm$, $W3 : 1370nm$, $W4 : 1150nm$ and $P' : 2250nm$, magnetic field map corresponding to resonance wavelength of (c) $W4(\lambda = 8.2\mu m)$, (d) $W2(\lambda = 8.9\mu m)$,(e) $W3(\lambda = 9.8\mu m)$ and (f) $W1(\lambda = 12.0\mu m)$	31
2.14	Unit cell of periodic antenna array considered for multi spectral absorption in $7 - 14m$ infrared range (a) three spectra, (b) four spectra	33
2.15	Absorption as a function of local period Pl (a) three spectra (b) four spectra.	34
2.16	Absorption as a function of a-Si spacer thickness (a) three spectra (b) four spectra	34
2.17	Absorption spectra for (a) $3CS$ (b) $4CS$ using optimal parameters . .	36
2.18	(a) Representation of polar(θ) and azimuth (φ) angle of incidence, (b) Absorption of antenna arrangement $3CS$ as a function of wavelength and polar (θ) angle of incidence for an azimuth angle $\varphi = 0^\circ$, (c-d) Absorption spectra for various polar angles (c) $\theta = 60^\circ$ (d) $\theta = 80^\circ$ and azimuth angles $\varphi = 0^\circ, 20^\circ, 40^\circ, 60^\circ, 80^\circ$	38
2.19	Absorption of antenna arrangement $4CS$ as a function of wavelength and polar (θ) angle of incidence for an azimuth angle $\varphi = 0^\circ$,(a) TM polarization, (b) TE polarization, (c-f) Absorption spectra for various polar angles (c, d) $\theta = 20^\circ$ (e, f) $\theta = 60^\circ$ and azimuth angles $\varphi = 0^\circ, 20^\circ, 40^\circ, 60^\circ, 80^\circ$ for (c, e) TM polarization, (d, f) TE polarization	39
3.1	Basic fabrication Steps	42

3.2	(a) Tilted SEM image of fabricated antenna array 3CS, (b) cross section SEM image of fabricated antenna	43
3.3	Sketch of experimental setup used for characterization of antenna array	44
3.4	Measured and computed absorption spectra of antenna array (a) 3CS, (b) 4CS for both TE and TM polarization	45
3.5	Measured absorption spectra for different incidence angles: 20°, 22° and 25° for TE and TM polarization, (a) 3CS, (b) 4CS	45
3.6	(a) Unit cell of periodic antenna array 3CS ,(b) Conceptual diagram showing the patch size variation of individual patch antenna in periodic array 3CS ,(c) Absorption as a function of Δ and wavelength for antenna array 3CS, (d) Absorption as function of wavelength for different Δ . The spectrum corresponds to the vertical cross cuts shown in (c).	48
3.7	(a) Individual structures which creates the rounded patch (b) Top view of rounded patch showing the center of cylindrical patch edge and its trajectory (c-d) top view of patch for different scaling factor r	50
3.8	Absorption as a function of scaling factor r and wavelength (a) for 3CS (c) 4CS for TM polarization of incidence wave (e) 4CS for TE polarization of incidence wave, Absorption as a function of wavelength for various scaling factor ($r = 0, 0.5, and 1$)(b) for 3CS (d) 4CS for TM polarization of incidence wave (f) 4CS for TE polarization of incidence wave	51
3.9	Schematic for bottom width target (b) absorption as a function of wavelength of periodic antenna width patch width $W : 1400nm$ and period $P : 2000nm$ (c) absorption as a function of wavelength of antenna array 3CS for different slope angles	54

3.10	(a) $\left(1 - \frac{2h_{ins}\tan(\theta)}{W_{bottom}}\right)$ and (b) $\frac{n'_{eff}}{n_{eff}}$ as a function of slope angle (θ) for various patch widths ($W : 1400nm, 1500nm$ and $1600nm$)	56
3.11	(a) Schematic for top width target (b) absorption as a function of wavelength of periodic antenna width patch width $W : 1400nm$ and period $P : 2000nm$ (c) absorption as a function of wavelength of antenna array $3CS$ for different slope angles	58
3.12	(a) $\left(1 - \frac{2h_{ins}\tan(\theta)}{W_{top}+2h_{ins}\tan(\theta)}\right)$ and (b) $\frac{n'_{eff}}{n_{eff}}$ as a function of slope angle (θ) for various patch widths ($W : 1200nm, 1300, 1400nm$)	60
3.13	Schematic for top width target with different slope angle for core material and top metal patch (b) absorption as a function of wavelength of antenna array $3CS$ for various metal slopes ($\theta_m : 40^\circ, 60^\circ, 80^\circ$) with fixed core slope ($\theta_h : 20^\circ$) (c) metal thickness at the edge of antenna patch normalized to designed metal thickness (h_{umet}) for various metal slopes ($\theta_m : 20^\circ, 40^\circ, 60^\circ, 80^\circ$)	62
3.14	Absorption as a function of wavelength of antenna array $3CS$ for various core slopes ($\theta_h : 10^\circ, 20^\circ, 40^\circ$) with fixed metal slope ($\theta_m : 70^\circ$)	63
3.15	(a) Cross section of antenna stack showing the slanted side faces of the stack, (b) Measured and computed absorption of $3CS$ with more realistic model including slant angles in faces of antenna stack, patch and stack dimension variation and $a - Si$ refractive index error of -5%	65
3.16	(a) Measured, specular and total absorption and computed absorption spectra of $3CS$ with realistic model, (b) measurement from the antenna array when source is blocked	66
3.17	(a) Black body radiation (BBR) normalized to maximum radiation at $8m$. 24% and 14% of normalized black body radiation is also shown. (b) Absorption spectrum fitted assuming black body radiation at $8m$.	67

4.1	(a) Metal-Semiconductor-Metal array on SiO_2 substrate, (b) Absorption as a function of $S1$ and wavelength for constant $S2$ and $h_{(a-si)} = 150nm$, (c) Absorption of different layer of MSM structure as a function of wavelength for $S1 : 45nm, S2 : 70nm$	72
4.2	(a) Absorption in $D1$ and $D2$ as a function of wavelength for different core thickness, (b) Absorption as a function of wavelength for different MSM layers along with total absorption of MSM array with core thickness of $300nm$ and $S1 : 45nm, S2 : 70nm, h_{met} : 40nm, h_{buffer} : 10nm$ and $Pl : 150nm$, (c) Absorption in metal layers as a function of wavelength for different core thickness, (d) Total transmission and reflection spectrum of MSM array as a function of wavelength for various core thickness	73
4.3	(a) MSM stack array with reflector layer, (b) Absorption as a function of wavelength and h_{cavity} for core thickness of $150nm$, (c) Absorption of different stack layer and reflector with $h_{cavity} : 150nm$	76
4.4	Comparison of absorption in silicon layer in MSM array with and without reflector	77
4.5	(a) Absorption in metal layers as a function of wavelength for different cavity lengths, (b) Comparison of absorption in metal layers of MSM array with and without reflecting surface. The dimensions considered for MSM array are: $S1 : 45nm, S2 : 70nm, h_{met} : 40nm, h_{buffer} : 10nm, h_{a-si} = 150nm$ and $Pl : 150nm$	78
4.6	(a) Reflection as a function of wavelength of bulk silicon, (b) Real and imaginary part of refractive index of silicon as a function of wavelength	80

4.7	(a) Two layer dielectric structure on top of Silicon, with individual thickness of $110nm$, Reflection as a function of wavelengths and refractive index of top layer (n_{gt}) with index of second layer (b) $n_{IL} = 1.5$ and (c) $n_{IL} = 2.0$	81
4.8	Reflection of two layer system with index of first layer $n_{gt}2.1$ and different indices for second layer	82
4.9	(a) Unit cell of the periodic arrangement of layered structures designed to minimize reflection at different wavelengths. Absorption spectra of silicon under the layered system with first- and second-layer made of material with indices (b) $n_{gt}2.1$ and $n_{IL-1} : 2.0$, (c) $n_{gt} : 2.1$ and $n_{IL-2} : 1.5$ for different sizes (Px) of the structure. . . .	84
4.10	(a) Homogenization of grating with subwavelength period. The effective index of homogenous layer is calculated using effective medium theory. (b) Effective index as a function of wavelength for different grating widths with grating refractive index of 2.5 and period $250nm$	86
4.11	(a) Two layer system with grating as first layer, (b) effective refractive index of the grating layer calculated using effective medium theory. .	87
4.12	Comparison of reflection spectra for two layer system with homogenous first layer and grating first layer calculated using TMM model and RCWA method with homogenous second layer (a) $n_{IL} = 1.5$ and (b) $n_{IL} = 2.0$ deposited on silicon, (c) $n_{IL} = 1.5$ and (d) $n_{IL} = 2.0$ deposited on homogenous material with refractive index 1.5	89
4.13	Different configuration of grating based antireflection structures (a) with grating stub on top of second layer of each antireflection structure (b) with atleast one grating stub on top of second layer of each structure and one on top of junction of second layer	92

4.14	Absorption as a function of wavelength for different structure sizes ($Px : 0.5m-5m$) in the silicon under (a) $n_{IL-1} : 1.5$ and (b) $n_{IL-2} : 2.0$ for configuration $C1$	93
4.15	Absorption as a function of wavelength for different structure sizes ($Px : 0.5m-5m$) in the silicon under (a) $n_{IL-1} : 1.5$ and (b) $n_{IL-2} : 2.0$ for configuration $C2$	93
4.16	Electromagnetic power dissipation in silicon as a function of spatial position for configuration $C2$ at wavelength of (a) $520nm$ and (b) $420nm$. The red arrows indicates the power flow time average in the structure	95
4.17	(a) Three layer structure for selective antireflection of light, in which the thickness and index of first, second and third layer is denoted as d_1 and n_1 , d_2 and n_2 , d_3 and n_3 , respectively (b) Reflection as a function of wavelength of the three layer antireflection structure designed for blue-green light, with $d_1 : 60nm$, $d_2 : 100nm$ and $d_3 : 50nm$ and $n_1 : 2.1$, $n_2 : 1.5$ for blue, $n_2 : 2.0$ for green light and $n_3 : 1.5$ (c) Reflection as a function of wavelength of the three layer antireflection structure designed for green-red light, with $d_1 : 90nm$, $d_2 : 100nm$ and $d_3 : 50nm$ and $n_1 : 2.1$, $n_2 : 1.5$ for green, $n_2 : 2.0$ for red light and $n_3 : 1.5$	97
4.18	(a) Periodic arrangement of blue and green antireflecting structure ($B1$ and $G1$) with first grating layer, (b) Absorption spectra of $B1$ and $G1$ represented by blue and green curve respectively. Power dissi- pation in silicon as a function of spatial position at wavelength of (c) $480nm$ and (d) $540nm$ for periodic arrangement of $B1$ and $G1$ respectively	99

4.19 (a) Periodic arrangement of green and red antireflecting structure (<i>G2</i> and <i>R1</i>) with first grating layer, (b) Absorption spectra of <i>G2</i> and <i>R1</i> represented by blue and green curve respectively. Power dissipation in silicon as a function of spatial position at wavelength of (c) $540nm$ and (d) $620nm$ for periodic arrangement of <i>G2</i> and <i>R1</i> respectively	100
A.1 (a) electric dipole (b) electric dipole antenna fed with alternating current (c) magnetic dipole with current loop of area A	106
A.2 Radiating object of arbitrary volume V with source \vec{J}	108
A.3 (a) Omni directional antenna pattern (b) Directional antenna pattern	110
A.4 Transmitting and receiving antennas separated by distance R	112
C.1 Experimental setup for total reflection measurement of antenna array	117
D.1 Binary grating structure for beam splitting	119
D.2 Diffraction efficiency of grating with $h = 1350nm$, $P = 10m$ and $f = 0.5$	120
D.3 Diffraction angle of first order diffracted light as a function of grating period	121
D.4 Diffraction efficiency of grating with (a) $P : 800nm$, $h : 2884nm$, (b) $P : 1000nm$, $h : 3522nm$, (c) $P : 1200nm$, $h : 4374nm$ (d) mosaic to detect complementary colors	122
D.5 Color detection scheme for complimentary color (a) Combination <i>G1</i> and <i>G2</i> , (b) Combination of <i>G1</i> and <i>G3</i>	123
D.6 3- level color separation grating (two phase levels + ground level) . .	124

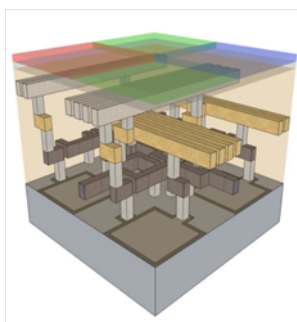
D.7	(a) Diffraction efficiency as a function of wavelength for central diffraction orders, -1, 0, and +1. Diffraction efficiency as a function of grating period, (b) TE illumination (c) TM illumination.	126
D.8	(a) Single wave splitter (b) multiple wave splitter	128
D.9	Maximum incidence angle for efficient color separation	129
E.1	Multilayer structure with complex refractive index. The electric field is divided to forward (with + sign) and backward (with - sign) components in TMM	132

Chapter 1

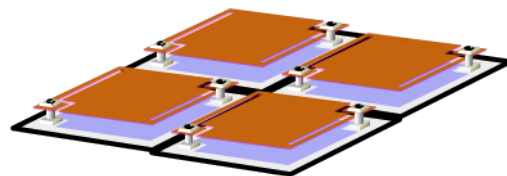
Introduction

1.1 Imaging technology and trend of array format

Imaging system in visible and infrared regime has found widespread use in both civilian and military applications. In visible imaging system, the color filters Green, Blue or Red are arranged regularly in specific format called Bayer's pattern as shown in figure 1.1 (a). Each filters are dedicated to individual sensors or photo detectors which converts the transmitted light from filter into electrical signal. These electrical signals are then processed to generate digital images.



(a)



(b)

Figure 1.1: Pixel arrays (a) RGB Bayer's array in visible imaging system (reproduce from ref.[1] by Vladislav Jovan Jovanov), (b) bolometer pixel array in infrared imaging system

The combination of filter and photo detector is called pixel and the regular array of filter and photo detector is known as pixel array. Similarly, in infrared imaging system, thermal sensors or bolometers are arranged regularly to form a pixel array as shown in figure 1.1 (b). The electronics embedded in the pixel generates electrical signal which is processed to form a digital infrared images.

Over last few decades the pixel size in both visible and infrared imaging system has decreased significantly because of the advancement and scaling effect in Complementary metal oxide semiconductor (CMOS) and micro-electro-mechanical system (MEMS) technology. [4, 5, 6, 7, 8].

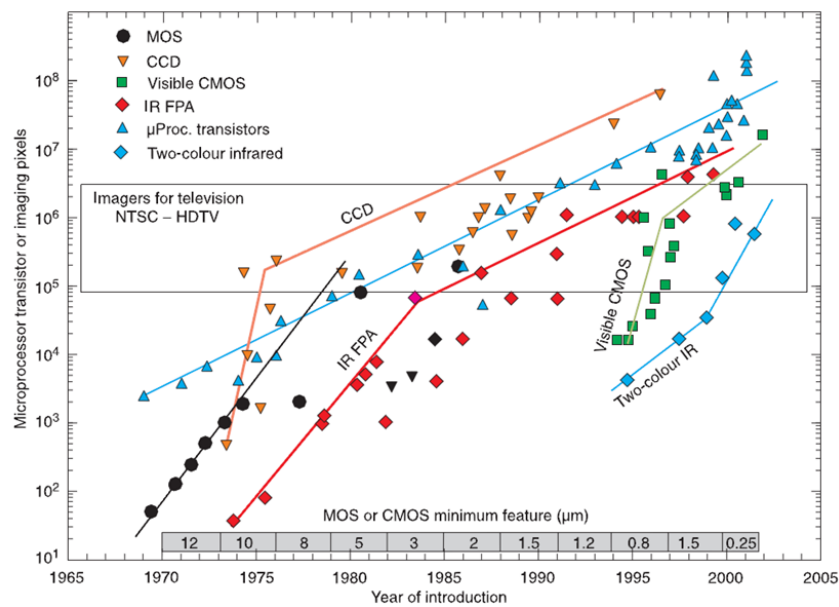


Figure 1.2: Trend of array format for different imaging technology for visible and infrared spectrum with respect to the complexity of silicon IC technology (taken from Ref. 2)

The number of pixels in imaging system has grown in proportion to the ability of silicon integrated circuit (IC) technology to read and process the array signals and has paralleled the development of electronic structure [5, 6] as can be seen in figure 1.2. The pixel size in current generation visible and infrared imaging device has decreased to $1.1\mu m$ and $17\mu m$ respectively allowing to manufacture compact

camera with higher pixel density. The pixel size will continue to decrease as the demand for imaging systems with higher pixel density increases.

1.2 Small pixel size and optical efficiency

One of the measure to quantify the performance of optical pixels is normalized optical efficiency (NOE) [9, 10]. It is defined as the ratio of optical power available or absorbed by photo detector to total power incidence on the pixel area of interest. Normalized optical efficiency is limited by geometrical parameters like detector fill factor (FF), which is the ratio of actual detector size to pixel size, and area of imaging pixel (A). For visible imaging system, NOE also depends on transmission efficiency (η) of color filters used. Let's consider two neighboring blue and green pixel of Bayer's pattern as shown in figure 1.3.

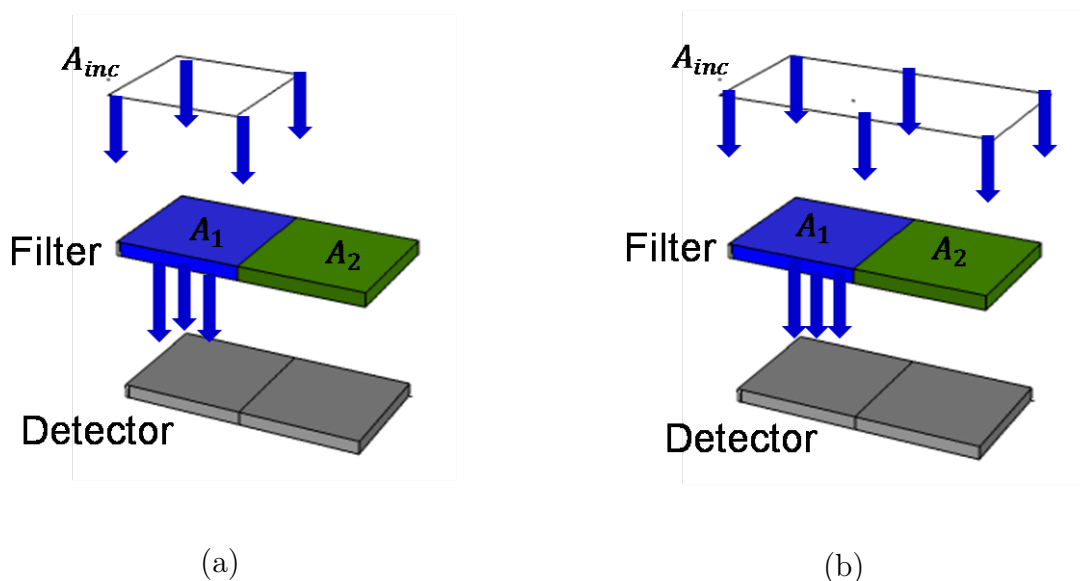


Figure 1.3: Incidence area considered for calculating NOE, (a) individual pixel (b) domain of two pixels

First, we consider incidence area above one pixel A_{inc} , A_1 physical area of blue pixels shown in figure 1.3 (a), FF the detector fill factor (ratio of actual detector size to pixel size) and η_{blue} the transmission efficiency of blue filter used, then for incidence

power P_{inc} in the pixel at corresponding spectral bandwidth, we can approximate the optical efficiency as:

$$NOE_{blue} = \frac{P_{D1}}{P_{inc}} = \frac{FF \times A_1}{A_{inc}} \times \eta_{blue} \quad (1.1)$$

In ideal case, where detector size is same as pixel size ($FF = 1$) and incidence area is equal to physical area of blue pixel ($A_1 = A_{inc}$), and the transmission efficiency of filters $\eta_{blue} = 1$, the normalized optical efficiency of pixel is:

$$NOE_{blue} = 1 \quad (1.2)$$

However, if we consider the incidence area to be the sum of area of blue and green pixels as shown in figure 1.3 (b) where we consider the incidence power over two pixel domain ($A_{inc} = A_1 + A_2$) then NOE given in 1.1 can be rearranged as:

$$NOE_{blue} = \frac{P_{D1}}{P_{inc}} = \frac{A_1}{A_1 + A_2} \times \eta_{blue} \quad (1.3)$$

Here we consider detector $FF = 1$. Considering same pixel dimensions for *Blue* pixel and *Green* pixel ($A_1 = A_2$), the maximum achievable NOE for arrangement shown in figure 1.3(b) with $\eta_{blue} = 1$, is given by:

$$NOE_{blue} = \frac{1}{2} \quad (1.4)$$

Similarly, if we consider the green pixel, the maximum achievable normalized optical efficiency would be $NOE_{green} = \frac{1}{2}$. In general, if we consider the incidence power in spectral region of interest from N-number of surrounding pixels (or detectors) to evaluate the efficiency of single pixel, then the maximum optical efficiency for that pixel is given by:

$$NOE_{1,2\dots N} = \frac{1}{N} \quad (1.5)$$

We see that, the NOE depends on physical area of pixels and incidence area considered for evaluation of NOE. One can argue that, when pixel size decrease from $5\mu m$ to $1\mu m$ as shown in figure 1.4, NOE would remains constant as the physical area decreases proportionally. However, the important thing to understand is that, the number of photon available to detector is much lesser than that for pixels with larger sizes.

For example, if we consider imaging pixels to be square shaped, reducing the pixel size from $5\mu m$ to $1\mu m$, as shown in figure 1.4, will reduce the optically active area by 25 fold. The decrease in optically active area will reduces the number of photons available to photo detector. Also, loss associated with filters or spectral selectors, lower fill factor of detectors, results in lower NOE of imaging pixels. It is therefore more challenging to maintain the acceptable SNR and DR in imaging system with small pixel. The signal to noise ratio (SNR) and dynamic range (DR) of imaging system will decrease as the pixel size decreases [4, 7, 8, 11, 12, 13, 14] leading to poor image quality.

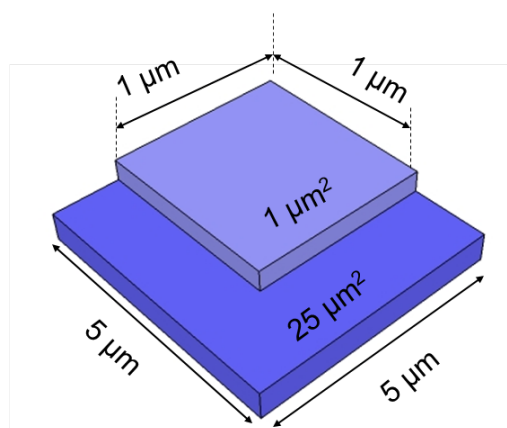


Figure 1.4: Reduction in pixel size

As the pixel size continues to shrink and approach the dimensions comparable to the wavelength of interest, the performance of conventional system starts to severely deteriorate [4, 7, 8, 11, 12, 13, 14]. The concern for imaging systems with small pixel dimension is how to increase the number of photons available to detector, so that it could maintain acceptable signal quality or image quality. Therefore, the spectral separation techniques used in current generation imaging system should be revised and new design methodologies have to be explored. Different studies has been done and design optimizations has been proposed to address these issues [15, 10, 16, 17, 1], in conventional CMOS visible imaging systems utilizing color filters, with pixel size as small as $1.1\mu m$. For example, in [15] the author use the microscale plate-like structure based on near field deflection to split colors from white light to increase number of photons available to the detectors. In [10] the optical efficiency of pixel is increased by utilizing light guiding structures between filter and detector.

1.3 Concept of Spectral Sorting

In previous section we discuss about the issues with small pixel sizes. The major issue regarding small pixel is that there is not enough photons available to detectors so that imaging system could maintain acceptable signal to noise ratio to produce good image quality. Except the optical efficiency and signal to noise ratio there would be electrical issues with small pixel sizes, which we do not cover in this thesis. The thesis deals with different ideas and concepts that could be useful to increase number of photons in photo detectors in imaging systems. We discuss in previous section that, the optical efficiency of small pixel would remain constant compared to their larger pixel counterpart, given that the filter efficiency remains constant for both pixel sizes and the dimension scaling of pixel from larger size to smaller size is proportional to all the pixels in the array. On doing so, we find that maximum optical efficiency (ideal) that could be achieved in any pixel is $\frac{1}{N}$ if incidence power

is considered from N number of pixels. However, the transmission efficiency of visible filters or efficiency of spectral selector is generally less than 100% resulting in decrease in overall optical efficiency of a pixel. If we could imagine some kind of structure, optical antenna for example, which could be embedded in filters or placed directly on detectors, that enable to route some lights incident on adjacent pixels as shown in figure 1.5 then it might be possible to achieve NOE of pixel greater than $\frac{1}{N}$.

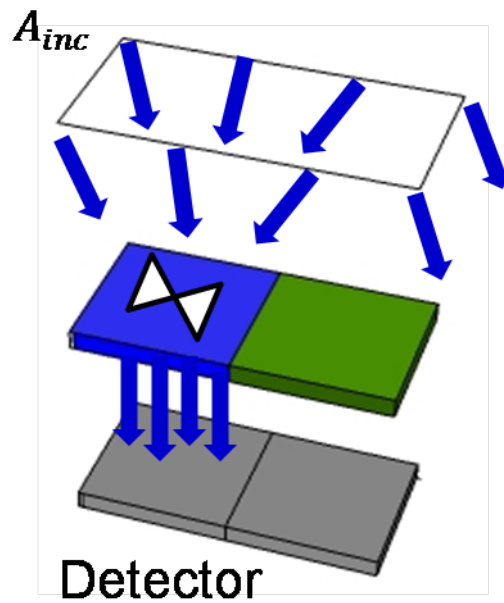


Figure 1.5: Spectral sorting of light incident on adjacent pixel to pixel of interest

The normalized optical efficiency larger than $\frac{1}{N}$ ($NOE > \frac{1}{N}$) for a pixel could be then be defined as the necessary condition of spectral sorting, since this requires routing of incidence wavelength to pixel of interest. Study has been made to achieve sorting of visible light using surface corrugation around nano holes made in metallic sheet and using bimetallic nano antennas [16, 17]. Also different studies has been made on optical patch antennas for sorting of infrared radiations [18, 2, 3, 19]. Unlike filters which have effective collection area limited to its physical size, metallic antennas could have larger effective collection area compared to its physical size during resonance. The larger interaction volume of an antenna can route the incident

wave to pixel of interest which could therefore increase the NOE of the pixels. This makes metallic antennas good candidates for spatially sorting light with different wavelengths (or energies).

1.4 Thesis Outline

In this thesis, we explore different concepts to efficiently separate or sort the specific band of wavelengths in small volume or area, which in turns could be used to design optically efficient pixels in imaging system. We focus our study on CMOS compatible structures for sorting of far-infrared ($8\mu m - 12\mu m$) and visible ($0.4\mu m - 0.7\mu m$) spectrum which are mostly used for thermal and color imaging respectively.

In Chapter 2, we study CMOS compatible metallic patch antennas to efficiently sort far infrared spectrum. We first give review of few state of arts on optical antennas used for sorting of infrared. The basics of optical antenna and numerical study on optical patch antenna is discussed in this chapter.

In chapter 3, we will study the effect of fabrication error in spectral response of optical antennas discussed in chapter 2 and present experimental results.

In chapter 4, we will explore sorting concept for visible spectrum utilizing metallic and dielectric structures. We will also discuss the dielectric based multilayer antireflection coating and present the way to achieve optically efficient sorting structure for visible light which could be utilized for submicron pixels.

Chapter 2

Numerical study of optical patch antennas for infrared sorting

Optical antennas like its RF counterpart can be used both in transmitting and receiving mode. In receiving mode it concentrates the incoming radiation into small volume in their high field region [20]. Optical antennas are generally used in this mode as it can be applied in variety of applications including surface enhanced spectroscopy [21, 22]. Moreover, it can have larger effective collection area compared to its physical size [23, 24, 20]. This property could be used to spatially sort the photons with different energies with high efficiency. In this chapter, we will explore the antenna concept to achieve efficient sorting device. First we will review few state of art technologies which utilizes an optical antennas to sort infrared spectrum.

2.1 State of Art

Near perfect absorbing components using metallic metamaterial has attracted wide attentions due to its potential applications in various application in multi spectral imaging, photovoltaics and environment sensing [25, 2, 19, 26, 18, 27, 28]. Optical absorber utilizing continuous layer gap plasmon resonator (CL-GPR) has been

reported to have perfect absorption in infrared regime [29] in recent years. Using multiple metal strip supported by dielectric patchwork on continuous metal layer underlay is reported to efficiently route the incoming photons by their colors towards one of the two groups of antenna [2, 3].

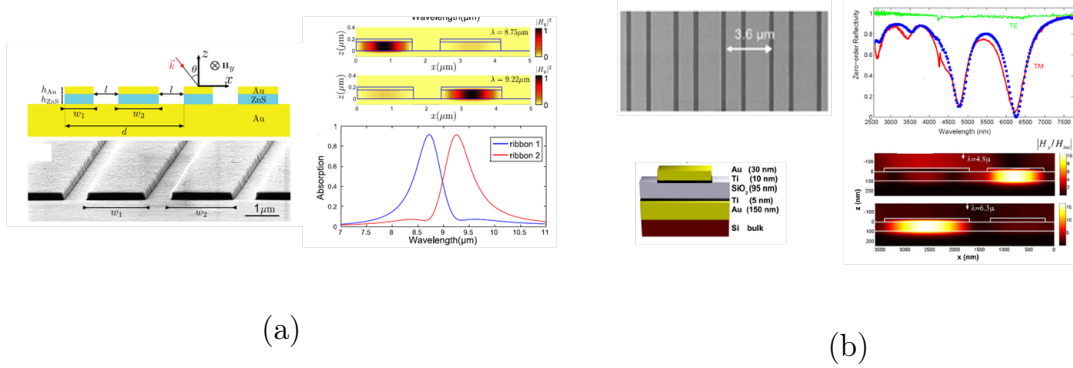


Figure 2.1: State of Art 1D MIM sorter (a)taken from [2] (b) taken from[3]

Figure 2.1 (a) shows the combination of two metal-insulator-metal (MIM) ribbons made with gold (Au) and ZnS. The metal strips of widths $w_1 : 1.67\mu\text{m}$ and $w_2 : 1.74\mu\text{m}$ are separated by distance $l : 0.82\mu\text{m}$ in [2] to route the infrared radiation with wavelengths $8.75\mu\text{m}$ and $9.22\mu\text{m}$ to their respective antennas. Similarly figure 2.1 (b) shows the two Metal (gold) strips of widths $w_1 : 1.15\mu\text{m}$ and $w_2 : 1.75\mu\text{m}$ supported by continuous dielectric layer on continuous metal underlay as studied in [3]. The structure is used to sort the mid infrared radiation $4.8\mu\text{m}$ and $6.2\mu\text{m}$ as can be seen in figure 2.1 (b). While the MIM sorting structures discussed in [2, 3] efficiently route the photons by their color toward their respective antenna, it is sensitive to polarization of incidence angle. Such MIM ribbon structure could only be used for TM polarization of incidence wave.

Recently study has been made to design wideband infrared absorber independent to polarization of incidence radiation utilizing the square MIM patch arrays [19]. The patch arrays studied in [19] are designed using Gold (Au) metallic layers. Such array has shown higher tolerance to incidence angle and polarization of incidence radiation. The spectral sorting using metallic structures has mostly been studied

using noble metals like gold, which are not compatible with CMOS technology. Although using such metals, the incidence radiation could be routed and absorbed with high efficiency, due to incompatibility to CMOS foundry, its use could be limited.

In this and next chapter, we numerically and experimentally study patch antenna structure using CMOS compatible material to sort different band of wavelengths in $8\mu\text{m}$ - $12\mu\text{m}$ infrared range so that these structures could be easily adapted and integrated to thermal imagers and other sensor applications.

2.2 Study of Optical patch antenna

The radiation property has been well studied for conventional RF resonant patch antenna. However, due to high metallic loss in optical domain, the model used for RF spectrum cannot be applied directly to evaluate the properties of optical patch antennas. More rigorous analysis is needed to study the behavior of such antenna. Recently, theoretical modeling of optical patch antenna and field enhancement in antenna cavity as a function of antenna geometrical parameters has been proposed [30]. In this section, we will discuss antenna modeling using transmission line theory and coupled mode theory in brief and derive important parameters necessary to design efficient patch antenna for spectral sorting.

2.2.1 Modeling of patch antenna

2.2.1.1 Resonance wavelength and field enhancement

Dielectric-Metal interface is known to excite propagative surface plasmon polaritons (P-SPP) when electromagnetic wave interact with metallic surface [31, 32] under phase matching condition. In presence of sub wavelength conductive scattering center, localized surface plasmon polaritons (L-SPP) could be excited, independent

of angle of incidence [32]. In optical patch antenna, which consists of ground metal plate, dielectric spacer and top metal patch, as shown in figure 2.2 (a) the surface plasmon polaritons (SPP) is excited in the metal-dielectric interface when incident electromagnetic wave interacts with antenna structure. The excited SPP in the interface couples to the insulator layer laterally. This induces oscillating fields inside the core creating Fabry-Perot like resonator. If the core thickness h is much smaller than incident wavelength, such structure can support confined TM_{100} mode with resonant wavelength λ_r determined by width W and insulator core index n_g of patch antenna [33, 34].

$$\lambda_r = 2Wn_g \quad (2.1)$$

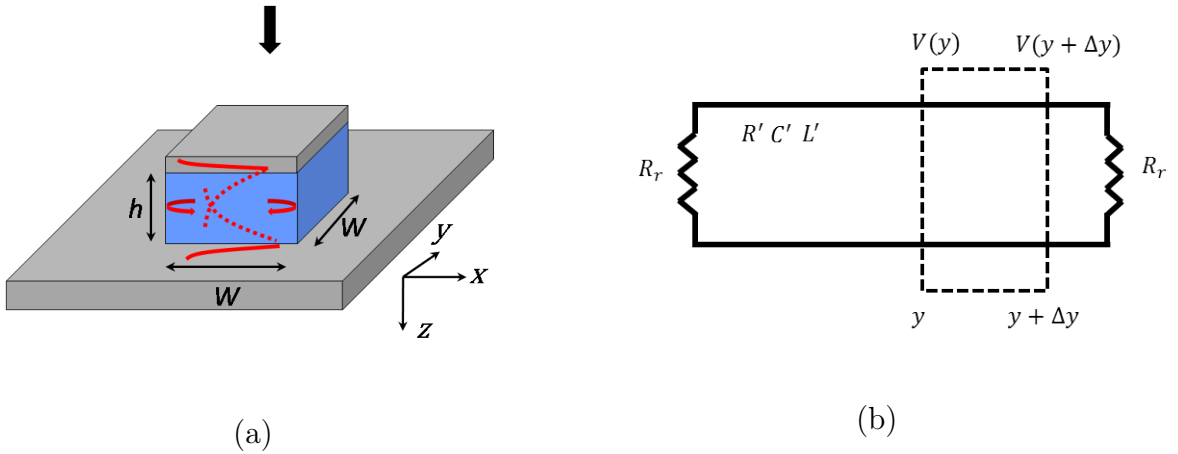


Figure 2.2: (a) Patch antenna with metal ground plate, with insulator width W , and height h . top metal thickness greater than skin depth is considered for the analysis (b) equivalent circuit model of patch antenna

At resonance, the field amplitude in the core of patch antenna can be much higher than the incidence field. The field enhancement factor (f), which is the ratio of core field amplitude to incidence field, has to be maximized for optimal performance of an antenna [35]. For an optical patch antenna, field enhancement factor can be evaluated using equivalent transmission line model as shown in figure 2.2(b). In the patch antenna, the ground plate produce an electromagnetic image of top metal

patch. The antenna therefore is similar to cut wire pair structure [36] in which the mode propagating within the plates are approximately TEM in nature [30]. This allows to formulate transmission line analysis of patch antenna as shown in figure 2.2 (b) where the quantities R' , C' , L' are the series resistance per unit length, capacitance per unit length and series inductance per unit length and depends on material and geometry of an antenna. The transmission line is terminated at either side of patch with an effective radiation resistance R_r of an antenna which could be calculated using induced voltage V and current I on the patch.

Assuming normal incidence of plane wave and polarized such that the magnetic field lies along x-axis, the peak voltage on patch antenna which occurs at the slot located at $y = \pm \frac{W}{2}$. With the knowledge of peak voltage, the field enhancement of the square patch antenna can be calculated as [30]:

$$f = \frac{2 \frac{k_0 R_r W}{g \eta_0 h} (1 + 2 \frac{\delta}{h})}{\frac{g}{k_0} \sin(\frac{gW}{2}) - i (\frac{W}{h}) \frac{R_r}{\eta_0} \cos(\frac{gW}{2})} \sin(\frac{gW}{2}) \quad (2.2)$$

Where, $k_0 = \frac{2\pi}{\lambda_0}$ is the free space wave vector, η_0 is the free space impedance, δ is the skin depth of metal and

$$g^2 = \beta^2 - ik_0 \frac{W}{h} \frac{R'}{\eta_0} \quad (2.3)$$

$$\beta = \frac{2\pi n_g}{\lambda_0} \quad (2.4)$$

The resistance per unit length R' depends on the geometric parameter and is given by:

$$R' = \eta_0 \frac{2hn_g}{W} \frac{\kappa \epsilon''}{(\tanh(\frac{k_x h}{2}) + \frac{k_x h}{2}) \frac{n_g \epsilon'^2}{\sqrt{n_g^2 - 1}} - \frac{n_g \epsilon'^2}{\sqrt{n_g^2 - \epsilon'}}} \quad (2.5)$$

Where $k_x = k_0\sqrt{(n_g^2 - 1)}$, $\kappa = k_0\sqrt{(n_g^2 - \epsilon')}$, ϵ' , ϵ'' are real and imaginary part of metal dielectric function and n_g is the effective index of waveguide mode. The radiation resistance R_r of an antenna can be calculated as:

$$R_r = \frac{\pi^2 \eta_0}{2I_1} \quad (2.6)$$

$$I_1 = \int_0^\pi \int_0^\pi \cos^2 \left(\frac{k_0 W}{2} \sin\theta \sin\varphi \right) \sin^3\theta \frac{\sin^2 \left(\frac{k_0 W}{2} \cos\theta \right)}{\cos^2\theta} d\theta d\varphi \quad (2.7)$$

Here, θ is taken from positive y-axis while φ is in xz- plane and taken from z-axis.

It can be seen from equation 2.2, that by appropriately choosing the material and dimensions of an antenna, the field in insulator core could be maximize, thus enabling the funneling of incidence light into sub wavelength region. For further information on transmission line model of patch antenna and calculation of field enhancement, readers are suggested to go through reference [30].

2.2.1.2 Antenna effective cross section area

In the previous section, we discuss that the SPP induced in metal-dielectric interface of patch antenna couples to core laterally creating a Fabry-Perot type resonator. We also discussed the resonance condition and field enhancement factor to design an optical patch antenna. We find that by controlling antenna dimension, the field in insulator core could be maximized for optimal working of an antenna. However, patch antenna can also be optimized considering its scattering and absorbing behavior. Patch antenna acts as a scattering center for incident radiation. A portion of incident power is scattered and absorbed by an antenna. In this section we derive two fundamental parameters, mainly scattering cross section area σ_{scat} and absorption cross section area σ_{abs} that could be optimized to increase interaction of incident wave with an antenna using couple mode theory [37]. The scattering cross section

area and absorption cross section area quantify the quality of interaction of antenna with incoming radiation.

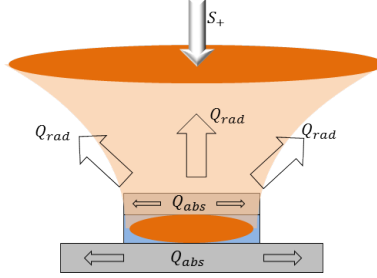


Figure 2.3: Schematic for modeling antenna with coupled mode theory

Figure 2.3 shows the schematic for modeling optical resonator with coupled mode theory, in which mode amplitude equation of a resonator excited by incidence wave with amplitude s_+ is given by [37]:

$$\frac{da}{dt} = i\omega_0 a - \left(\frac{1}{\tau_{abs}} + \frac{1}{\tau_{rad}} \right) a + \kappa s_+ \quad (2.8)$$

Where, a and κ are the mode amplitude in cavity and coupling coefficient of incidence wave s_+ to antenna respectively, ω_0 is the resonance frequency, $\frac{1}{\tau_{abs}}$ and $\frac{1}{\tau_{rad}}$ are the decay rate due to absorption and radiation respectively. Considering A_e and A_{inc} as effective aperture of an antenna and spot size of incidence wave, coupling coefficient κ can be expressed as:

$$\kappa = \sqrt{\frac{2A_e/A_{inc}}{\tau_{rad}}} \quad (2.9)$$

Using expression 2.9 in equation 2.8, the mode amplitude equation can therefore be written as:

$$\frac{da}{dt} = i\omega_0 a - \left(\frac{1}{\tau_{abs}} + \frac{1}{\tau_{rad}} \right) a + \sqrt{\frac{2A_e/A_{inc}}{\tau_{rad}}} s_+ \quad (2.10)$$

The wave amplitude s_+ is normalized such that $|s_+|^2$ represents the power carried by incidence wave where as $|a|^2$ represents the energy stored in resonator cavity. For the incidence wave with frequency ω , the response can be find from 2.10 as:

$$a = \frac{\sqrt{\frac{2A_e/A_{inc}}{\tau_{rad}}} s_+}{i(\omega - \omega_0) + \left(\frac{1}{\tau_{abs}} + \frac{1}{\tau_{rad}}\right)} \quad (2.11)$$

And energy stored in cavity can be calculated as:

$$|a|^2 = \frac{\frac{2A_e/A_{inc}}{\tau_{rad}}}{(\omega - \omega_0)^2 + \left(\frac{1}{\tau_{abs}} + \frac{1}{\tau_{rad}}\right)^2} |s_+|^2 \quad (2.12)$$

Using expression 2.12 for stored energy in cavity, power dissipation due to scattering and absorption can then be calculated as:

$$P_{scat} = \frac{2|a|^2}{\tau_{rad}} = \frac{4\frac{A_e/A_{inc}}{\tau_{rad}^2}}{(\omega - \omega_0)^2 + \left(\frac{1}{\tau_{abs}} + \frac{1}{\tau_{rad}}\right)^2} |s_+|^2 \quad (2.13)$$

$$P_{abs} = \frac{2|a|^2}{\tau_{abs}} = \frac{4\frac{A_e/A_{inc}}{\tau_{rad}\tau_{abs}}}{(\omega - \omega_0)^2 + \left(\frac{1}{\tau_{abs}} + \frac{1}{\tau_{rad}}\right)^2} |s_+|^2 \quad (2.14)$$

Using the power dissipation due to scattering and absorption, the effective cross section area, $\sigma = P/I_0$ can be calculated using relations $I_0 = \frac{|s_+|^2}{A_{inc}}$ as:

$$\sigma_{scat} = \frac{P_{scat}}{I_0} = \frac{4\frac{A_e}{\tau_{rad}^2}}{(\omega - \omega_0)^2 + \left(\frac{1}{\tau_{abs}} + \frac{1}{\tau_{rad}}\right)^2} \quad (2.15)$$

$$\sigma_{abs} = \frac{P_{abs}}{I_0} = \frac{4\frac{A_e}{\tau_{rad}\tau_{abs}}}{(\omega - \omega_0)^2 + \left(\frac{1}{\tau_{abs}} + \frac{1}{\tau_{rad}}\right)^2} \quad (2.16)$$

Now, using the definition of quality factor $Q = \frac{\omega_0\tau}{2}$, the effective cross section area at resonance $\omega = \omega_0$ can be written as:

$$\sigma_{scat} = \frac{P_{scat}}{I_0} = 4A_e \frac{Q^2}{Q_{rad}^2} \quad (2.17)$$

$$\sigma_{abs} = \frac{P_{abs}}{I_0} = 4A_e \frac{Q^2}{Q_{rad}Q_{abs}} \quad (2.18)$$

The sum $\sigma_{ext} = \sigma_{scat} + \sigma_{abs}$ gives the extinction coefficient of an antenna. Here we used the relation for total quality factor of resonator Q :

$$\frac{1}{Q} = \frac{1}{Q_{abs}} + \frac{1}{Q_{rad}} \quad (2.19)$$

Where, Q_{rad} and Q_{abs} are quality factors corresponding to scattering and absorption respectively. The cross section areas derived in 2.15 - 2.18 can be normalized to an antenna physical area (A_p) as:

$$\sigma'_{scat} = \frac{\sigma_{scat}}{A_p} \quad (2.20)$$

$$\sigma'_{abs} = \frac{\sigma_{abs}}{A_p} \quad (2.21)$$

Using these normalized cross section area; we can have an overview of an extent of spatial area in which antenna interacts with incidence wave. Figure 2.4 shows the normalized absorption and scattering cross section area of an optical patch antenna with width W : $1.2\mu\text{m}$ and core thickness of h_{ins} : 350nm resonating at $8.6\mu\text{m}$. Constant refractive index of 3.6 is considered for insulator core for the calculation.

It can be seen from figure 2.4 that the interaction area of the resonant antenna is much larger than its physical area. However, it can also be seen that the normalized cross section areas does not acquire same values with core thickness of h_{ins} : 350nm for investigated antenna. In previous section we discuss that the SPP excited in

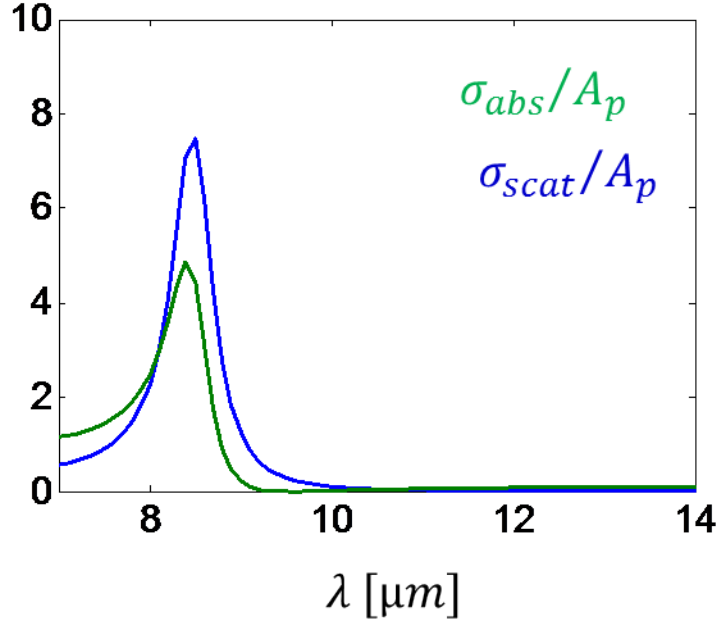


Figure 2.4: Normalized cross section area of patch antenna resonating at 8.2 μm insulator-metal interface couples to core of an antenna. Since there are two metallic interface with core in patch antenna, the SPP from these interface could overlap. However, at certain core thickness the overlapping of SPP could be minimized creating an optimal condition for an antenna to acquire same value of scattering cross section and absorption cross section area. When these two cross section areas σ_{abs} and σ_{scat} acquires same values, there will be no reflection (scattering) of incidence wavelength from an antenna, all of the incident power is transfer to resonating mode [20]. The condition when σ_{abs} and σ_{scat} acquires same values is known as critical coupling.

2.2.1.3 Antenna absorption at resonance

In previous two sections, we studied different methods to model an optical patch antenna. The antenna could be optimized using different concepts, maximizing field enhancement or optimizing antenna dimensions to achieve critical coupling. At resonance, we find that the incident power is absorbed by an antenna. The

absorption $(1 - R)$ at resonance can be related to field enhancement factor f and extinction cross section area $\sigma_{ext} = \sigma_{scat} + \sigma_{abs}$ of an antenna using coupled mode theory, [20, 38] as:

$$A = 1 - R = \frac{2\pi V_{eff}}{A_{inc}\lambda_r Q_{abs}} f = \frac{\sigma_{ext}}{A_{inc}} \frac{Q}{Q_{abs}} \quad (2.22)$$

Where V_{eff} is the effective mode volume of the antenna, which quantify the electric field strength per unit photon[39] . From equation 2.22, we can see that the absorption is proportional to field enhancement. In other form it is proportional to extinction coefficient and antenna absorption efficiency $(\frac{Q}{Q_{abs}})$. All of these antenna properties are dependent on the geometrical parameters of the antenna. Therefore to achieve maximum absorption we can follow these simple steps:

1. Determine antenna width to make it resonate at wavelength λ_r using equation 2.1.
2. With resonant wavelength (or width of patch antenna) fixed, optimize other antenna parameter like top metal thickness, insulator thickness, ground metal plate thickness and material associated with different layers in antenna, to achieve maximum field enhancement f or critical coupling condition $\sigma_{abs} = \sigma_{scat}$ or $Q_{rad} = Q_{abs}$ at which antenna absorption efficiency $(\frac{Q}{Q_{abs}})$ is maximum.

The antenna could be optimized by following either of one modeling methods discussed in previous sections, however in this thesis we follow cross section model to study the antenna and spectral sorting. The scattering cross section area and absorption cross section area gives more insight into the interaction area of antenna which leads to easy interpretation of spectral sorting.

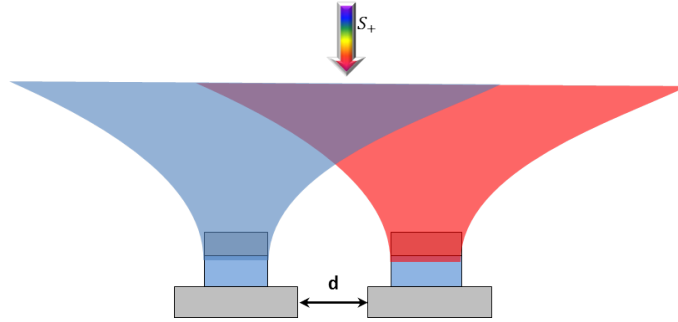


Figure 2.5: Two antennas with overlapped cross sections

For spectral sorter based on optical antennas, we can design and optimize antenna resonating at different wavelengths. These antennas can then be placed or fabricated near to each other separated by distance d such that the effective cross section area of these antennas overlaps as shown in figure 2.5. Due to the larger interaction area, the incident radiation can be sorted according to its color in respective antennas even at sub wavelength regime achieving near perfect absorption of resonant wavelength. The extend of cross section overlap could further be increased by reducing the separation distance d . Using such approach, optical efficiency (NOE) of detectors could be maximized even for small pixel dimension.

2.2.2 Numerical study of Single patch antenna

In this section, we first study the behavior of isolated patch antenna using finite difference time domain (FDTD) based software Lumerical FDTD. Perfectly matched layer (PML) boundary condition is used for study of an isolated patch antennas with different widths. Later we will discuss the periodic antenna array and its absorption properties. From the study of isolated patch antenna we can have an idea of the scattering and absorption cross section area and its effect on absorption characteristic of the antenna. The information could later be used to design spectral sorter. The readers are suggested to go thorough reference [40] for theory of FDTD method for electromagnetic simulations.

We use CMOS compatible tungsten patch antenna with amorphous silicon (a-Si) spacer coated on tungsten ground plate. Figure 2.6 (a-b) shows the simulation domain, in which we vary the width (W) of square patch antenna. The spacer thickness (h_{ins}) of $350nm$, top metal patch thickness (h_{umet}) of $50nm$ and ground plate thickness (h_{gp}) of $200nm$ were considered for study. The refractive index of tungsten is adopted from Palik handbook of optical constants [41], whereas the refractive index of 3.6 is used for a-Si. The antenna is illuminated with TM-polarized Total field scattered field (TFSF) source with illumination spot size of $4\mu m \times 4\mu m$. The fields scattered and absorbed by the antenna were recorded using scattered field monitor and absorption field monitor respectively. The absorption normalized to source power, wavelength of antenna resonance, scattering and absorption cross section area normalized to patch area are then calculated for different antenna width and is shown in figure 2.6 (c-d). As can be seen in figure 2.6(c), that the resonance wavelength varies linearly with patch width as given by relation 2.1. Also the increase in absorption is observed as the patch width is increased. Figure 2.6 (d) shows the absorption cross section area and scattering cross section area of the antenna as a function of patch width. It can be seen that the scattering cross section area decreases rapidly compared to absorption cross section area for given $350nm$ a-Si spacer when patch width is increased.

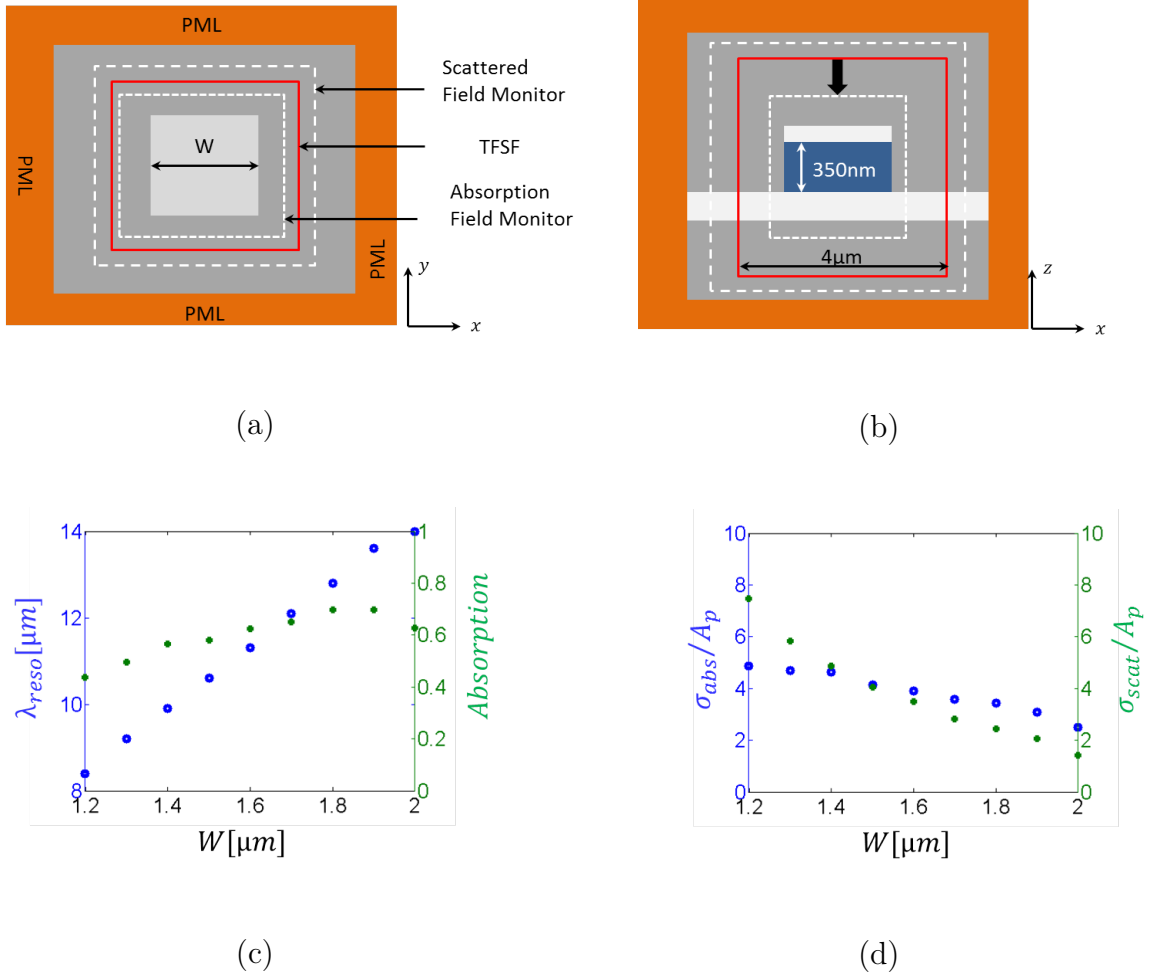
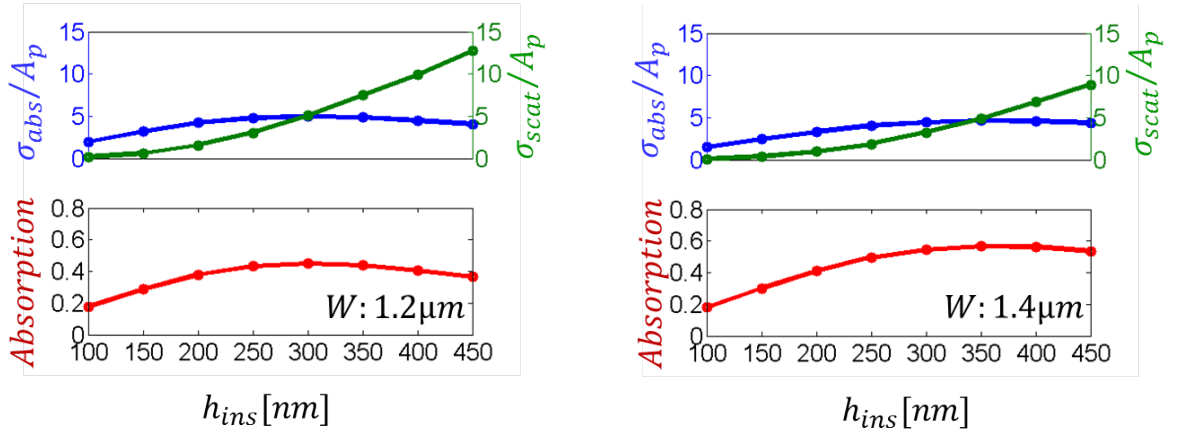


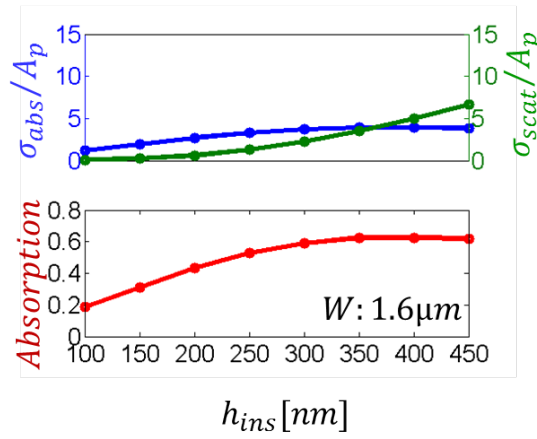
Figure 2.6: (a) top view of simulation region (b) side view of simulation region (c) resonance wavelength and normalized absorption as a function of patch width (d) scattering cross section area and absorption cross section area normalized to patch area

The decrease in antenna absorption can be attributed to decrease in absorption cross section area of an antenna when its width is increased. In addition it can also be attributed to mismatch between absorption quality factor and scattering quality factor ($Q_{\text{rad}} \neq Q_{\text{abs}}$) which is responsible for difference in scattering and absorption cross section area as seen in figure 2.6 (d). In critical coupling ($Q_{\text{rad}} = Q_{\text{abs}}$) the scattering and absorption cross section area of the antenna overlaps and have same values. This condition can be achieved by optimizing the spacer thickness of an isolated antenna.



(a)

(b)



(c)

Figure 2.7: Normalized cross section area and absorption as a function of spacer height of an isolated antenna with patch width (a) $1.2\mu m$ (b) $1.4\mu m$ and (c) $1.6\mu m$

Figure 2.7 shows the absorption and scattering cross section area normalized to antenna physical area along with normalized absorption of the antenna when spacer thickness is varied. Antenna resonating at $8.4\mu m$, $9.9\mu m$ and $11.3\mu m$ with respective patch size of $1.2\mu m$, $1.4\mu m$ and $1.6\mu m$ is considered for the study. As can be seen, the absorption increases with increase in spacer thickness. The absorption cross section area acquires same value as scattering cross section at spacer thickness of

300nm, 350nm and 365nm for the antennas with patch width 1.2 μ m, 1.4 μ m and 1.6 μ m respectively. For this thickness the absorption maximum is also observed indicating critical coupling. The absorption spectra of these antennas using optimal spacer thickness is shown in figure 2.8. It can be seen from figure 2.7, that the thicker spacer is required for critical coupling of the incident wave to the antenna for an antenna resonating in longer wavelengths.

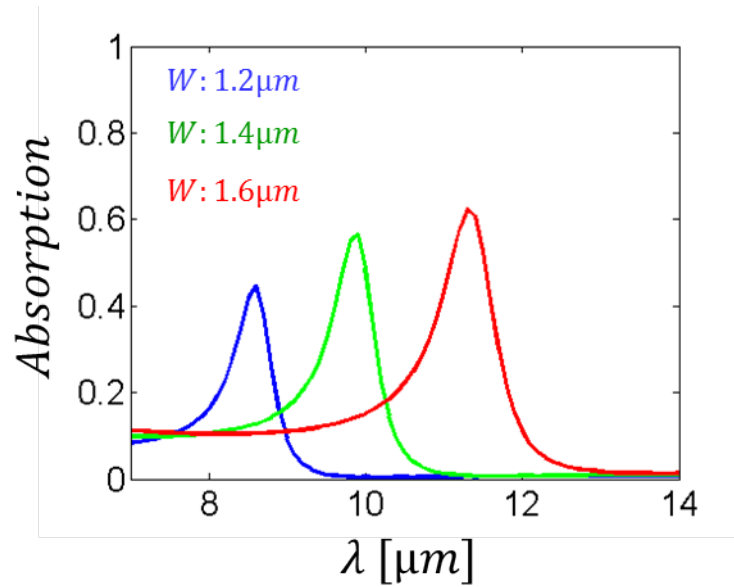


Figure 2.8: Absorption spectra of an antenna using optimal spacer thickness for given patch width (shown in inset). $4\mu\text{m} \times 4\mu\text{m}$ illumination spot size is used for calculation.

2.2.3 Antenna mutual coupling and its effect on absorption property

Two antennas or resonators positioned at different location can couple to each other [37]. This spatial coupling of an antenna modify the absorption characteristics of an antenna depending on spatial separation and arrangement of the antennas. In this section, we study the effect of spatial separation and orientation of antenna arrangement on absorption property of an antenna.

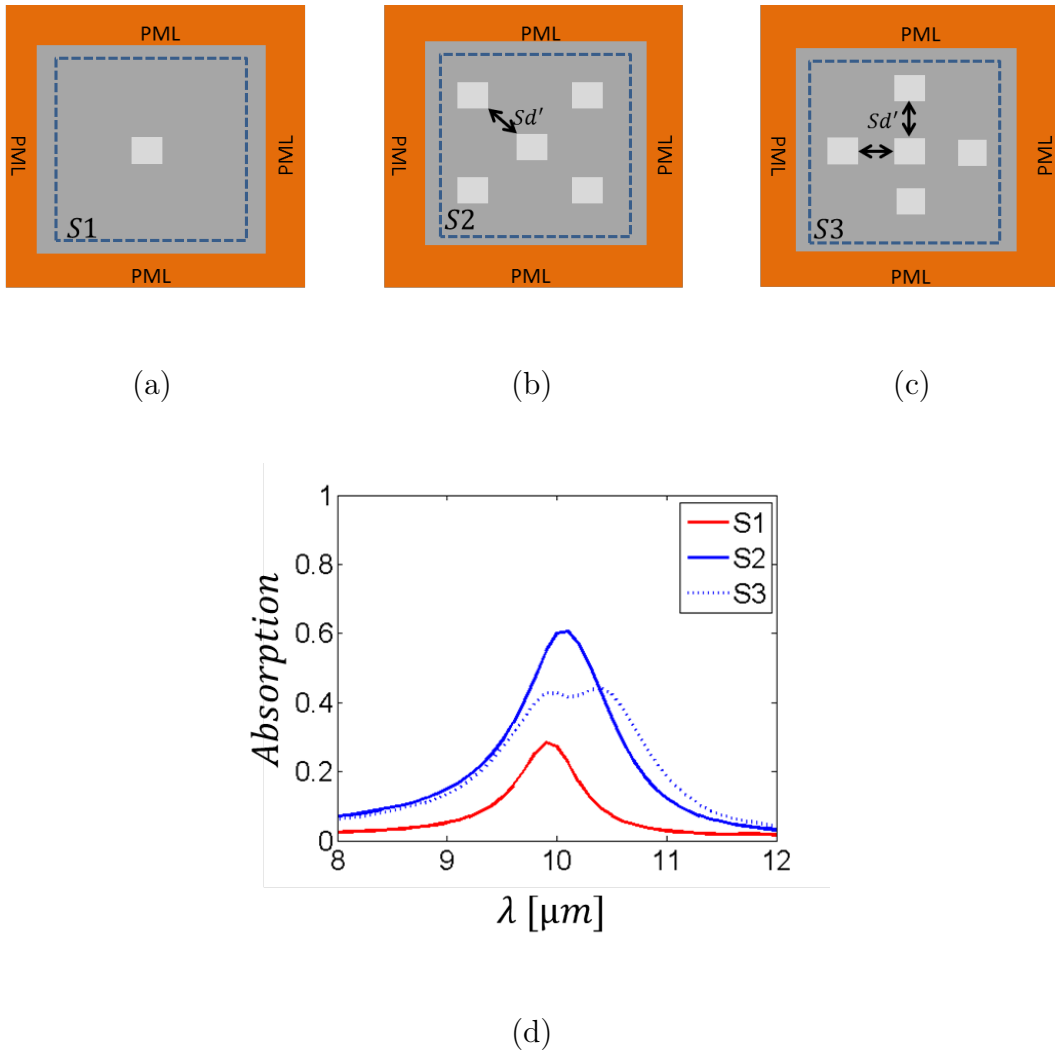


Figure 2.9: Patch antenna with patch width $1400nm$ arranged in different arrangement (a) single patch antenna at center ($S1$), (b) cross arrangement ($S2$), (c) plus arrangement ($S3$) with antenna-antenna separation distance Sd' (d) absorption spectra of arrangement $S1$, $S2$ and $S3$

Figure 2.9 (a-c) shows the different antenna arrangements considered for study. The antenna width (W) of $1400nm$ and illumination spot size of $10\mu m \times 10\mu m$ is considered. The thickness of top metal patch and spacer is fixed to $50nm$ and $350nm$ respectively while thickness of metal ground plate is fixed to $200nm$. Figure 2.9 (a) shows the single patch antenna while figure 2.9 (b-c) shows the cross arrangement and plus arrangement respectively with antenna-antenna separation distance Sd' . For simplicity the arrangements are called $S1$, $S2$ and $S3$ respectively as shown in inset in figure 2.9 (a-c). Figure 2.9 (d) shows the absorption spectra of the antenna

arrangements $S1$, $S2$ and $S3$. The antenna-antenna separation distance Sd' of $500nm$ is considered for antenna arrangement $S2$ and $S3$. The absorption spectrum of $S1$ is used as a reference to compare later two structures. The absorption peak at $10\mu m$ is observed for both $S1$ and $S2$. While the splitting of absorption spectrum with two absorption peaks at $9.9\mu m$ and $10.4\mu m$ is observed for $S3$, indicating the lateral coupling of excited SPP between two antennas. Such coupling is minimized in case of $S2$. This suggests that the effect of spatial coupling is more prominent in $S3$ than in $S2$. It is however interesting to understand for which value of Sd' the spatial coupling will start to have minimal effect in absorption spectra.

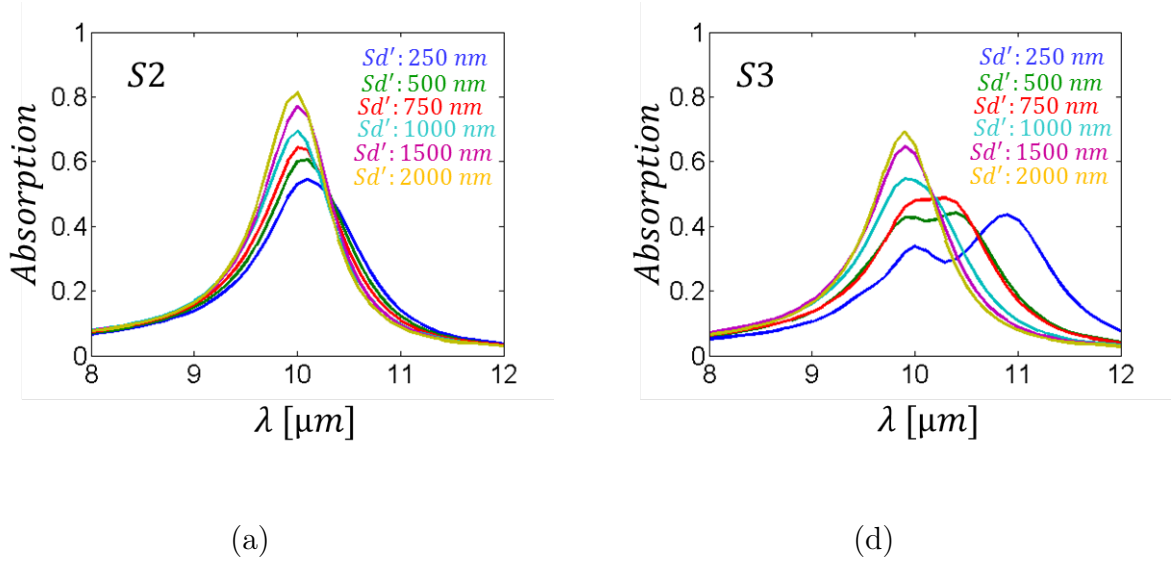


Figure 2.10: Absorption spectrum for different Sd' (a) antenna arrangement $S2$ (b) antenna arrangement $S3$

Figure 2.10 (a) and (b) shows the absorption spectra of antenna arrangement $S2$ and $S3$ respectively when antenna-antenna separation distance Sd' is varied from $250nm - 2000nm$ in $250nm$ step. For $S2$, the splitting in absorption spectrum is not observed for all the values of Sd' considered. While for $S3$, the splitting starts to cease for Sd' greater than $1000nm$. These result provides an important understanding on effect of antenna arrangement and separation distance which can later be used for designing the spectral sorting device.

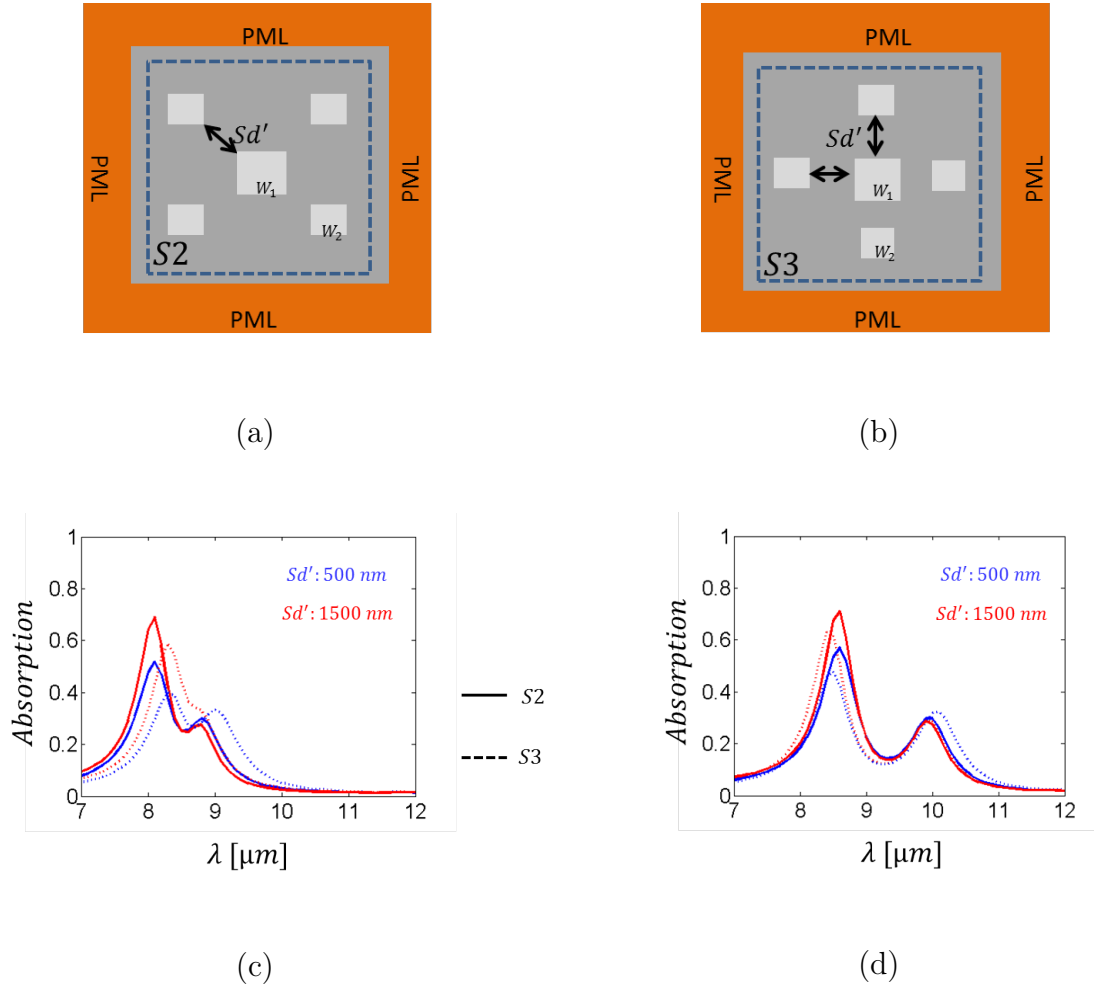


Figure 2.11: Antenna with width W_1 surrounded by another antenna with width W_2 (a) Cross arrangement (b) Plus arrangement, Absorption spectra with (c) $W_1 : 1240nm$ $W_2 : 1150nm$ (d) $W_1 : 1400nm$ $W_2 : 1200nm$

We further study the effect of antenna arrangement on absorption characteristics using two different antenna patch widths. Figure 2.11 (a) and (b) respectively shows the arrangement S_2 and S_3 , with central patch width W_1 and surrounding patch width W_2 . We first use $W_1 : 1240nm$ and $W_2 : 1150nm$ ($\Delta W : 90nm$) to calculate the absorption spectra as shown in figure 2.11 (c). Later, we use $W_1 : 1400nm$ and $W_2 : 1200nm$ ($\Delta W : 200nm$) and calculate the absorption spectra for S_2 and S_3 as shown in figure 2.11 (d). The solid line depicts the absorption spectra for S_2 , while dotted line shows the absorption for S_3 .

It can be seen that for small difference in patch width ΔW , the absorption spectra is not affected by separation distance Sd' for arrangement $S2$. While that for $S3$, spectral shift in absorption is observed when Sd' is increased. Also broadening in spectral width is observed for shorter wavelength. For $Sd' : 1500nm$ the absorption shoulder at $8.8\mu m$ is still visible however it is not as distinct as for arrangement $S2$. For higher ΔW the spectra is not sensitive to the antenna arrangement as can be seen in figure 2.11 (d). It can be seen that it is advantageous to place the antennas with comparable dimensions diagonally rather than laterally since it minimize the coupling between the antennas even for smaller separation distance.

2.3 Spectral sorting and broadband absorption using patch antenna

In previous section, we study the individual patch antenna and its absorption properties. We found that for optimal spacer thickness the effective cross section area is much larger than its physical area. We also study the mutual coupling between the antennas. We found that it is advantageous to arrange the antennas with comparable dimensions diagonally to minimize the coupling and thus maximize the absorption of resonance wavelength. In this section we study the spectral sorting using the antennas with different patch width. We first study the absorption properties of limited number of antennas arranged to achieve spectral sorting at different spatial location. Later we study the absorption properties of periodic antenna array designed for multi spectral broadband absorption of incident wave.

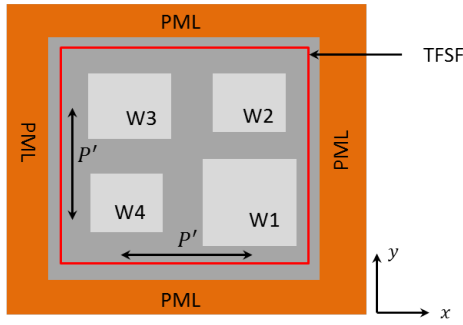
2.3.1 Spectral Sorting using patch antenna array

We can take advantage of increased collection area of antenna and arrange them such that the collection area of individual antenna overlaps as described in section

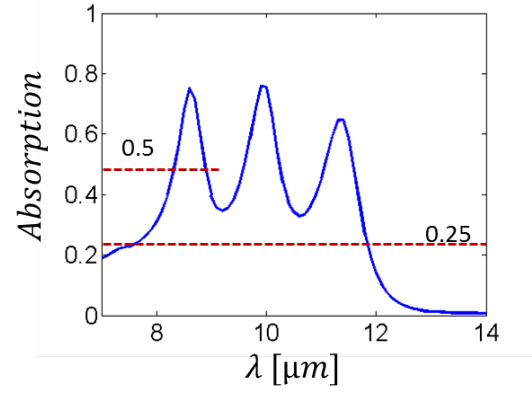
2.2.1. One such arrangement is shown in figure 2.12 (a) where different antennas are arranged in square lattice with center to center distance denoted by P' and individual patch width denoted by $W1, W2, W3, W4$ respectively.

Figure 2.12 (b) shows the total absorption spectra for the antenna arrangement shown in figure 2.12 (a) with antenna width fixed to $W1 : 1600nm, W2 = W4 : 1220nm, W3 : 1400nm$ and $P' : 2000nm$. We study the antenna array using Lumerical Solution. Total field scattered field (TFSF) source with illumination spot size of $5\mu m \times 5\mu m$ and TM-polarization was used for study. The a-Si spacer thickness of $350nm$ was considered for the study. The metal thickness of $50nm$ and $200nm$ were used for top tungsten patch and ground tungsten plate respectively. The absorption peaks at $8.5\mu m, 9.8\mu m$ and $11.5\mu m$ is observed, which are the resonant wavelengths of the antenna with patch width of $1220nm(W2, W4), 1400nm(W3)$ and $1600nm(W1)$ respectively. The red line in figure 2.12 (b) shows the maximum absorption that can be achieved as predicted by equation 1.5 for each resonant wavelength if we use the filter arrays.

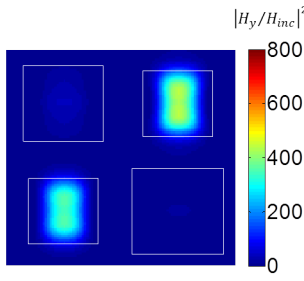
Since we use two patches of same width $W2$ and $W4$ the theoretical maximum is 0.5 for total absorption at resonance for these antennas. We see that the peak absorptions are much higher than that predicted by equation 1.5 at individual resonant wavelength of an antenna. This signifies the phenomenon of spectral sorting. To further confirm the sorting effect, the magnetic field maps were calculated at each resonant wavelength. As can be seen in figure 2.12 (c –e) the field is localized to the corresponding antenna when illuminated by its corresponding resonant wavelength.



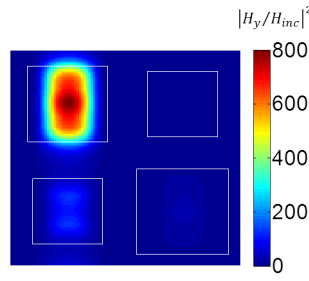
(a)



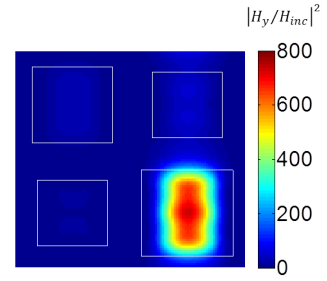
(b)



(c)



(d)



(e)

Figure 2.12: (a) patch antennas with different width arranged in square lattice with center to center distance P' (b) absorption spectra of antenna array shown in (a) with $W1 : 1600nm$ $W2 = W4 : 1220nm$ $W3 : 1400nm$ and $P' : 2000nm$, magnetic field map corresponding to resonance wavelength of (c) $W2$ and $W4$ ($\lambda = 8.5\mu m$), (d) $W3$ ($\lambda = 9.8\mu m$) and (e) $W1$ ($\lambda = 11.5\mu m$)

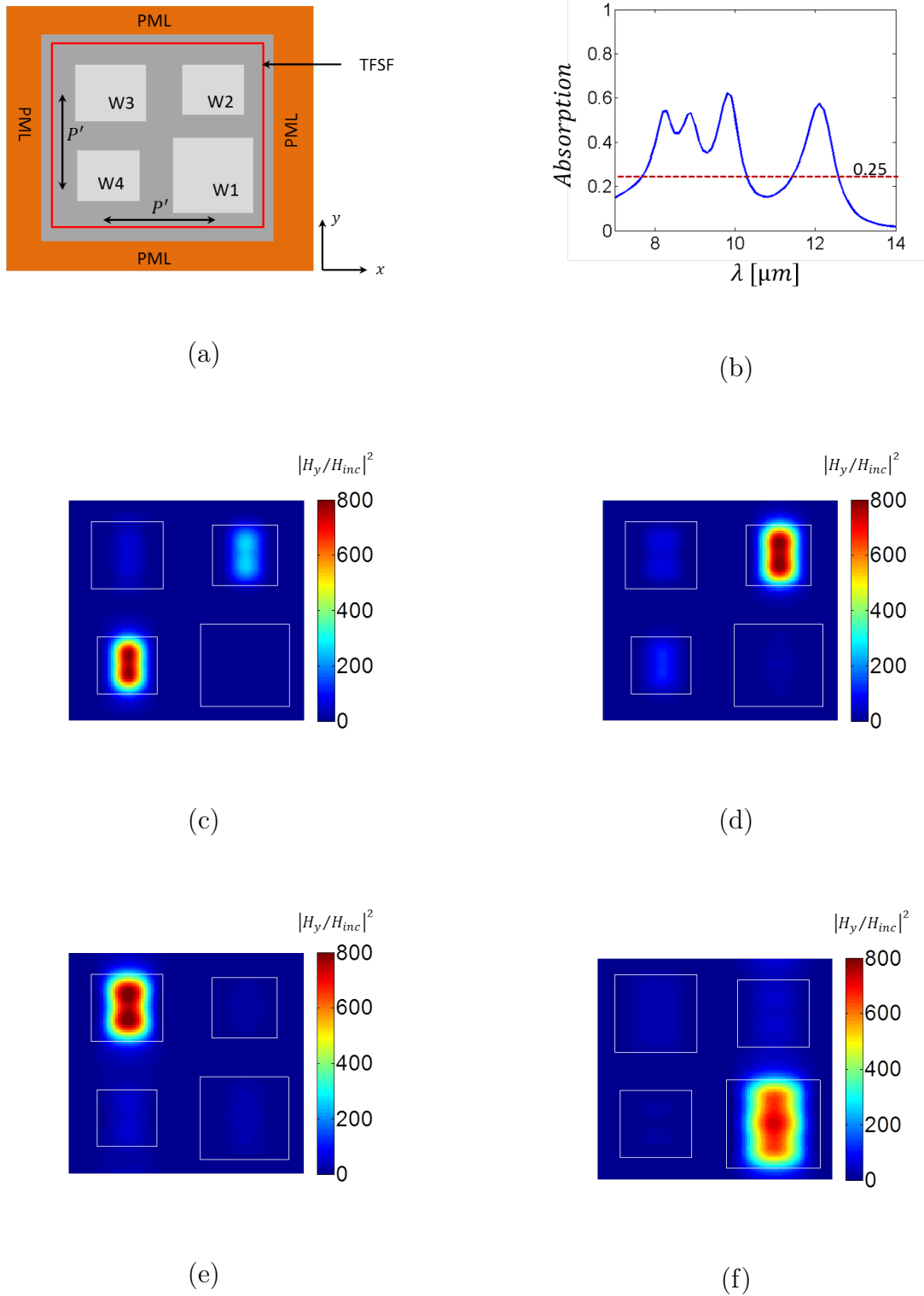


Figure 2.13: (a) patch antennas with different width arranged in square lattice with center to center distance P' (b) absorption spectra of antenna array shown in (a) with $W1 : 1685\text{nm}$ $W2 : 1240\text{nm}$, $W3 : 1370\text{nm}$, $W4 : 1150\text{nm}$ and $P' : 2250\text{nm}$, magnetic field map corresponding to resonance wavelength of (c) $W4(\lambda = 8.2\mu\text{m})$, (d) $W2(\lambda = 8.9\mu\text{m})$, (e) $W3(\lambda = 9.8\mu\text{m})$ and (f) $W1(\lambda = 12.0\mu\text{m})$

The antenna array can also be designed to achieve broadband absorption exploiting the sorting effect. We use four different patch sizes of $W1 : 1685nm$, $W2 : 1240nm$, $W3 : 1370nm$ and $W4 : 1150nm$ in the array to achieve four color sorting as shown in figure 2.13 (a). The center to center distance (P') of $2250nm$ was considered for study. The a-Si spacer thickness, top tungsten patch and ground tungsten plate thickness were kept constant to $350nm$, $50nm$ and $200nm$ respectively. Figure 2.13 (b) shows the corresponding absorption spectra, where we can see the absorption at resonance are more than 0.25, indicating sorting effect. Figure 2.13 (c-f) shows the magnetic field maps at wavelengths corresponding to absorption peak seen in figure 2.13 (b). We see that the absorption spectra has a broadband characteristics in $7 - 10\mu m$ with another absorption peak at $12\mu m$.

Using differently sized metal patch antenna we can therefore tailor multi spectral absorption with high efficiency. Moreover broadband absorption can be achieved using such antenna arrangement. For the practical applications we can use the periodic array of such antenna arrangement. In next section we will discuss the absorption properties of periodic array of antenna arrangement discussed in this section. We will also discuss the influence of various geometrical parameters in absorption properties.

2.3.2 Multi Spectral Absorption using periodic patch antenna array

In previous section, we studied the isolated antenna array to achieve spectral sorting. Such array needs illumination spot size in micro meter range. However, for most of the practical applications the illumination spot size is much larger and could be approximated as plane wave excitation. Using periodic arrangement of antenna array described in previous section, the radiation pattern can be optimized to match plane wave excitation [20]. Figure 2.14 (a) and (b) shows the top view of unit cell of

periodic antenna array considered for selective absorption of three and four spectra in $7 - 14\mu m$ infrared range respectively.

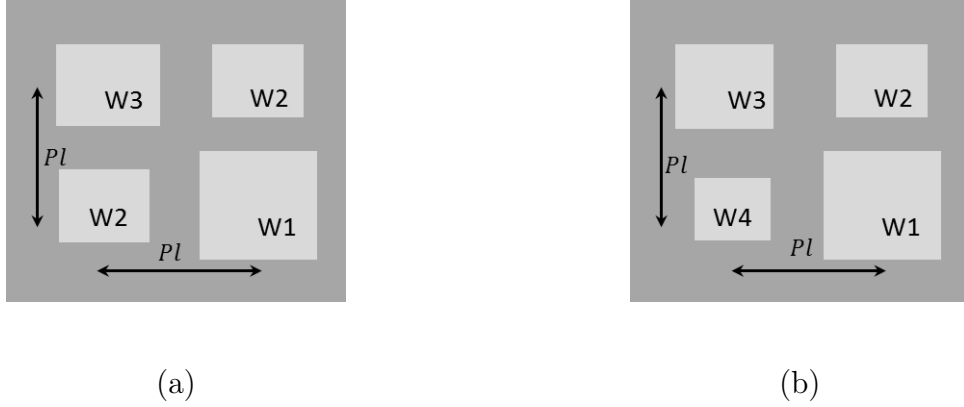


Figure 2.14: Unit cell of periodic antenna array considered for multi spectral absorption in $7 - 14\mu m$ infrared range (a) three spectra, (b) four spectra

We consider the antennas array with patch widths $W1 : 1600nm$, $W2 : 1220nm$ $W3 : 1400nm$ to selectively absorb three wavelengths and $W1 : 1685nm$, $W2 : 1240nm$, $W3 : 1370nm$ and $W4 : 1150nm$ to selectively absorb four wavelengths in infrared regime. For simplicity, we name these antenna array $3CS$ and $4CS$ respectively. The patchworks are arranged in square lattice with local period (distance between center of one patch to another) Pl . The absorption as a function of local period (Pl) and a-Si spacer thickness(h_{ins}) were calculated using Rigorous coupled wave analysis (RCWA) to study the influence of array geometrical parameters in antenna absorption. Figure 2.15 (a) and (b) shows the absorption as a function of local period Pl for $3CS$ and $4CS$ respectively. For this calculation the a-Si spacer thickness (h_{ins}) of $350nm$, top metal patch thickness (h_{umet}) of $50nm$ and ground plate thickness (h_{gp}) of $200nm$ were considered. We consider normal incidence of wave which is TM polarized, for the study.

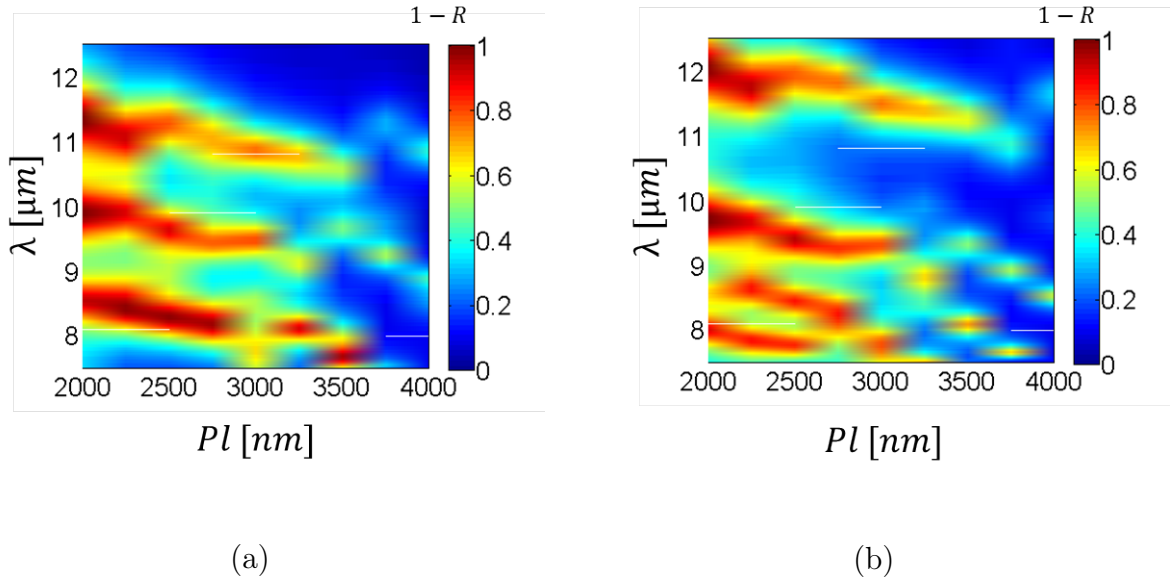


Figure 2.15: Absorption as a function of local period Pl (a) three spectra (b) four spectra.

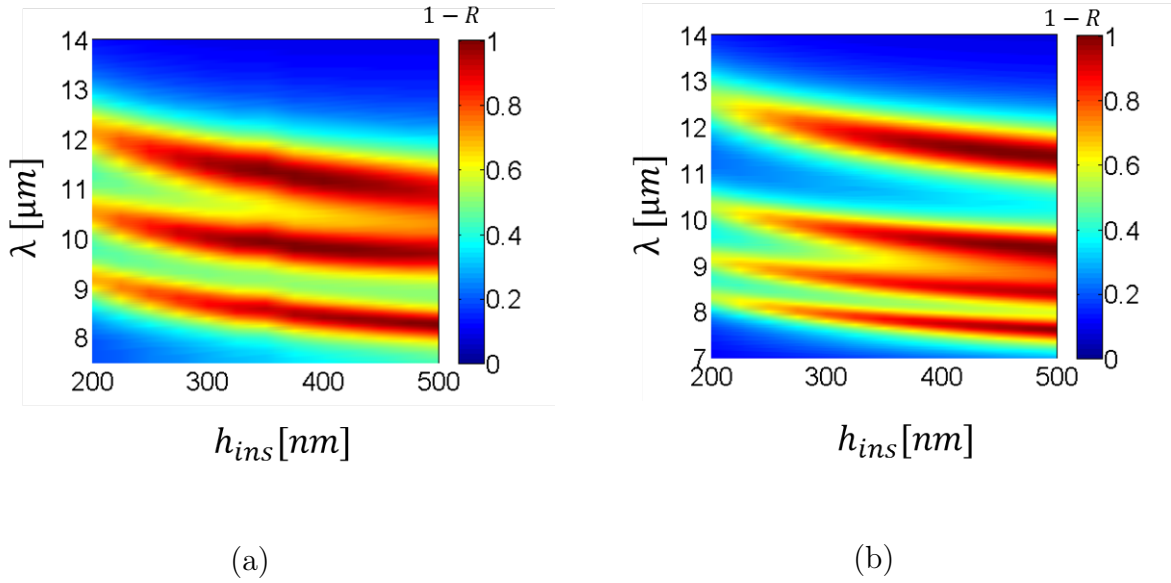


Figure 2.16: Absorption as a function of a-Si spacer thickness (a) three spectra (b) four spectra

It can be seen from the figure 2.15 that near perfect absorption could be achieved in multiple spectra for specific values of Pl . However, with increase in Pl the blue shift in absorption wavelength is observed for both antenna arrangements. The absorption tends to decrease when Pl is higher than $3000nm$. Moreover, for higher

value of Pl , the antenna array cease to work as multi spectral absorber. It is therefore, very important to choose the value of Pl so that the antenna array still works as multi spectral absorber and has higher absorption efficiency. For $3CS$ the optimal value of Pl is found to be $2000nm$, while that for $4CS$, $2250nm$ is calculated to be optimal value. As discussed in section 2.2.1, the spacer thickness determines the critical coupling of incidence wave to antenna and depends on the resonant wavelength of individual antennas in the array. However, from technological point of view, it is easier to fabricate the antennas with common spacer thickness. It is therefore necessary to find the optimal common thickness of spacer for all the antennas in the array. Using optimal values for local period, we now study the effect of a-Si thickness (h_{ins}) in antenna absorption. The other parameters h_{umet} , and h_{gp} were unchanged for the study. Figure 2.16 (a) and (b) respectively shows the absorption as a function of spacer thickness for $3CS$ and $4CS$. It can be seen that the absorption increases with spacer thickness. At the same time, blue shift in absorption wavelength is observed with increase in spacer thickness. It can be seen in figure 2.16 (a-b) that for spacer thickness larger than $400nm$, the spectral width broadens for longer wavelengths. Owing to the fact that higher spacer thickness influences the spectral width and in some extent the absorption efficiency for longer wavelengths and thinner spacer results in lower absorption efficiency, we determine $350nm$ to be an appropriate spacer thickness for both $3CS$ and $4CS$.

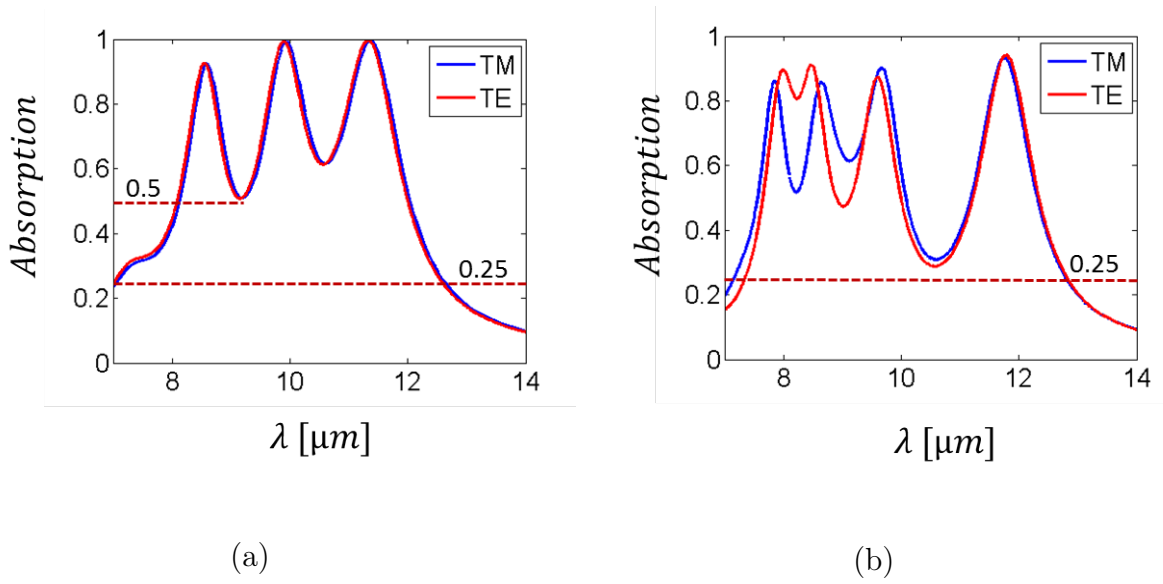


Figure 2.17: Absorption spectra for (a) 3CS (b) 4CS using optimal parameters

The absorption spectra of 3CS and 4CS using the optimal parameters are shown in figure 2.17. The local period Pl , of $2000nm$ and $2250nm$ were used for 3CS and 4CS respectively, while a-Si spacer thickness of $350nm$ was used to calculate the absorption spectra. It can be seen in figure 2.17 (a) that the absorption spectrum for both TE and TM polarization is identical for 3CS. It is because the antenna array 3CS is invariant through the rotation of $\frac{\pi}{2}$ radians about z-axis and when illuminated under normal incidence, its behavior does not depend on the polarization of incidence light [42]. While this is not the case for 4CS. It is therefore sensitive to the polarization of incident wave as can be seen in figure 2.17 (b). For shorter wavelengths the absorption spectra does not have distinct absorption peak unlike that for TM polarization. However, for longer wavelength of incidence wave, absorption is not sensitive to polarization as the absorption efficiency and wavelength of peak absorption is almost identical for both TE and TM polarization. We see that, using differently sized antennas in an array we can tailor near perfect absorption in multiple wavelengths. Following the Kirchhoff's law of thermal radiation, such array

could also be used as multi spectral emitters. Such array could therefore have applications in bolometers, multi spectral thermal imaging, photovoltaic, environment sensing and other potential applications.

2.3.2.1 Angular response periodic patch antenna array

In previous section, we discuss the near perfect absorption using differently sized antennas in a periodic array. We used normal incidence of an incoming wave for an analysis. However, it is important that the absorption characteristic remains unchanged for different polar (θ) and azimuth (φ) angle of incidence. The polar and azimuth angles are defined as shown in figure 2.18 (a). In this section, we study angular response of differently sized antenna to various incidence angles. We use the optimal parameters for antennas 3CS and 4CS described in previous section for study.

Figure 2.18 (b) shows the absorption of antenna arrangement 3CS as a function of wavelength and polar incidence angle(θ) for azimuth angle $\varphi = 0^\circ$. The three resonant absorptions are clearly observed for incidence angle as large as 70° . However, when incidence angle is further increased, slight blue shift in resonant wavelength is observed for shorter wavelengths, along with broadening of absorption spectra. Figure 2.18 (c) and (d) shows the absorption spectra for $\theta = 60^\circ$ and $\theta = 80^\circ$ respectively and azimuth angles $\varphi = 0^\circ, 20^\circ, 40^\circ, 60^\circ, 80^\circ$. It can be seen that the resonance wavelength is insensitive to azimuth angle as it is to polar incidence angle.

Figure 2.19 (a) and (b) shows the absorption of antenna arrangement 4CS as a function of wavelength and polar incidence angle for azimuth angle $\varphi = 0^\circ$ and TM and TE polarization of incident wave respectively. Figure 2.19 (c, d) and (e, f) shows the absorption spectra for $\theta = 20^\circ$ and $\theta = 60^\circ$ respectively and azimuth angles $\varphi = 0^\circ, 20^\circ, 40^\circ, 60^\circ, 80^\circ$.

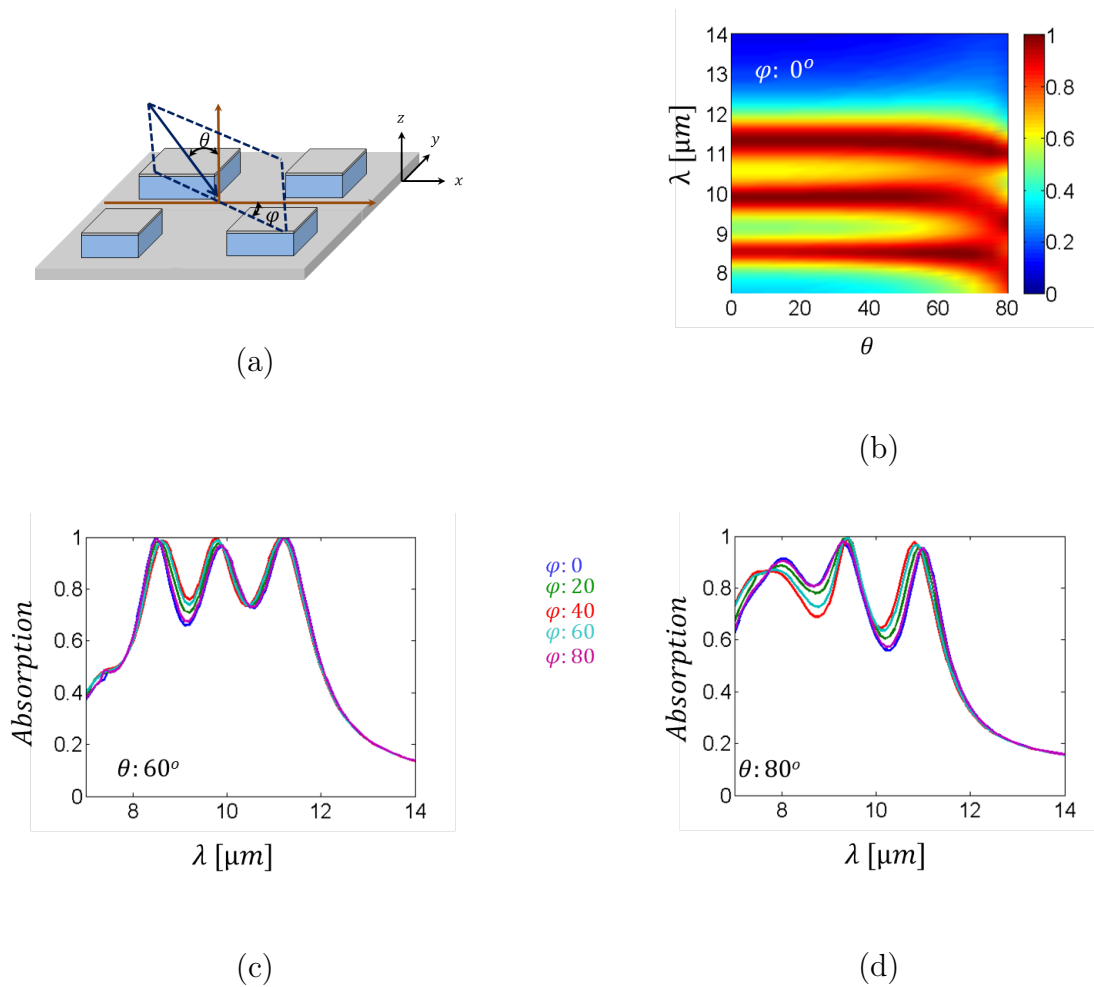


Figure 2.18: (a) Representation of polar(θ) and azimuth (φ) angle of incidence, (b) Absorption of antenna arrangement *3CS* as a function of wavelength and polar (θ) angle of incidence for an azimuth angle $\varphi = 0^\circ$, (c-d) Absorption spectra for various polar angles (c) $\theta = 60^\circ$ (d) $\theta = 80^\circ$ and azimuth angles $\varphi = 0^\circ, 20^\circ, 40^\circ, 60^\circ, 80^\circ$

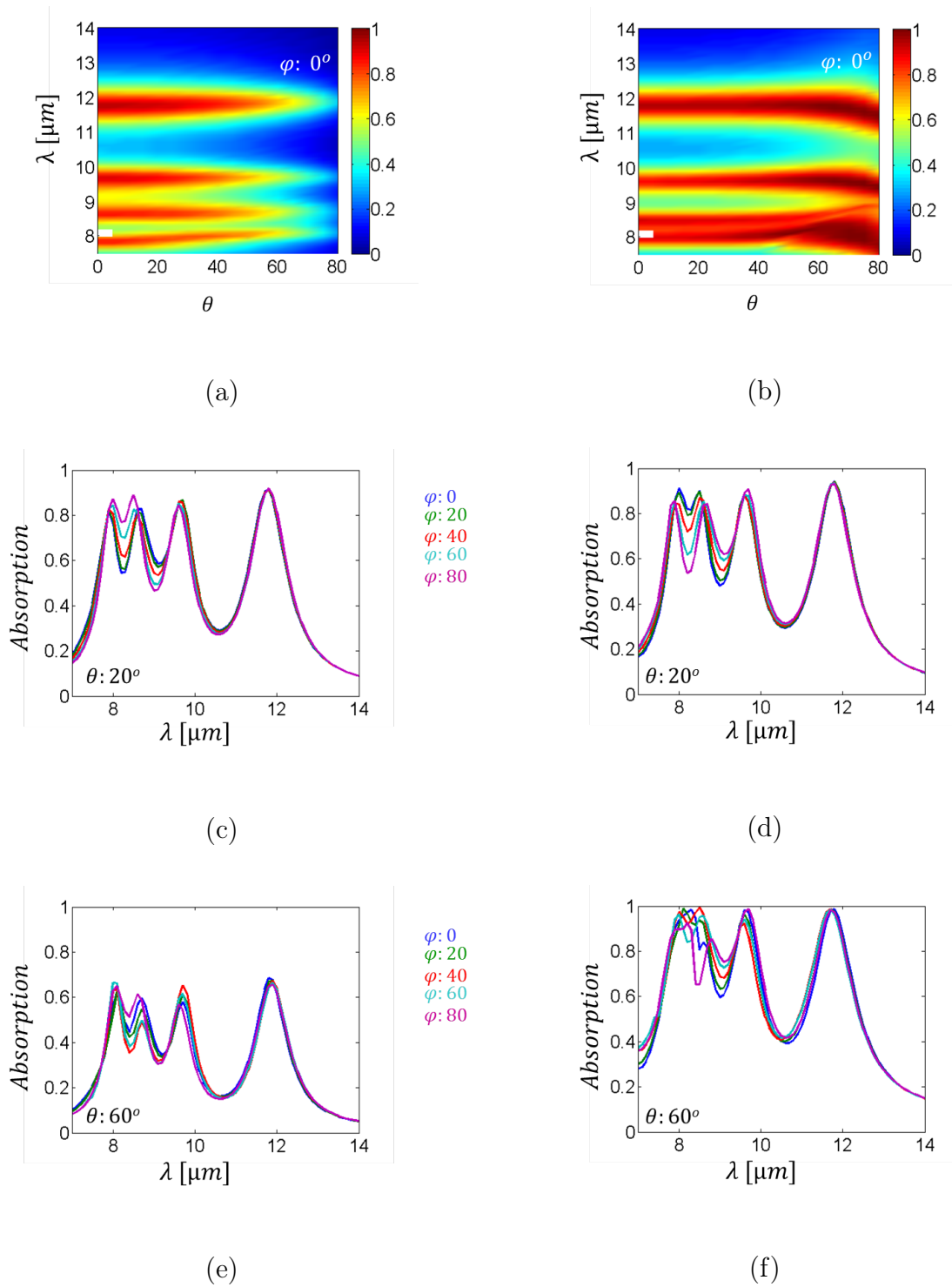


Figure 2.19: Absorption of antenna arrangement 4CS as a function of wavelength and polar (θ) angle of incidence for an azimuth angle $\varphi = 0^\circ$, (a) TM polarization, (b) TE polarization, (c-f) Absorption spectra for various polar angles (c, d) $\theta = 20^\circ$ (e, f) $\theta = 60^\circ$ and azimuth angles $\varphi = 0^\circ, 20^\circ, 40^\circ, 60^\circ, 80^\circ$ for (c, e) TM polarization, (d, f) TE polarization

Figure 2.19 (c, e) shows the absorption spectra for TM polarization whereas figure 2.19 (d, f) shows the absorption spectra for TE polarization for different incidence angles. The four resonant wavelengths appear to be independent to incidence angle for TM polarization. However, for TE polarization, as the polar incidence angle increases, spectral broadening of shorter wavelength is observed. For higher incidence angle $\theta > 40^\circ$ the absorption spectra of antennas resonating at shorter wavelengths overlaps as can be seen in figure 2.19 (b). This makes the individual resonant absorption indistinguishable in spectral plot, instead we observe broadband absorption at those wavelength regions as can be seen in figure 2.19 (f).

For TM polarization of incident wave, the average absorption tends to decrease with increase in polar incidence angle. However, near perfect absorption could still be achieved for TE polarization even at higher incidence angles. It can be seen that for both cases: TE and TM, the resonance wavelength remains insensitive to both polar and azimuth incidence angle, for wide ranges of angular values. This indicates an omnidirectional behavior of antenna array.

2.4 Conclusion

In this section, we present the study of metallic patch antenna to achieve spectral sorting in different spatial location. We emphasized on the importance to effectively collect the incidence light and introduce the concept of absorption and scattering cross section area of an antenna. We point out the important parameters which plays crucial role for effective coupling of incident wave to antenna. We study an isolated patch antenna and array of patch antenna to achieve spectral sorting and high efficiency multi spectral absorption independent to incidence angles. We calculated the optimal antenna parameters to technologically realize such antenna array. In next chapter, we will discuss the fabrication and characterization of the antenna array discussed in this chapter.

Chapter 3

Fabrication and Characterization of optical patch antenna array

In chapter 2, patch antenna arrangement to achieve sorting were discussed. Optical Patch antenna is relatively simple and with differently sized antennas arranged to form an array, it was shown that multi spectral absorption could be tailored with high efficiency. Also it was shown that the incident wave with different energies could be localized in different spatial positions using such arrangement of antenna array. Use of patch antenna array is advantageous from technological point of view as it could be reproduced with high efficacy.

In this chapter, we will present the experimental results for differently sized patch antenna array to tailor multi spectral absorption. We will also present spectral response of an antenna array subjected to different issues and dimensional variation that could occur during fabrication process using numerical techniques.

3.1 Fabrication of optical patch antenna array

The antenna arrays 3CS with patch widths $W1 : 1600nm$, $W2 : 1220nm$, $W3 : 1400nm$ and 4CS with $W1 : 1685nm$, $W2 : 1240nm$, $W3 : 1370nm$ and $W4 :$

1150nm and a - Si spacer thickness (h_{ins}) of 350nm, top metal patch thickness (h_{umet}) of 50nm and ground plate thickness (h_{gp}) of 200nm as described in chapter 2 have been fabricated in CEA-Leti platform in Grenoble. Because of confidentiality issue, the fabrication steps and process are not discussed in this thesis, however the fabrication steps is similar to the one shown in figure 3.1.

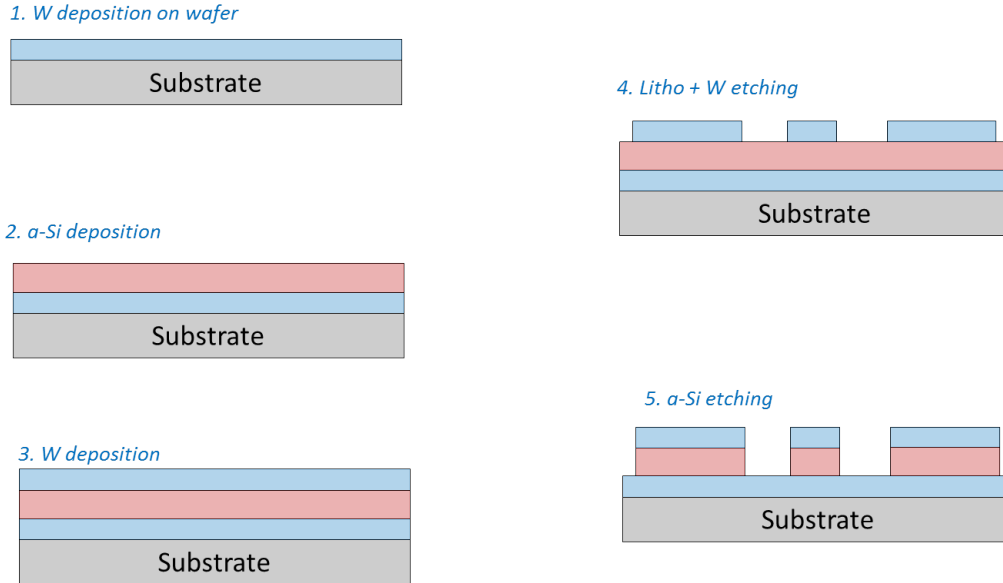
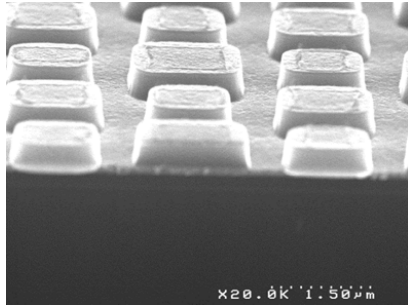


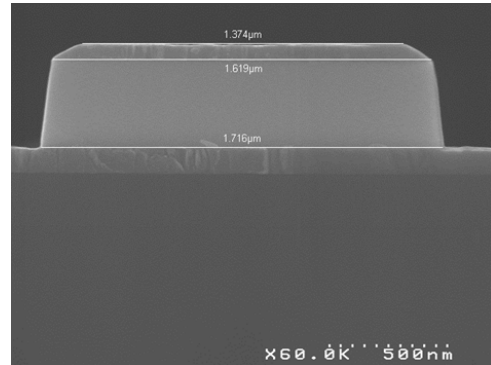
Figure 3.1: Basic fabrication Steps

The optical patch antenna could be fabricated using simple five steps. On substrate, first ground plate tungsten (W) could be deposited (step-1), upon which amorphous silicon (a-Si) of designed thickness could be deposited (step-2). After deposition of silicon, third layer of tungsten (top metal) could be deposited (step-3). Tungsten and silicon could be deposited using LPCVD deposition technique. In fourth step, the lithography process along with etching of top tungsten could be done. For etching of tungsten, electrochemical etching techniques could be used with different combination of etchants like, 1 : 1HF : HNO₃, HCl, H₂SO₄ etc. After etching of top tungsten, silicon can be etched (step-5) using etchant like, KOH, NaOH.

Figure 3.2 (a) and (b) shows tilted and cross section scanning electron microscope (SEM) image of fabricated patchworks of antenna array $3CS$ designed to sort three infrared wavelengths $8.7\mu m$, $10\mu m$ and $11.5\mu m$.



(a)



(b)

Figure 3.2: (a) Tilted SEM image of fabricated antenna array $3CS$, (b) cross section SEM image of fabricated antenna

It can be seen from figure 3.2 that the fabricated patch antenna dimension varies from designed dimensions. Also the antenna face slope are slanted and edges are rounded. This is expected in fabrication as different fabrication steps cannot be controlled with very high accuracy to produce ideal patch antenna with perfect corners and vertical face walls. After fabrication, we characterize the antenna array to study their spectral response. In next section we will discuss the characterization of these fabricated antenna array and discuss the measured spectral response.

3.2 Characterization of antenna arrays

To characterize the spectral response of fabricated antenna array, the reflection between $7\mu m - 14\mu m$ is measured using Fourier transform Infrared spectrometer (FTIR) from Bruker (IFS55). Figure 3.3 shows the sketch of experimental setup used for the characterization of fabricated antenna arrays.

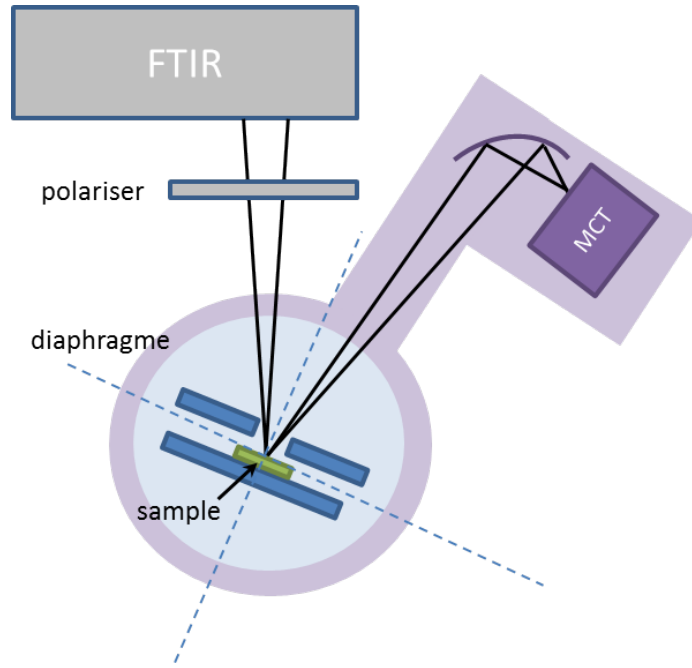


Figure 3.3: Sketch of experimental setup used for characterization of antenna array

The globar infrared source (silicon carbide) and mercury cadmium telluride (HgCdTe) or MCT detector is used in the setup for infrared source and detector respectively. The source aperture of 2.4mm is used in setup, which is incident on sample through 6mm aperture as shown in figure 3.3. 90° off axis parabolic mirror with 38mm parent focal length is used as the collection mirror to collect the reflected light from sample which is then detected by MCT. The reflection from the antenna array is divide by the reflection of gold mirror to find the normalized reflection spectra. The absorption of an antenna array is then calculated using $A = 1 - R$, where A is the absorption of an antenna array and R is the normalized reflection of antenna array.

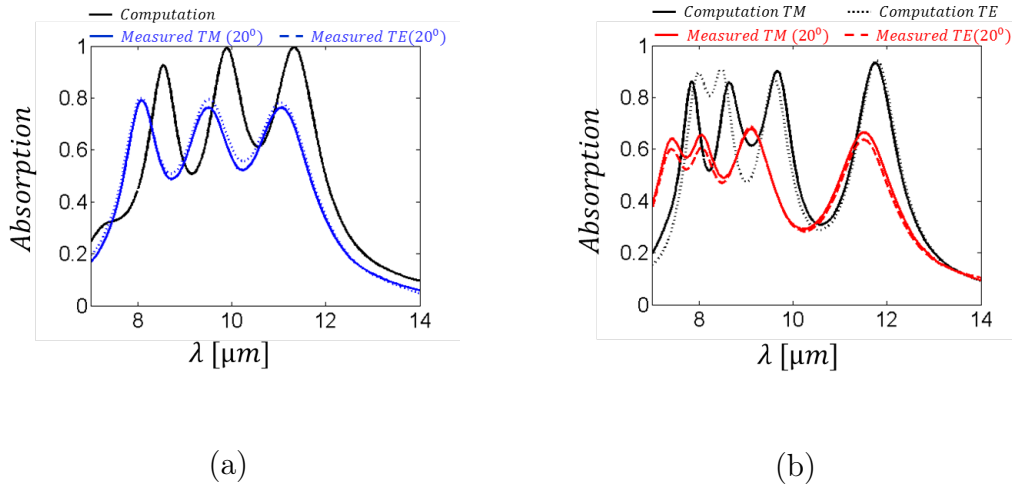


Figure 3.4: Measured and computed absorption spectra of antenna array (a) 3CS, (b) 4CS for both TE and TM polarization

Figure 3.4 (a) and (b) shows the absorption spectra of 3CS and 4CS respectively measured for an incidence angle of 20° for both *TE* and *TM* polarization. Also the computed absorption spectra for the antenna array without considering the dimensional variation and error in refractive index of core ($n_{(a-Si)} : 3.6$) is shown for comparison. Figure 3.5 (a) and (b) shows the absorption measured at different incidence angles: 20° , 22° and 25° for fabricated antenna arrays 3CS and 4CS respectively.

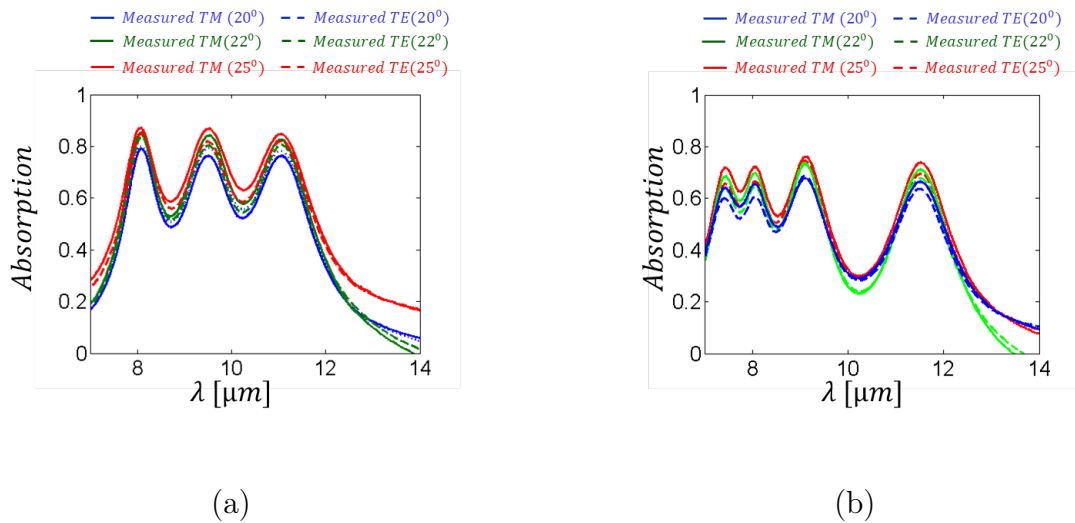


Figure 3.5: Measured absorption spectra for different incidence angles: 20° , 22° and 25° for TE and TM polarization, (a) 3CS, (b) 4CS

In figure 3.4 (a-b) and figure 3.5 (a-b) it is clearly visible that using differently sized antenna array, a multi spectral absorption detector could be designed with efficiency higher than 70% and 60% for antenna array *3CS* and *4CS* respectively. However, the blue shift in wavelengths of peak absorption and reduction in absorption is also observed compared to computed absorption spectra for both antenna arrays *3CS* and *4CS*. We saw in figure 3.2 different fabrication processes and steps could lead to dimensional variation of an antenna from its original design. It is therefore important to study the spectral response of the antenna array subjected to different dimensional variation to achieve accurate agreement between numerical simulation and experimental behavior. In next section, we will address the effect of dimensional variation on spectral response of the antenna array. Later we present the comparison of more accurate antenna model incorporating fabrication errors and experimental results for differently sized antennas arranged in an array to tailor multi spectral absorption.

3.3 Dimensional variation and spectral response

Different techniques like photo-lithography, electron-lithography, atomic layer depositions (ADL), low power chemical vapor deposition (LPCVD) are widely used for fabrication of nano- and micro-structures in optics. Precision control techniques are required to realize the exact transfer of numerical design to fabricated device. However, depending on the fabrication processes and steps dimensional variation is generally expected in fabricated device. For example, when we fabricate the array of square patches, the rounded corners are generally expected. Also the etching process induces the slant angle in vertical directions which could change the optical response of the final device. The deviation of optical response might be small or huge depending on the precision control of fabrication steps. Understanding the

effect of dimensional variation on optical response could therefore facilitate the process variation. In this section, we will discuss the effect of dimensional variation on spectral response of the patch antenna array designed to achieve multi spectral absorption.

3.3.1 Variation in Patch size

In this section, we study the effect of patch size variation on spectral response of the periodic antenna array designed to achieve multi spectral absorption. The resonance wavelength of patch antenna varies linearly with patch width as given by relation 2.1. For the periodic array of differently sized antennas, variation in patch size could change the resonance wavelengths from desired values, given the core index does not changes.

We use the periodic antenna array 3CS, described in section 2.3.2 as a reference for this study. In figure 3.6 (a) we recall the unit cell of antenna array 3CS, where we use three different antenna patches $W1 : 1600nm$, $W2 : 1220nm$ $W3 : 1400nm$ arranged in square lattice with local period $Pl : 2000nm$. 3.6 (b) shows the conceptual diagram of patch size variation, where Δ is used to scale the patch size. With Pl fixed to $2000nm$, Δ is varied from -10% to $+10\%$. Figure3.6 (c) shows the absorption of antenna array 3CS as a function of Δ and wavelengths.

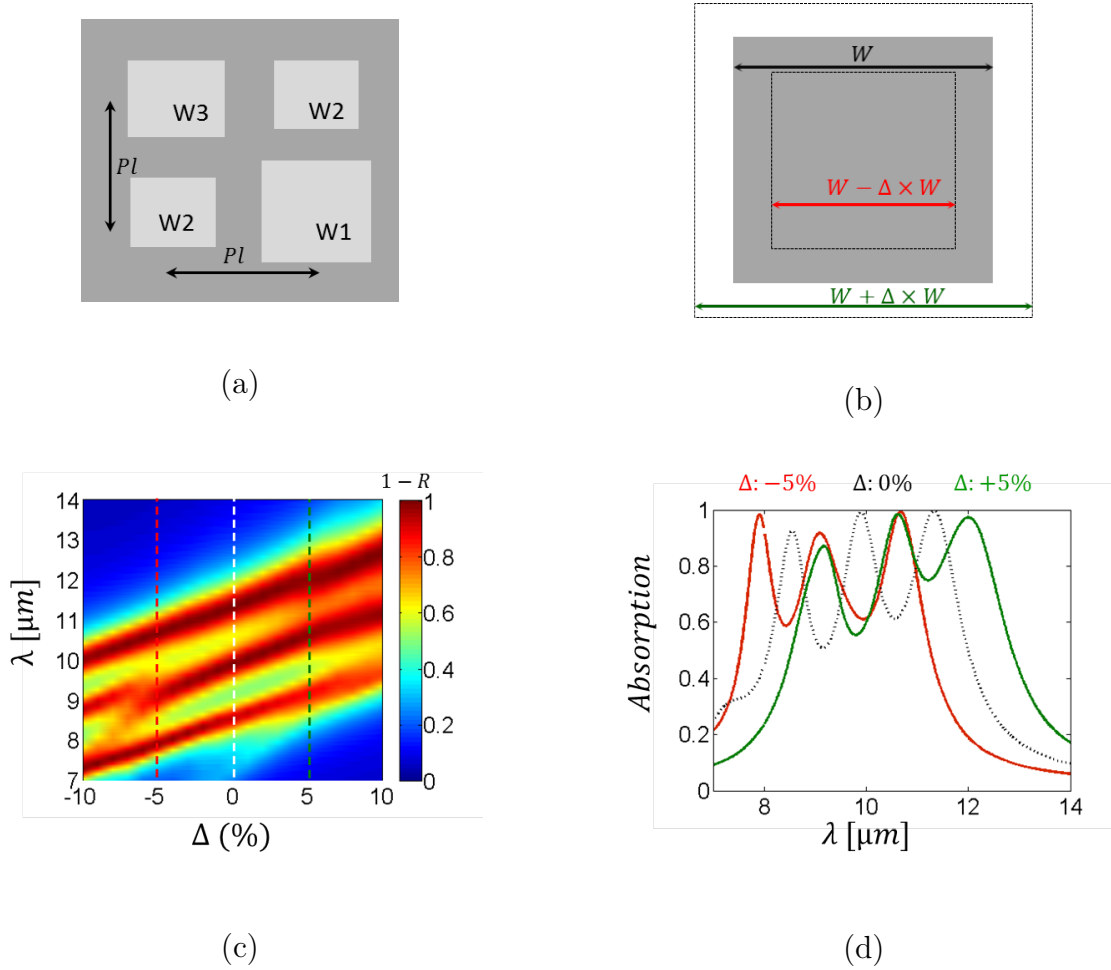


Figure 3.6: (a) Unit cell of periodic antenna array 3CS ,(b) Conceptual diagram showing the patch size variation of individual patch antenna in periodic array 3CS ,(c) Absorption as a function of Δ and wavelength for antenna array 3CS, (d) Absorption as function of wavelength for different Δ . The spectrum corresponds to the vertical cross cuts shown in (c).

It can be seen that the resonance wavelength of individual patch antenna in an array blue shifts when $\Delta < 0$ and red shifts when $\Delta > 0$ in accordance to relation 2.1. Broadening of absorption spectrum is observed with increase in Δ , meanwhile average absorption of antenna array remains above 70%. Figure 3.6 (d) shows the absorption spectrum as a function of wavelength for $\Delta : -5\%$, 0% and $+5\%$ respectively which corresponds to the vertical cross cuts shown in figure 3.6(c). We see that even for the patch size variation as small as $\pm 5\%$ the individual resonance

peak changes by $\sim 500nm$. It is therefore, very important to reduce this variation to achieve the resonance at desired wavelengths.

3.3.2 Rounding of patch edge

The fabrication techniques and process steps for square patch introduce the rounding effects, especially at the patch edges and corners. This could change the spectral response of the antenna array. In this section we study the effect of edge rounding on spectral response of antenna arrays $3CS$ with patch widths, $W1 : 1600nm$, $W2 : 1220nm$ $W3 : 1400nm$ and $4CS$ with patch widths $W1 : 1685nm$, $W2 : 1240nm$, $W3 : 1370nm$ and $W4 : 1150nm$, as described in section 4.4. The other parameters, upper metal patch thickness and $a-Si$ spacer thickness is kept constant to designed value of $50nm$ and $350nm$ respectively.

Suppose we have to introduce the rounded edge with radius R such that $2R \leq W$. This can be done by creating composite structure which consists of five cuboids and four quarter cylinders as shown in figure 3.7 (a). To study the antenna array with different edge roundness, we introduce the scaling factor r which creates the cylinder whose radius is proportional to half width of the patch:

$$R = r \times \frac{W}{2} \quad (3.1)$$

When $r = 0$, we get ideal patch edge, while $r \neq 0$, we get the rounded edge with radius given by equation 3.1 whose center moves along the diagonal of the square patch as shown in figure 3.7 (b). In the extreme case when $r = 1$, we get the circular patch with radius $R = \frac{W}{2}$. Figure 3.7 (c-d) shows the top view of corner shapes for different values of r .

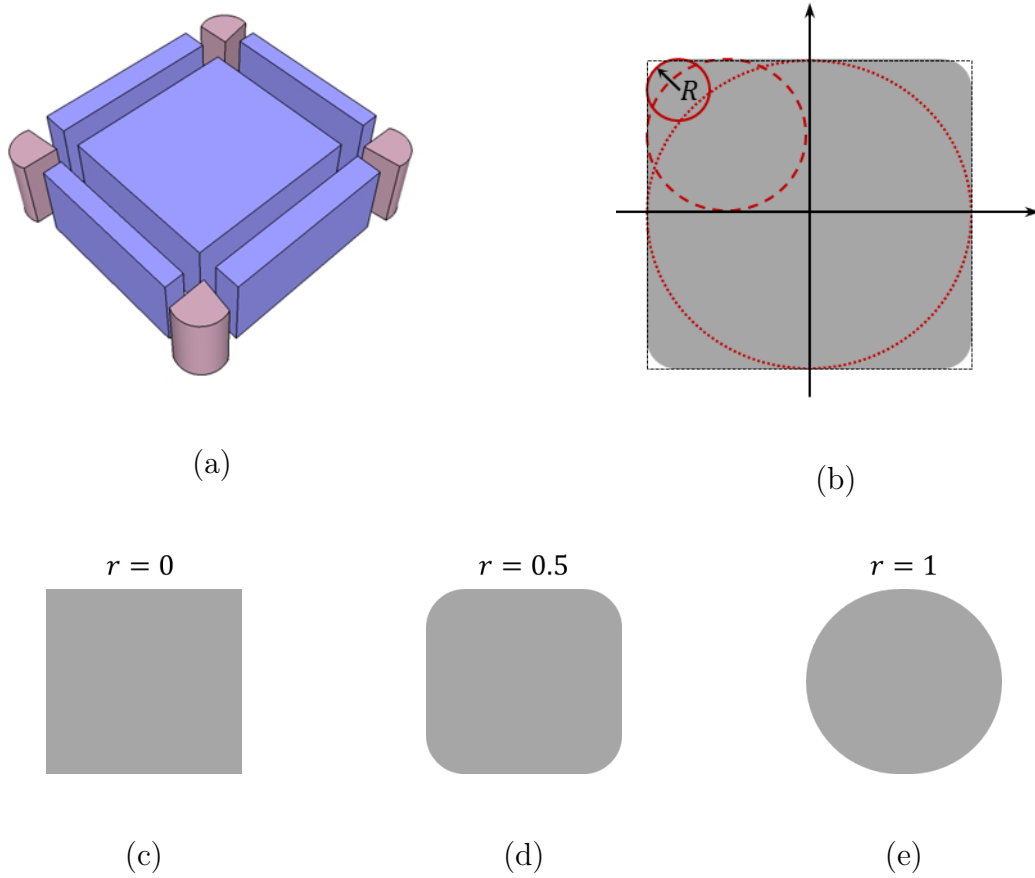


Figure 3.7: (a) Individual structures which creates the rounded patch (b) Top view of rounded patch showing the center of cylindrical patch edge and its trajectory (c-d) top view of patch for different scaling factor r

The patch edges in the antenna array $3CS$ and $4CS$ were rounded whose radius is a fraction of its individual width as given by relation 3.1. This means that, the individual patches in an array does not have same radius of roundness but have the common scaling factor r . Figure 3.8 (a) shows the absorption as a function of scaling factor r and wavelength for antenna array $3CS$ for TM polarization of incidence wave. Similarly figure 3.8 (c) and (e) shows the absorption of antenna array $4CS$ for TM and TE polarization of incidence wave respectively.

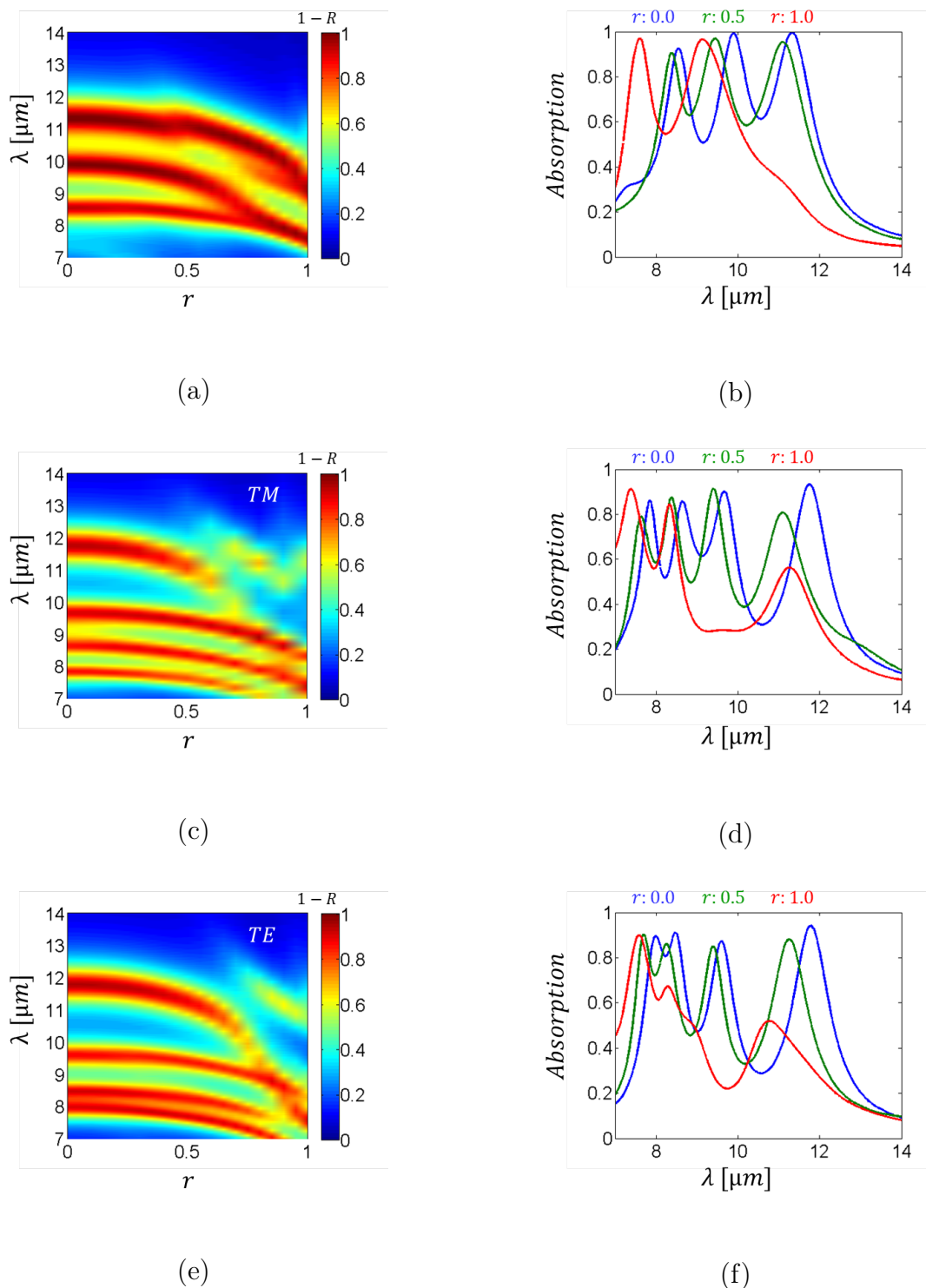


Figure 3.8: Absorption as a function of scaling factor r and wavelength (a) for 3CS (c) 4CS for TM polarization of incidence wave (e) 4CS for TE polarization of incidence wave, Absorption as a function of wavelength for various scaling factor ($r = 0, 0.5, \text{and } 1$) (b) for 3CS (d) 4CS for TM polarization of incidence wave (f) 4CS for TE polarization of incidence wave

It can be seen that the wavelength of absorption peak (or resonance wavelength) of each antenna in array exhibits the common trend. As the antenna patch is gradually deformed from square into circle by increasing the radius of edge roundness, the wavelength at which antennas resonate blue shifts significantly. This blue shift of resonance wavelength on increasing the radius of roundness is attributed to the spread-out charge distribution on the edges and faces of metal interfaces [43]. It can be seen that the resonance wavelength blue shifts faster when scaling factor is higher ($r > 0.5$). Interestingly, in antenna array 3CS for specific scaling factors, overlap of resonance wavelength of two antennas in an array is observed as visible in figure 3.8 (a) for $r \geq 0.7$. Therefore only two resonance absorption is observed for higher degree of edge roundness ($r \geq 0.7$). Whereas for antenna array 4CS, when $r > 0.7$ absorption tends to decrease for longer wavelengths. Figure 3.8 (b), (d) and (f) shows the absorption as a function of wavelength for various values of scaling factor ($r = 0, 0.5, \text{ and } 1$) corresponds to absorption maps shown in figure 3.8 (a), (c) and (e) respectively.

It is shown that the edge roundness does affect the resonance of patch antenna and magnitude of absorption of resonant wavelengths. It is therefore important to consider this effect while modeling the multi spectral absorption using differently sized antenna array, to achieve better agreement with the experimental behavior.

3.3.3 Variation in antenna stack slope

Other non-idealities that could occur during fabrication process of patch antenna are non-vertical side faces of antenna stack. Due to the etching process of metal and $a-Si$, the side faces are generally slanted. The slope angle relative to surface normal of ground plate depends on the etching method, etching rate and chemical used. In this section we study the effect of slope angle in spectral response of an antenna array.

For a patch antenna array we learned in previous sections that the antenna width determines the resonance wavelength. The ideal situation would be to be able to fabricate an antenna stack with same width of core material in both top metal patch interface and bottom ground plate interface. For simplicity, we would call the width of core material in the top metal patch interface, top width (W_{top}) and that in ground plate interface, bottom width (W_{bottom}). However, due to the non-idealities introduced by etching process, it is convenient to target either top width or bottom width of antenna stack to acquire the designed value. Many variations have to be considered to exactly model the effect of stack slope, for example the rounded edges and corners, different slope of top metal patch, index variation of core material has also to be included within the model to accurately match the experimental results. However, the effect could be studied step by step starting with simple case and then introduce more non-idealities. We study the different cases to understand the effect of slope variations.

3.3.3.1 Target: Bottom width (W_{bottom})

First we consider the simple case where the bottom width is targeted to acquire designed width as shown in figure 3.9 (a). Figure 3.9 (a) shows the cross section of square patch in which shaded region is the materials that are etched during the process. The slope angle (θ) is considered relative to surface normal of ground plate at the edge of the patch as shown.

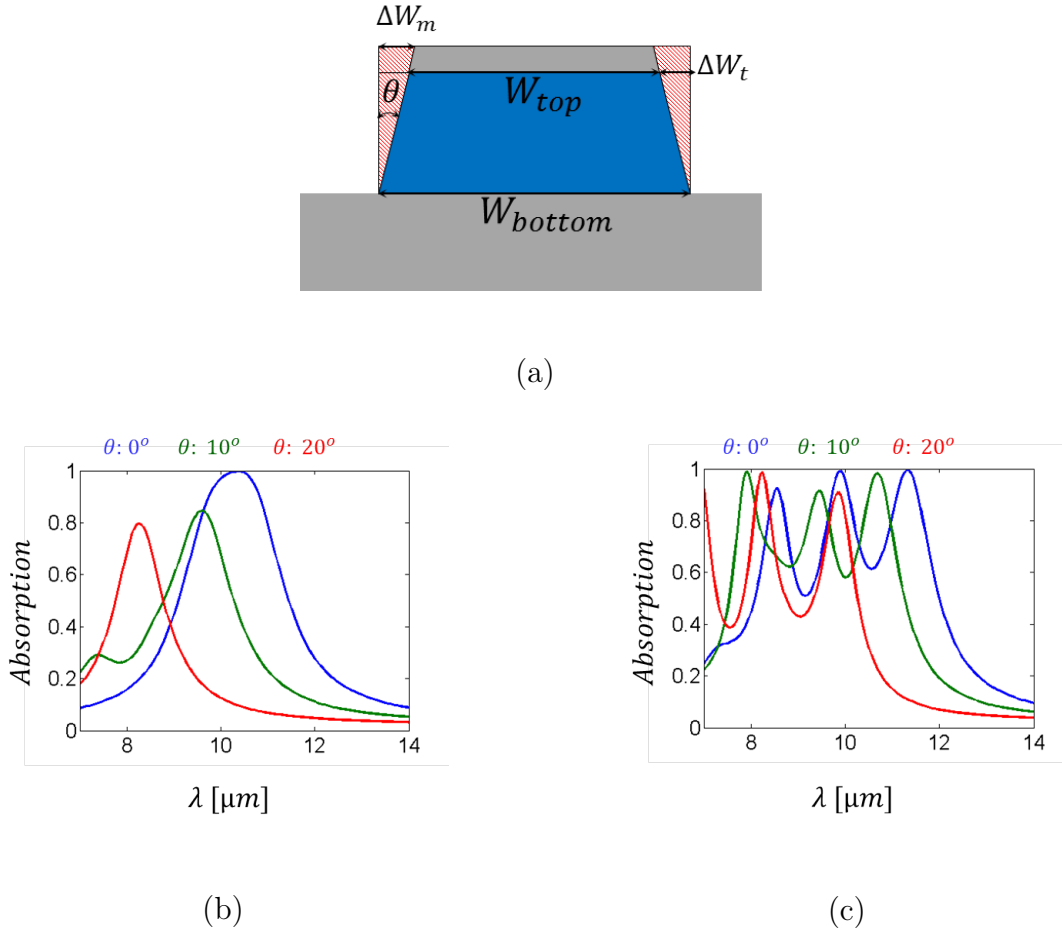


Figure 3.9: Schematic for bottom width target (b) absorption as a function of wavelength of periodic antenna width patch width $W : 1400nm$ and period $P : 2000nm$ (c) absorption as a function of wavelength of antenna array 3CS for different slope angles

When the slope angle is introduced, the top width (W_{top}) and top metal width ($W_{t-metal}$) at superstrate–metal interface are smaller than bottom width (W_{bottom}). These widths can be calculated as:

$$W_{top} = W_{bottom} - 2 \Delta W_t \quad (3.2)$$

$$W_{t-metal} = W_{bottom} - 2\Delta W_m \quad (3.3)$$

Where ΔW_t and ΔW_m are dependent on slope angle:

$$\Delta W_t = h_{ins} \tan(\theta) \quad (3.4)$$

$$\Delta W_m = (h_{ins} + h_{umet}) \tan(\theta) \quad (3.5)$$

Figure 3.9 (b) shows the absorption of antenna array with patch width $W : 1400nm$ arranged periodically in square lattice with array period $P : 2000nm$ for different slope angles ($\theta = 0^\circ, 10^\circ, 20^\circ$). The a-Si core height (h_{ins}) and tungsten top metal thickness (h_{umet}) of $350nm$ and $50nm$ were considered respectively. It can be seen that the resonance wavelength blue shifts significantly along with in decrease in absorption when the slope angle is varied from $0^\circ - 20^\circ$. Similar trend can be seen for the antenna array $3CS$ as shown in figure 3.9 (c) as the slope angle is varied. We assume this blue shift of resonance is due to decrease in top width (W_{top}) of antenna array as slope angle increases.

Using relation 2.1 which relates the resonance wavelength with width of antenna patch, we can calculate the resonance wavelength for various slope angles. When slope angle ($\theta = 0^\circ$), the top width and bottom width are same, therefore

$$\lambda_{\theta=0} = 2n_{eff} W_{bottom} \quad (3.6)$$

For slope angle ($\theta \neq 0^\circ$), we assume resonance is determined by top width W_{top} :

$$\lambda_{\theta \neq 0} = 2n'_{eff} W_{top} \quad (3.7)$$

Where, n_{eff} and n'_{eff} are the mode index of an antenna with vertical and slanted side faces respectively. Taking the ratio $\lambda_{\theta \neq 0}$ to $\lambda_{\theta=0}$ and using relations 3.2 and 3.4, we get:

$$\frac{\lambda_{\theta \neq 0}}{\lambda_{\theta = 0}} = \frac{n'_{eff}}{n_{eff}} \left(1 - \frac{2h_{ins} \tan(\theta)}{W_{bottom}} \right) \quad (3.8)$$

We see that the resonance of wavelength for antenna with slanted side face depends on two factors: the slope angle (θ) and the mode index ratio $\frac{n'_{eff}}{n_{eff}}$.

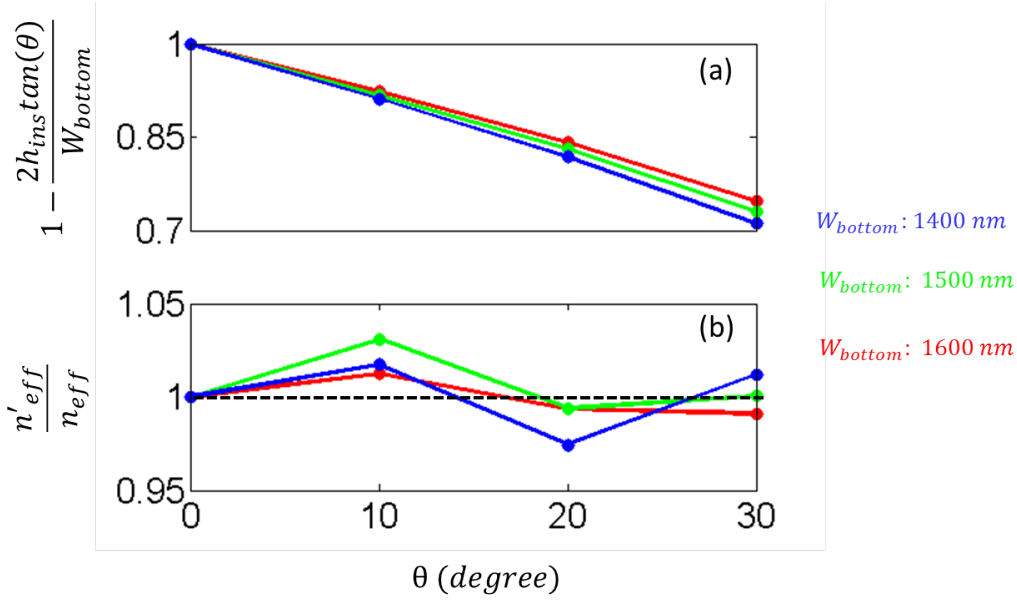


Figure 3.10: (a) $\left(1 - \frac{2h_{ins} \tan(\theta)}{W_{bottom}}\right)$ and (b) $\frac{n'_{eff}}{n_{eff}}$ as a function of slope angle (θ) for various patch widths ($W : 1400 \text{ nm}, 1500 \text{ nm}$ and 1600 nm)

Figure 3.10 shows the term inside bracket in right hand side of equation 3.8 and the ratio $\frac{n'_{eff}}{n_{eff}}$ calculated for different antenna array with patch widths $W_{bottom} : 1400 \text{ nm}, 1500 \text{ nm}, 1600 \text{ nm}$ for various slope angles (θ). The term $\left(1 - \frac{2h_{ins} \tan(\theta)}{W_{bottom}}\right)$ in equation 3.8 decreases with increase in slope angle for given bottom width of antenna stack as can be seen in figure 3.10 (a). If there were no blue shift of absorption spectra then the ratio $\frac{n'_{eff}}{n_{eff}}$ should increase accordingly. However, it remains almost constant when slope angle of slanted side face is increased as shown in figure 3.10 (b). The black dotted line in figure 3.10 (b) shows the reference with $\frac{n'_{eff}}{n_{eff}} = 1$.

It can therefore be said that the blue shift in absorption spectra as shown in figure 3.9 (b) and (c) is due to the decrease in top width of antenna stack when slope angle is increased. It can also be said that the resonance wavelength of an antenna is determined by the top patch width. To achieve better agreement in resonance condition between the numerical design and fabricated antenna array, one should therefore target the top width (W_{top}) of antenna stack to acquire design value.

3.3.3.2 Target: Top width (W_{top})

We now study how the spectral response of patch antenna gets affected when the top width of antenna stack is targeted to acquire designed value. Figure 3.11 (a) shows the cross section of antenna stack in which the region shaded in green is the excess core material relative to the vertical side face. The region shade in red is the top metal which is etched during the process. We vary the stack slope angle (θ) relative to vertical side face as shown in figure 3.11 (a). The slope of excess core material and etched top metal patch is considered to have same value for the analysis.

For the given slope angle (θ), the bottom width (W_{bottom}) is larger and the top metal width ($W_{t-metal}$) in superstrate-metal interface is smaller than the top width (W_{top}) which are given by:

$$W_{bottom} = W_{top} + 2\Delta W_b \quad (3.9)$$

$$W_{t-metal} = W_{top} - 2\Delta W_m \quad (3.10)$$

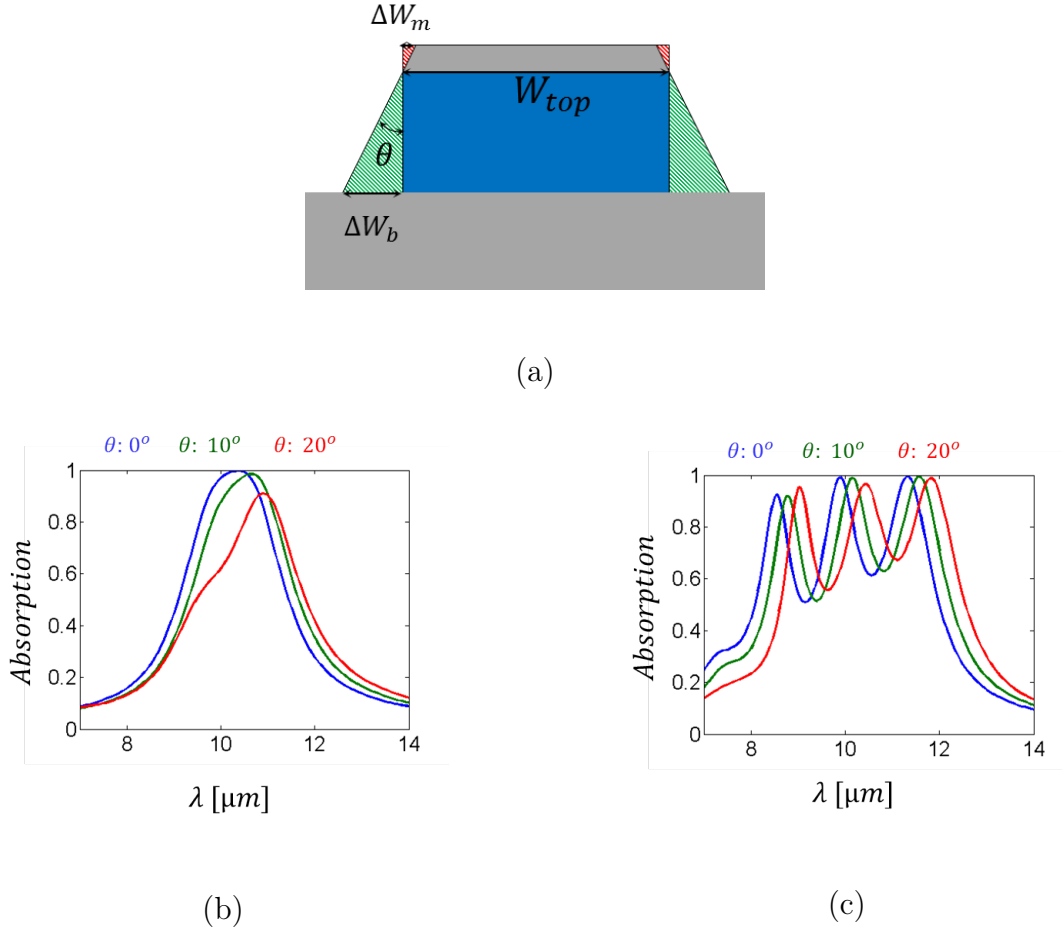


Figure 3.11: (a) Schematic for top width target (b) absorption as a function of wavelength of periodic antenna width patch width $W : 1400nm$ and period $P : 2000nm$ (c) absorption as a function of wavelength of antenna array 3CS for different slope angles

Where ΔW_b and ΔW_m are dependent on slope angle:

$$\Delta W_b = h_{ins} \tan(\theta) \quad (3.11)$$

$$\Delta W_m = h_{umet} \tan(\theta) \quad (3.12)$$

Figure 3.11 (b) shows the absorption as a function of wavelength for an antenna array with patch width $W : 1400nm$ arranged periodically in square lattice with array period $P : 2000nm$ for different slope angles ($\theta = 0^\circ, 10^\circ, 20^\circ$). The a-Si core

height (h_{ins}) and tungsten top metal thickness (h_{umet}) were kept constant to the values considered in previous section. It can be seen that the absorption spectra red shifts when slope angle is increased. Similar trend can be seen in absorption spectra of antenna array 3CS as shown in figure 3.11(c), when slope angle of slanted side face is increased.

However, the absorption spectra red shifts slowly compared to blue shift due to decrease in top metal width discussed in previous section. From previous section we know that the top width of antenna stack determines the resonance wavelength. The red shift in absorption spectra as seen in figure 3.11 (b) and (c) with fixed top width therefore should arise due to increase in effective index of the antenna array. To validate this assumption, we follow the similar approach as in previous section to find the ratio of resonance wavelengths with slanted side face ($\theta \neq 0^\circ$) to that with vertical side face ($\theta = 0^\circ$):

$$\frac{\lambda_{\theta \neq 0}}{\lambda_{\theta = 0}} = \frac{n'_{eff}}{n_{eff}} \left(1 - \frac{2h_{ins}\tan(\theta)}{W_{top} + 2h_{ins}\tan(\theta)} \right) \quad (3.13)$$

Where n'_{eff} and n_{eff} are the effective index of antenna array with and without slanted side faces respectively. Figure 3.12 shows the term inside bracket in right hand side of equation 3.13 and the ratio $\frac{n'_{eff}}{n_{eff}}$ calculated for different antenna array with patch widths $W_{top} : 1200nm, 1300nm, 1400nm$ for various slope angles (θ). For fixed top width (W_{top}) it can be seen that the term in bracket in right hind side of equation 3.13 decreases with increase in slope angle (θ) as shown in figure 3.12 (a).

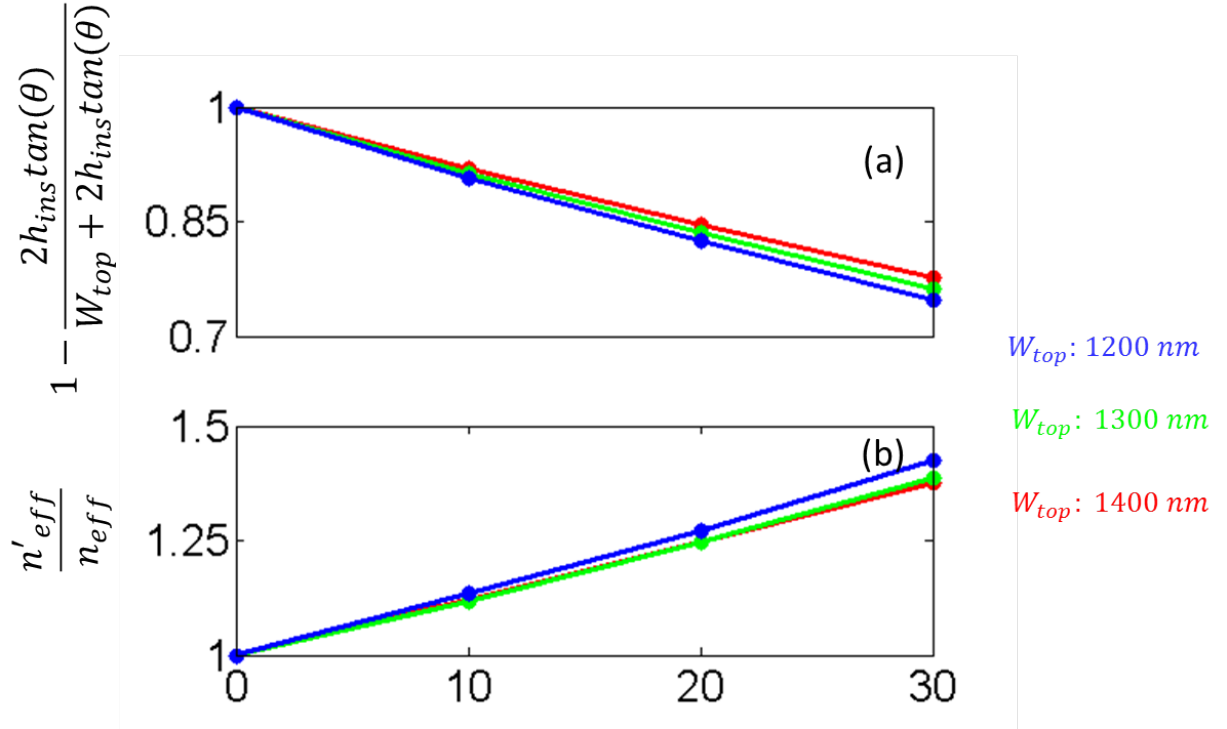


Figure 3.12: (a) $\left(1 - \frac{2h_{ins}\tan(\theta)}{W_{top} + 2h_{ins}\tan(\theta)}\right)$ and (b) $\frac{n'_{eff}}{n_{eff}}$ as a function of slope angle (θ) for various patch widths ($W : 1200\text{nm}, 1300, 1400\text{nm}$)

The ratio $\frac{n'_{eff}}{n_{eff}}$ calculated for antenna array with different patch widths are shown in figure 3.12 (b). It can be seen that the ratio increases significantly with increase in slope angles. The simultaneous increase of ratio $\frac{n'_{eff}}{n_{eff}}$ and decrease of term $1 - \frac{2h_{ins}\tan(\theta)}{W_{top} + 2h_{ins}\tan(\theta)}$ in equation 3.13 counteract each other and tries to keep the resonance wavelength at same position. However due to higher rate of change of ratio $\frac{n'_{eff}}{n_{eff}}$ compare to term $1 - \frac{2h_{ins}\tan(\theta)}{W_{top} + 2h_{ins}\tan(\theta)}$ induce slight red shift of absorption spectra which is visible in figure 3.11 (b) and (c). Higher rate of change of ratio $\frac{n'_{eff}}{n_{eff}}$ indicates that the mode index of antenna increases due to additional insulator material in the core compared to its vertical face antenna counterpart.

We can therefore allow the top width to be smaller than the designed value allowing slanted side faces of antenna stack to achieve better agreement between numerically calculated absorption spectra and that of fabricated antenna array. The new top width can be calculated using equation 3.13 knowing all other parameters. However,

finding new value of top width is non-trivial as the etching of material and thus the slope angles induced are purely dependent on process parameters.

3.3.3.3 Target: Top width(W_{top}), different angles for etched top metal and excess core material

In the previous two cases, we targeted the top width (W_{top}) and bottom width (W_{bottom}) to acquire the designed value and introduce the slope for side faces of the antenna stack. In both cases the slope of top metal patch were considered to have same values as the slope of core material. However, the metal patch could have different slope angle compared to the slope of core material. In this section we consider different slope angles for core material and top metal patch of antenna stack while targeting the top width to acquire designed patch width.

Figure 3.13 (a) shows the cross section of antenna patch, in which the region shaded in green is the excess core material relative to the vertical side face. The region shaded in red is the top metal which is etched during the process. We vary the core slope angle (θ_h) and metal slope angle (θ_m) relative to vertical side face as shown in figure 3.13 (a). Figure 3.13 (b) shows the absorption spectra as a function of wavelength for fixed core slope ($\theta_h : 20^\circ$) and various metal slopes ($\theta_m : 40^\circ, 60^\circ, 80^\circ$) for the antenna array 3CS with patch widths, $W1 : 1600nm, W2 : 1220nm, W3 : 1400nm$ arranged periodically. The absorption spectrum of ideal antenna stack with vertical side faces ($\theta_h = \theta_m = 0^\circ$) is shown as a reference in black dotted line. The red shift of absorption spectra for non-ideal antenna stack with slopes is attributed to increase in effective index of antenna array as discussed in previous section.

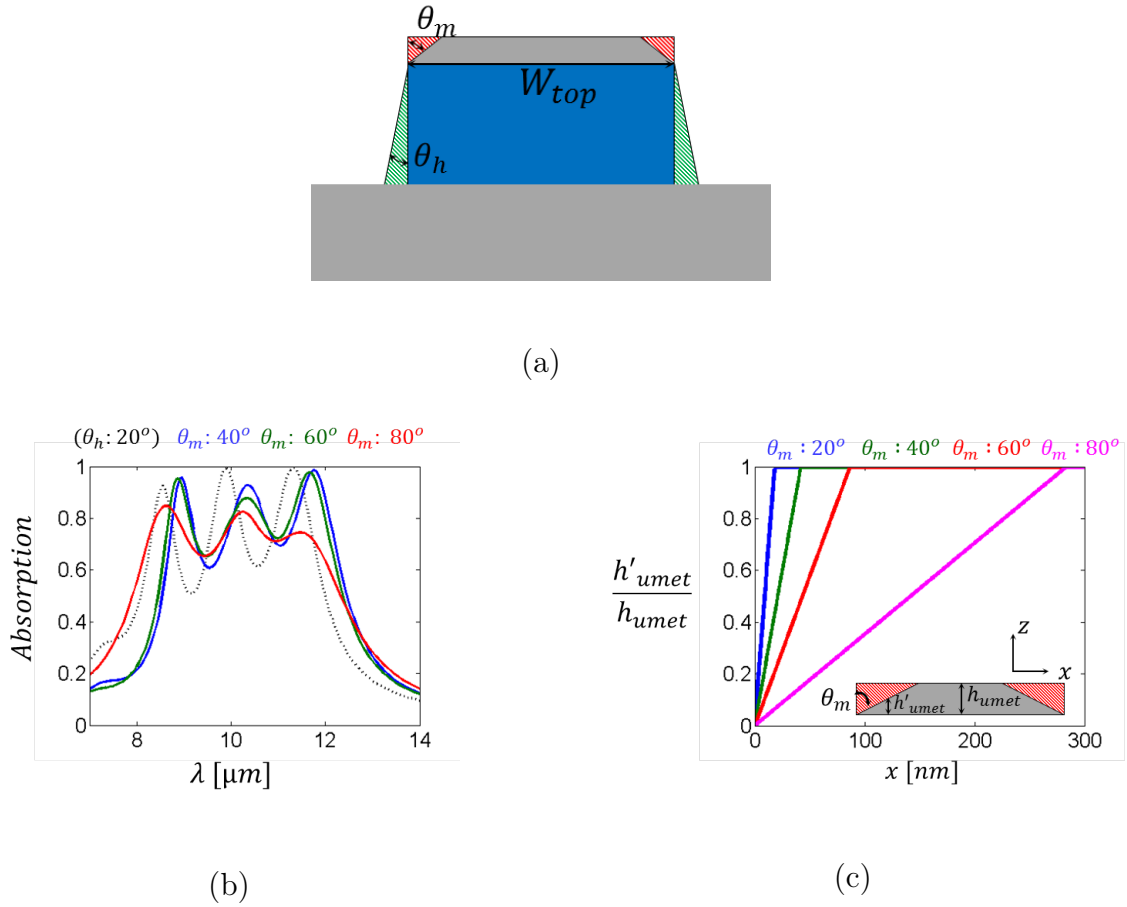


Figure 3.13: Schematic for top width target with different slope angle for core material and top metal patch (b) absorption as a function of wavelength of antenna array 3CS for various metal slopes ($\theta_m : 40^\circ, 60^\circ, 80^\circ$) with fixed core slope ($\theta_h : 20^\circ$) (c) metal thickness at the edge of antenna patch normalized to designed metal thickness (h_{umet}) for various metal slopes ($\theta_m : 20^\circ, 40^\circ, 60^\circ, 80^\circ$)

It can be seen that for fixed core slope of 20° the wavelength of peak absorption does not change significantly, when metal slope is increased to the value as large as 60° . However for higher slope angle blue shift of absorption spectra is observed along with decrease in average absorption of the antenna array. This could be attributed to decrease in metal thickness at the edge of antenna patch as the metal slope increases. Figure 3.13 (c) shows the metal thickness at the edge of antenna patch normalized to design metal thickness (h_{umet}) for various metal slope angles (θ_m) as a function of spatial position (x). The inset in figure 3.13 (c) illustrates the parameters considered

for calculating the ratio $\frac{h'_{umet}}{h_{umet}}$. h'_{umet} is the metal thickness along the spatial position (x) for which the metal is etched away and has slanted face.

It can be seen that for higher slope angles, the metal thickness at the edges of antenna could be significantly less than the designed value. This could decrease the effective width of the patch which in turns results in blue shift of resonance wavelength of an antenna. Moreover, the lower thickness of the top metal edge for considerable width of top metal patch could induce the transparency for longer wavelength, broadening the spectral response, as is visible in figure 3.13 (b) for ($\theta_m : 80^\circ$).

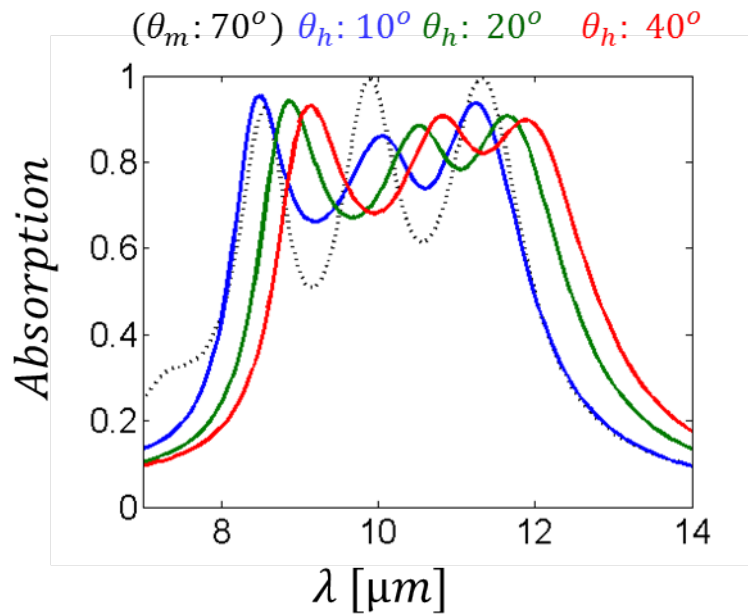


Figure 3.14: Absorption as a function of wavelength of antenna array 3CS for various core slopes ($\theta_h : 10^\circ, 20^\circ, 40^\circ$) with fixed metal slope ($\theta_m : 70^\circ$)

Figure 3.14 shows the absorption spectra of antenna array 3CS for various slopes of core material ($\theta_h : 10^\circ, 20^\circ, 40^\circ$) with fixed metal slope angle ($\theta_m : 70^\circ$). The absorption spectrum of ideal antenna stack is shown as a reference in black dotted line. With increase in core angles the absorption spectrum of antenna array red shifts as visible in figure 3.14. The red shift is attributed to increase in effective index of antenna array. It can be seen that the average absorption is lower than that of ideal antenna array for all the core angles considered. Moreover, the spectral

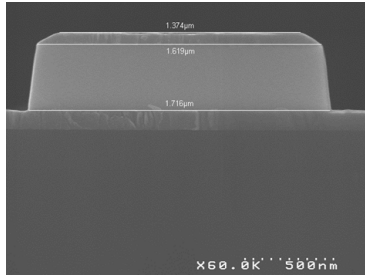
broadening can be observed for longer wavelengths. This spectral broadening can be attributed to lower thickness of top metal patch at the edges for given metal slope of 70° .

Interestingly, the absorption peaks do not vary significantly for the antenna array with core slope angle of 10° compared to ideal antenna array. This indicates that even with larger portion of metal etched at the edges of top metal patch, slope of core material could be controlled to achieve accurate agreement between the designed and experimental resonance wavelengths.

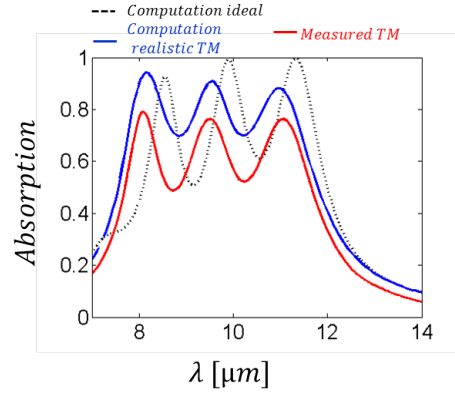
3.4 Comparison of realistic antenna modeling and experimental result

As discussed in previous sections, the dimensional variation and variation in index of the material is expected while fabricating the designed antenna arrays. The designed dimensions for 3CS were, $W1 : 1600nm$, $W2 : 1220nm$, $W3 : 1400nm$ and that for 4CS were, $W1 : 1685nm$, $W2 : 1240nm$, $W3 : 1370nm$ and $W4 : 1150nm$. While the $a - Si$ spacer thickness (h_{ins}) of $350nm$, top metal patch thickness (h_{umet}) of $50nm$ and ground plate thickness (h_{gp}) of $200nm$ were designed for antenna arrays. From the SEM images of the fabricated array, we find 1.25% increase in the top patch widths. While $a - Si$ spacer thickness of $368nm$, top metal thickness of $58nm$ and ground plate thickness of $105nm$ is determined. Figure 3.15(a) shows the cross section of antenna stacks with measured dimensions. Moreover, slope of the stack faces $\theta_h : 15^\circ$ and $\theta_m : 76^\circ$ were observed. We learned in previous section that the slope of stack faces tends to decrease an average absorption efficiency of the antenna array. While from equation 2.1 ($\lambda_r = 2Wn_g$) we can say that the mismatch in refractive index between simulated and deposited $a - Si$ is be responsible for the

blue shift in wavelength of peak absorptions, given the increase in patch width for the fabricated antenna arrays.



(a)



(b)

Figure 3.15: (a) Cross section of antenna stack showing the slanted side faces of the stack, (b) Measured and computed absorption of 3CS with more realistic model including slant angles in faces of antenna stack, patch and stack dimension variation and $a - Si$ refractive index error of -5%

With the actual dimensions of the fabricated antenna stack array, and introducing face slopes in the antenna stack, we modeled more realistic antenna array 3CS. We also introduce -5% errors in refractive index of $a - Si$ core. It means, the new value of refractive index of core material is ~ 3.4 instead of 3.6 that we used in previous simulations. Figure 3.15 (b) shows the computed absorption spectra of more realistic antenna array along with ideal antenna array and measured absorption spectra for antenna array 3CS at TM polarization. The calculated absorption spectra for more realistic antenna array is in good agreement with the measured absorption as can be seen in figure 3.15 (b).

We also measured the total reflection from the antenna array 3CS using Bruker A 562-G with integrated sphere (see appendix C for schematic) and used $A = 1 - R$ to find the absorption of an array. Figure 3.16 (a) shows the absorption measured using integrated sphere for antenna array 3CS along with measured absorption with specular reflection and calculated absorption spectra using realistic device model.

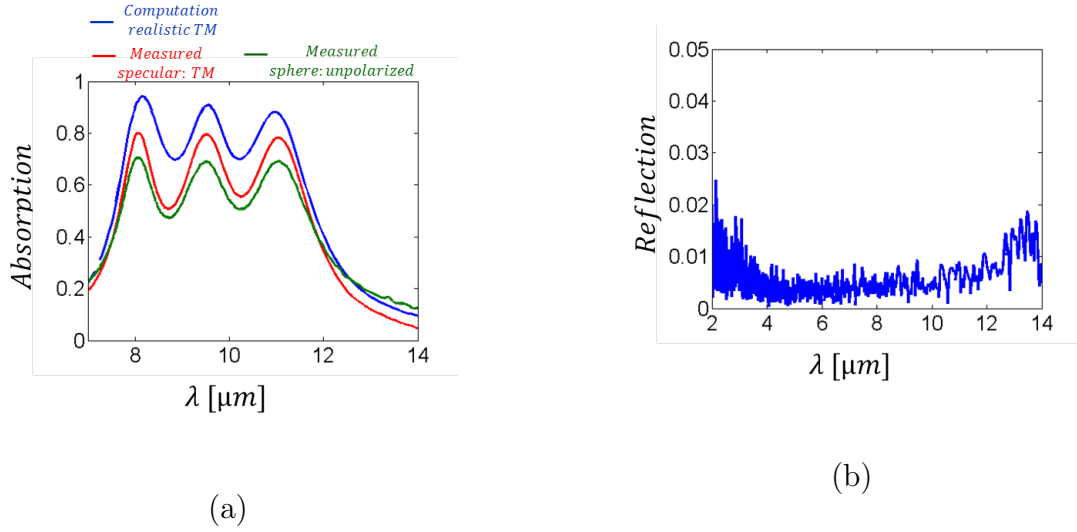


Figure 3.16: (a) Measured, specular and total absorption and computed absorption spectra of 3CS with realistic model, (b) measurement from the antenna array when source is blocked

As can be seen in figure 3.16 (a) the absorption measured using integrated sphere has lower values than that measured using specular reflection from an array. The offset in the absorption as seen in figure 3.16 (a) is unusual. The experiment is repeated again, however each time the measurements showed the similar trend. Absorption calculated by measuring specular reflection is always higher than that calculated by measuring total reflection with integrated sphere. We assume the array is heated during the period of measurement. To check if there is any emission from the array, first we shine the infrared ($2\mu m - 14\mu m$) light to the array without measuring the reflection. After, the source was blocked and the data was collected for $2\mu m - 14\mu m$. Figure 3.16 (b) shows the measurement after the source was blocked. The measured data is normalized to reflection from gold mirror and therefore called reflection in figure 3.16 (b). The measurement in figure 3.16 (b) hardly provide any information on the emission from the array. It could therefore be considered as the noise margin of the detector. It would have been informative if the temperature of antenna array could be measured in real time when reflection measurement is carried out. However in our experiment it was not possible to measure the array temperature in real time.

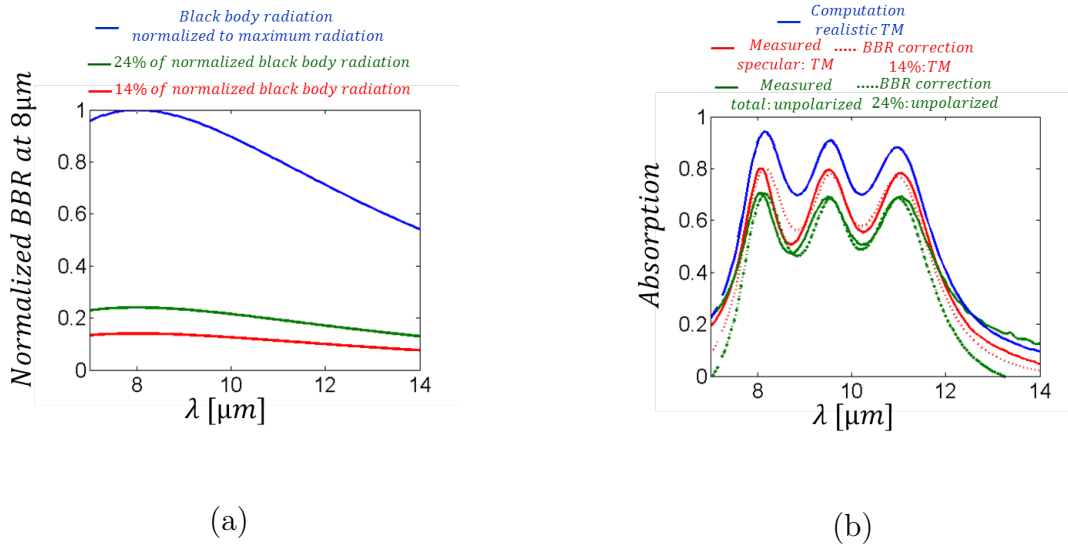


Figure 3.17: (a) Black body radiation (BBR) normalized to maximum radiation at $8\mu\text{m}$. 24% and 14% of normalized black body radiation is also shown. (b) Absorption spectrum fitted assuming black body radiation at $8\mu\text{m}$.

Assuming black body radiation (BBR) at $8\mu\text{m}$ from the array we numerically studied the absorption in antenna array. Figure 3.17 (a) shows the normalized black body radiation at $8\mu\text{m}$ along with 24% and 14% of the radiation. Incorporating, 24% and 14% of the normalized radiation at $8\mu\text{m}$ with the computed absorption spectra using realistic model, we study how absorption would be affected. Figure 3.17 (b) shows the measured (specular and total) absorption and calculated absorption incorporating the black body radiation. Using 24% of BBR the computed absorption fits with absorption calculated by measuring total reflection, while utilizing 14% of BBR the absorption fits with absorption calculated from specular reflection for TM polarized light as can be seen in figure 3.17(b). Even though the calculations could not be validated with experimental methods, we assume the offset in measured absorption could be due to heating of an array.

3.5 Conclusion

In this chapter, we study the effect of dimensional variation of antenna stack array and analyzed the performance of the structure realized at CEA-Leti. We find that it is important to consider the slope and edge roundness of antenna stack to model antenna array more realistically. We find the spectral response of fabricated antenna array is in good agreement with the computed spectral response of realistic antenna model including the correction in slope of stack faces and refractive index of $a - Si$ core. We have experimentally shown that the differently sized antenna array could be used to achieve multi-spectral absorption with efficiency higher than 70%. However, the offset is observed in absorption calculated by measuring specular and total reflection from the antenna array. We assume, the offset is caused due to heating of antenna array which results in thermal emission from the array. The temperature of antenna array could not be measured in real time during the reflection measurement; therefore our assumption of emission could not be validated by experimental methods. However, our numerical study shows that calculated and measured absorption fits when we incorporate black body radiation at $8\mu m$.

Chapter 4

Sorting in Visible

4.1 Introduction

In visible imaging system, three different color filters mainly Red, Green, Blue (RGB) are arranged regularly in Bayer's pattern. The color filters are generally made with pigment based photo-resist [44]. In recent years, there has been various studies in metallic based color filters that could be integrated in CMOS imaging systems [45, 46, 47, 48, 49]. However, as discussed in chapter 1, when the dimension of color pixel approaches the wavelength of light that has to be filtered, the optical performance decreases considerably.

The concept of compact single device to simultaneously generate three primary colors (red, green, blue) from white light has been proposed by Dammann et al in 1978. The compact device proposed by Dammann et al used the phase relief type grating to project primary colors in far field [50]. In other study Knop et al [51] propose binary phase gratings with deep rectangular grooves as transmission filter to project complementary colors, cyan, magenta and yellow in zero diffraction order. Recently, light splitting techniques using microscale plate like structure has been proposed [15]. Further more, photon sorter based on plasmonic structure has also been proposed [52] to increase optical performance of imaging pixels. However,

there exist limitation in the proposed solutions. For example, in the phase relief type grating and binary phase grating proposed in [50, 51], larger grating period has to be used for efficiently project white light to primary color in these structures. Furthermore, the buffer layer between grating structure and detector has to be more than $10\mu m$, resulting in bulky device. Even in the micorscale plate like structure proposed in [15] the buffer layer is atleast $5\mu m$. The microscale plate structure used in [15] has aspect ratio (height of structure/width of structure) larger than 5, resulting in bulky device. In addition the angular tolerance of such devices is very small ($\pm 5^\circ$). The sorting structure base on SPP proposed in [52] requires higher number of gratings covering larger area. Since it is based on SPP, the device is angle sensitive. All of these proposed structures would cease to work with greater efficiency if the pixel size decreases below $1\mu m$. As the pixel size continues to get smaller, different design methodologies has to be explored.

In previous chapters we discussed differently sized metallic patch antenna array to achieve sorting of infrared wave in different spatial location. Using such antenna array, we showed that the near perfect absorption could be achieved for multiple wavelengths. This could have different applications in multispectral and wideband infrared detections. Likewise, the sorting of visible light, mainly of the fundamental color lights red, blue and green could overcome the efficiency limit of traditional color filters used in color detection and imaging systems. In this chapter we will explore different ideas for sorting of visible light.

4.2 Metallic structures for sorting of visible light

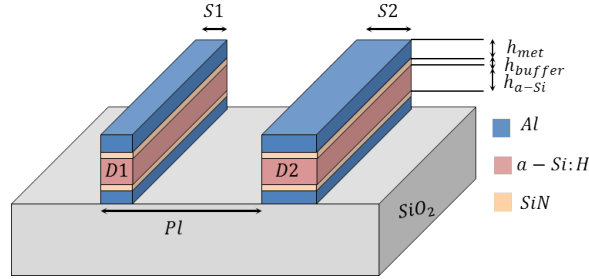
We saw in previous chapters, that the metallic patch antenna can efficiently sort the incidence wavelengths in different spatial locations. In this section, we follow the similar approach to investigate if sorting could be achieved using Metal-Semiconductor-Metal (MSM) nanostructures. Here we test different design of MSM using RCWA method to study the sorting of visible light.

4.2.1 Metal-Semiconductor-Metal Array on transparent substrate

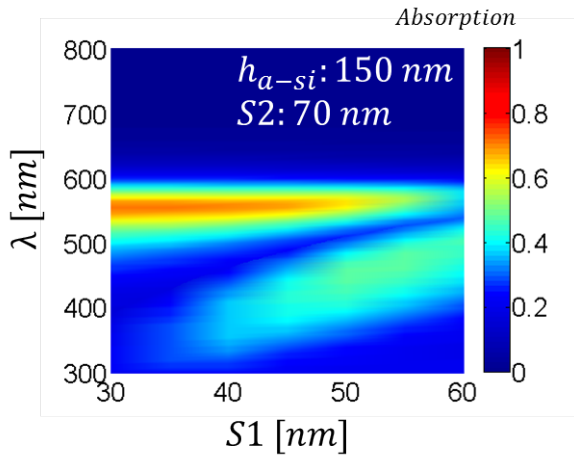
Figure 4.1(a) shows one of the arrangements of differently sized MSM stripes used for the study. The MSM stripes with widths $S1$ and $S2$ are arranged periodically on SiO_2 substrate. We define the distance between edge of one strip to another as local period Pl as shown in figure 4.1 (a). We use amorphous silicon (a-Si:H) as a semiconductor core with Silicon Nitride (SiN) of thickness $h_{buffer} = 10nm$ as a buffer layer between core and Aluminum (Al) strips. The metal thickness of $h_{met} = 40nm$ is considered for the study. In MSM structure, silicon acts both as core and detector simultaneously. For ease we use nomenclature $D1$ and $D2$ for silicon in strip with width $S1$ and $S2$ respectively.

Figure 4.1 (b) shows the absorption in a-Si:H core as a function of wavelength and width $S1$, with $S2$ fixed to $70nm$, core thickness to $h_{(a-Si)} = 150nm$ and local period to $Pl = 150nm$. TM polarized plane wave is considered for the study. The absorption in $D1$ and $D2$ are normalized to the total power incident in unit cell. It can be seen that as the width of stripe $S1$ is increased the wavelength of absorption red shifts ($350nm - 500nm$) following the equation 2.1, while the wavelength of absorption of stripe $S2$ remains constant at $570nm$. It can also be noted that the

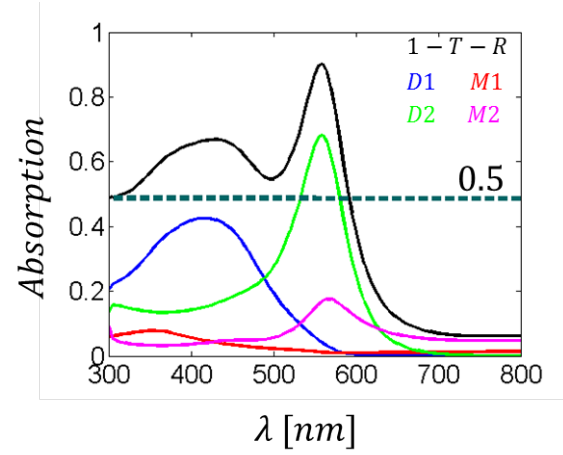
peak absorption in $D1$ is always limited below 50% indicating no sorting for blue light. Meanwhile the absorption in $D2$ is higher than 50% in all the cases.



(a)



(b)



(c)

Figure 4.1: (a) Metal-Semiconductor-Metal array on SiO_2 substrate, (b) Absorption as a function of $S1$ and wavelength for constant $S2$ and $h_{(a-si)} = 150nm$, (c) Absorption of different layer of MSM structure as a function of wavelength for $S1 : 45nm, S2 : 70nm$

Figure 4.1 (c) shows the absorption spectra for the MSM array with $S1 : 45nm, S2 : 70nm$ indicated as $D1$ and $D2$ in blue and green curves respectively. Also shown are the total absorption of the MSM array (black curve) and absorptions in metallic layers of stripe with widths $S1$ and $S2$ indicated as $M1$ and $M2$ respectively.

In chapter 4 we find that tuning core thickness, maximum coupling of incidence light to the core of patch antenna could be achieved. To see if tuning the silicon core

thickness could increase absorption in $D1$ higher than 50%, we varied the silicon thickness from 150nm – 300nm for both stripes in an array.

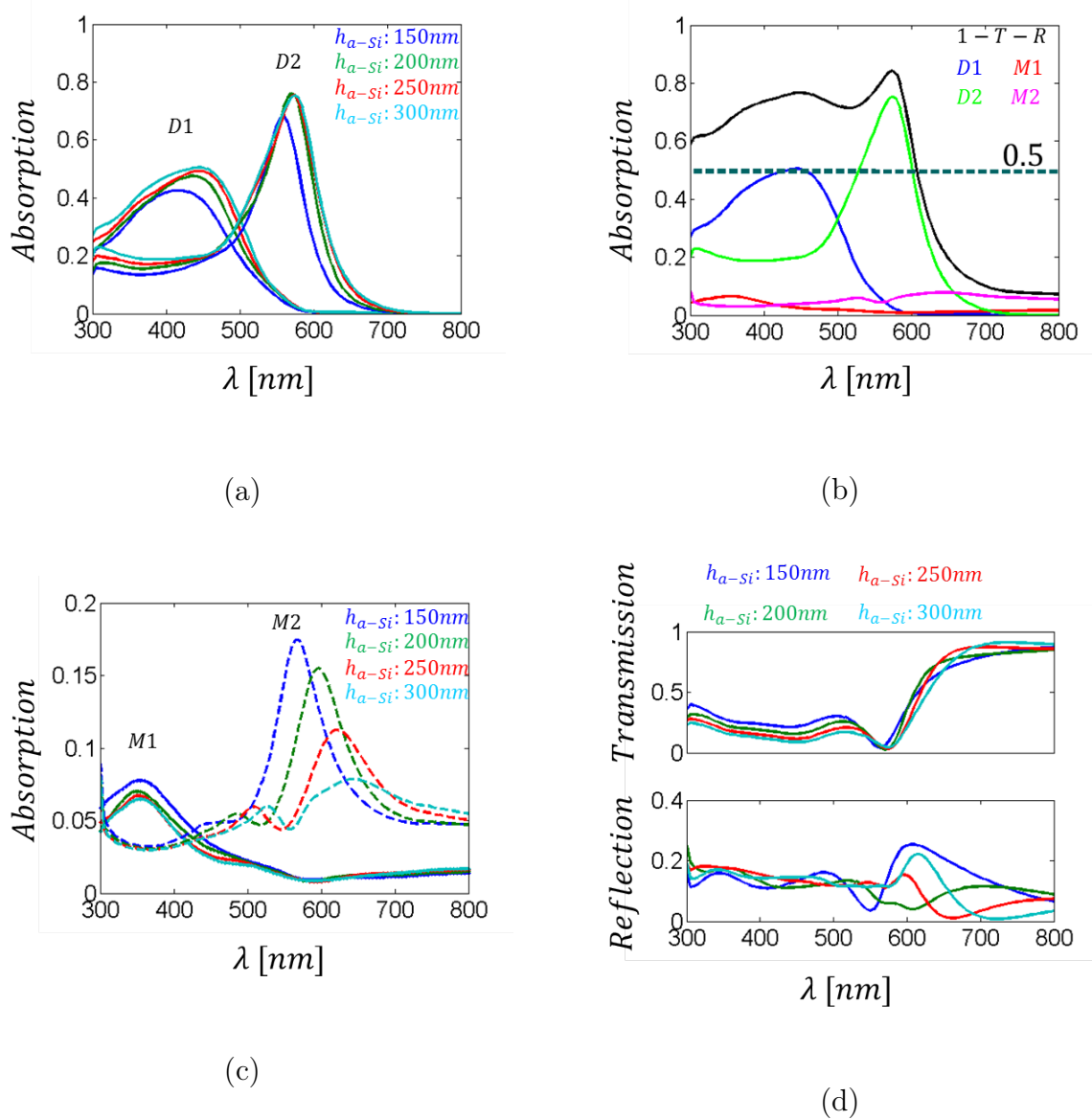


Figure 4.2: (a) Absorption in $D1$ and $D2$ as a function of wavelength for different core thickness, (b) Absorption as a function of wavelength for different MSM layers along with total absorption of MSM array with core thickness of 300nm and $S1 : 45\text{nm}, S2 : 70\text{nm}, h_{met} : 40\text{nm}, h_{buffer} : 10\text{nm}$ and $Pl : 150\text{nm}$, (c) Absorption in metal layers as a function of wavelength for different core thickness, (d) Total transmission and reflection spectrum of MSM array as a function of wavelength for various core thickness

Figure 4.2 (a) shows the absorption as a function of wavelength in $D1$ and $D2$ for different core thickness. It can be seen that the absorption increases as the

core thickness increases. Figure 4.2 (b) shows the absorption spectra for different MSM layers with core thickness of $300nm$ for $S1 : 45nm, S2 : 70nm, h_{met} : 40nm, h_{buffer} : 10nm$ and $Pl : 150nm$. Although, the absorption increases as the core thickness is increased, we find that the peak absorption in $D1$ does not get higher than 50%.

Figure 4.2 (c) shows the total absorption on metallic layer of MSM layers in the array for different core thickness. It can be seen that for strip with width $S2$ which absorbs the green spectrum of incidence wave, the losses in metallic layer decreases rapidly with increase in core thickness. However, for the strip width $S1$, the losses due to absorption in metallic layer changes slowly and fairly remain constant when core thickness is increased higher than $200nm$. Because of its high absorption coefficient, the blue light is mostly absorbed in surface of silicon whereas the green light is absorbed in the bulk [53]. For higher core thickness, most of the light gets absorbed by silicon before it reaches bottom metal layer in MSM stack. It is because of this, for higher core thickness the top metal layer in the stack is responsible for loss arising due to absorption in metal. Therefore decrease in the total metallic loss could be observed for higher core thickness as viewed in figure 4.2 (c).

In addition to metallic losses arising in MSM stack, the transmission loss and reflection loss should also be considered to understand why the peak absorption in $D1$ limits to 50%. In figure 4.2 (d) the transmission and reflection spectra of MSM array for different core thickness is shown. Transmission dip in spectra could be seen around $570nm$ for all core thickness which corresponds to higher absorption of green light in $D2$, however such dip is not seen in blue region. For shorter wavelengths, it could be seen that the transmission loss $\sim 30\%$ and reflection loss $\sim 20\%$ are considerably higher compared to that in green spectra where transmission dip occurs for all the core thickness considered in the study.

From the study of different losses arising in MSM array, we can say that the transmission loss is more responsible to limit the absorption in $D1$ to 50%. While the

metallic loss is inevitable in the stack, we have to find the way to reduce the reflection and transmission loss. At least redirect the transmitted light to array utilizing the reflector so that absorption could be increased in silicon core in MSM array. In next section we will investigate the performance of MSM stack array with the reflector.

4.2.2 Metal-Semiconductor-Metal Array with reflector

In previous section we find that the transmission loss for shorter wavelength limits the absorption in silicon core in MSM stack. The light transmitted into substrate can however be reverted back to array utilizing reflector layer as shown in figure 4.3 (a) where Aluminum layer of thickness $h_{mirror} : 100nm$ is used as a reflecting surface. The separation distance between reflector and MSM array is denoted as h_{cavity} and will be called cavity length hereafter.

Figure 4.3(b) shows the absorption in $D1$ and $D2$ as a function of wavelength and separation distance between reflector and MSM array for $S1 : 45nm, S2 : 70nm, h_{met} : 40nm, h_{buffer} : 10nm, h_{a-si} = 150nm$ and $Pl : 150nm$. It can be seen that for lower value of h_{cavity} the absorption in $D1$ is broad with no distinct absorption peaks. The absorption peak starts to appear for $D1$ as the cavity length increases. The cavity length determines the wavelength of light which is reflected back efficiently following the relation $h_{cavity} = \frac{\lambda}{2n_{cavity}}$, where n_{cavity} and λ are the refractive index of material used as spacer between MSM stack and reflecting surface and wavelength respectively. The red shift in wavelength of peak absorption is visible in figure 4.3 (b) as the cavity length is increased.

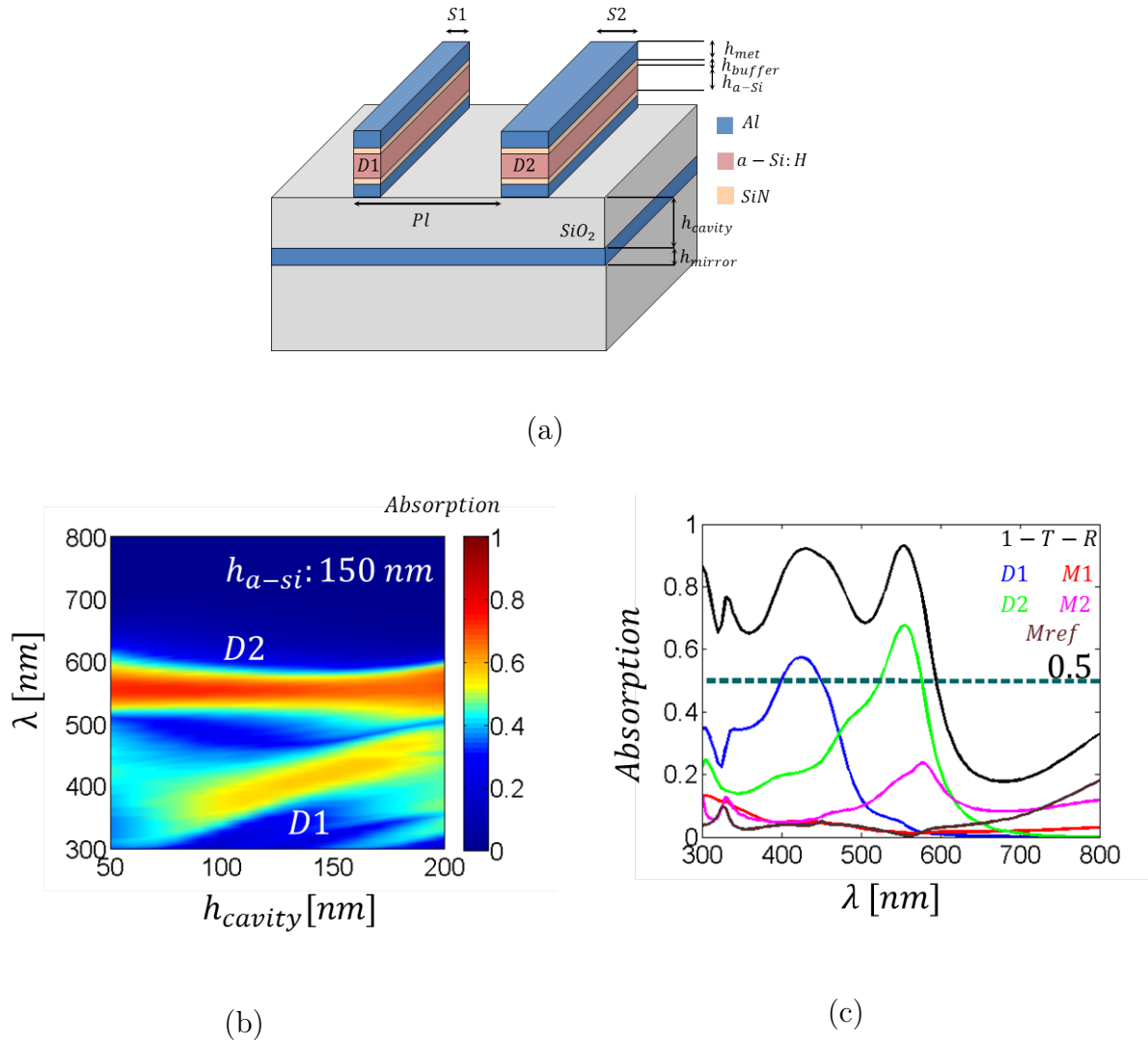


Figure 4.3: (a) MSM stack array with reflector layer, (b) Absorption as a function of wavelength and h_{cavity} for core thickness of 150nm , (c) Absorption of different stack layer and reflector with $h_{cavity} : 150\text{nm}$

For $D2$, it can be seen that the wavelength of peak absorption does not change and peak value retains nearly same value as cavity length is increased. Figure 4.3 (c) shows the absorption as a function of wavelength for different layer of MSM stack along with total absorption of the array for the cavity length of $h_{cavity} : 150\text{nm}$. Also shown is the absorption loss associated with aluminum thin film used as reflector which is denoted as $Mref$ in figure 4.3(c). For appropriate cavity length, it can be seen that the absorption of blue spectra could be increased ($> 50\%$) in $D1$.

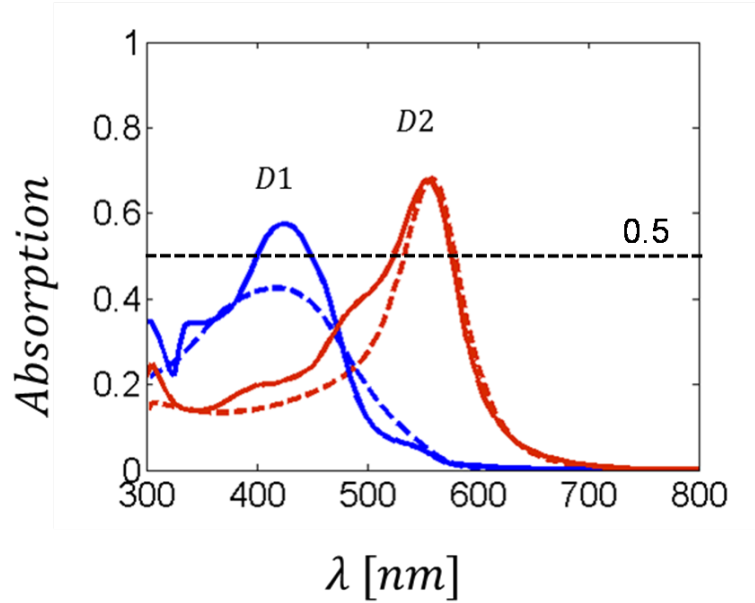


Figure 4.4: Comparison of absorption in silicon layer in MSM array with and without reflector

In figure 4.4, the absorption in silicon cores, $D1$ and $D2$ of MSM stack array with widths $S1 : 45nm$ and $S2 : 70nm$ respectively is shown for array with and without utilizing reflector layer. The solid lines represent the absorption in core material of MSM array utilizing reflector layer. While the broken line represents the absorption of MSM array, discussed in previous section, without using any reflector layer. The core thickness of $h_{a-si} = 150nm$ is considered for both structures in comparison, while the cavity length of $h_{cavity} : 150nm$ was considered for structure utilizing reflector. It can be seen that using reflector layer, the peak absorption in $D1$ could be increased significantly. For this particular comparison, the peak absorption in $D1$ is increased by factor of 1.4 when reflector layer is used. It can also be noted that the absorption spectrum in $D2$ gets wider, while change in peak absorption value is almost negligible for the structure utilizing reflector layer.

We find that using reflecting layer the absorption in MSM core could be increased, however with additional metallic layer, we also increase the loss associated with absorption in the metal. Figure 4.5(a) shows the absorption in metal layers in MSM

stack array with reflector as a function of wavelength for different cavity lengths. $M1$, $M2$ indicates the total metallic losses associated to MSM stripes with width $S1 : 45nm$ and $S2 : 70nm$ respectively. Whereas M_{res} represent the metallic absorption in reflecting layer.

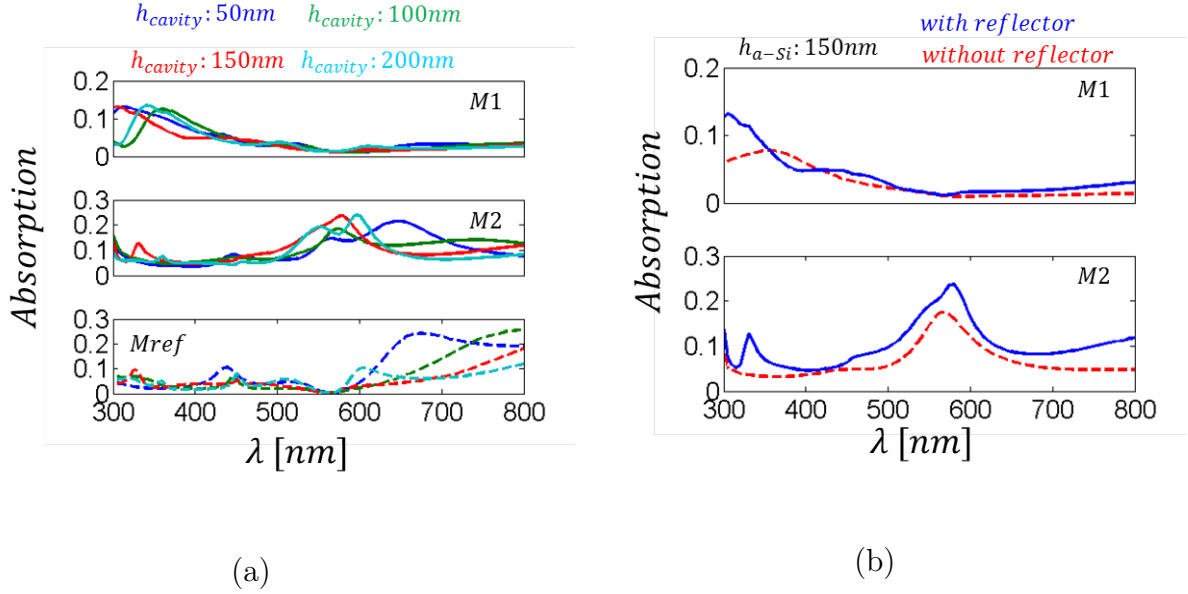


Figure 4.5: (a) Absorption in metal layers as a function of wavelength for different cavity lengths, (b) Comparison of absorption in metal layers of MSM array with and without reflecting surface. The dimensions considered for MSM array are: $S1 : 45nm, S2 : 70nm, h_{met} : 40nm, h_{buffer} : 10nm, h_{a-si} = 150nm$ and $Pl : 150nm$

It can be seen that the absorption in reflector is dominant in longer wavelengths ($> 600nm$). However, a glitch in the absorption curve around $\sim 450nm$ could be observed, which corresponds to $\sim 8\%$ of total incident power for cavity length of $150nm$. Figure 4.5(b) shows the comparison of absorption in metallic layer of MSM stack with and without using reflector layer. It can be seen that the absorption increases significantly for MSM stack with width $S2$, while that for stack with width $S1$ the increment is significant only around $\sim 300nm - 350nm$. Whether we use reflector layer or not, the absorption in metal used in different layer of MSM stack to sort visible light is inevitable.

Even though the structures we presented for sorting visible light to efficiently detect fundamental colors are conceptually simple, the requirement of smaller dimensions and high aspect ratio of MSM stack might be for the moment technologically challenging. Furthermore, the detection of red light would be more challenging as a-Si:H has lower absorption coefficient in this spectra. This means thicker cores in MSM stack is required, which in turns only increases the aspect ratio of the stack. Metallic losses along with problem of charge extraction from detector, surface recombination of charge generated in silicon to metallic layer and other associated technological challenge thus limit the performance of spectral sorter discussed here.

It is therefore, necessary to investigate different design methodology without using metallic layers, to efficiently sort the visible light. In next sections, we will investigate the reflection property of silicon and study how simple two layer or multi-layer anti reflection structures could be utilized to achieve sorting of visible light.

4.3 Dielectric based structure for sorting of visible light

In this section we will investigate the dielectric based sorting structure for visible light. Using TMM we will study the antireflection behavior of simple one and two layer coating structure. We will use the information from reflection analysis to study the absorption efficiency of silicon when two antireflection structures are deposited periodically on top of silicon. Later we will apply effective medium theory of lamellar grating to the one of the coating layer to design grating based antireflection structure. With grating based antireflection structure we then investigate the sorting of visible light.

4.3.1 Antireflection property of multilayer dielectric on Silicon

Silicon is widely used as the photo detecting material in visible imaging system [10, 1, 54]. The color filters are generally used to separate white light into fundamental colors, red, green and blue colors. As discussed in previous chapters, the optical efficiency of filters deteriorates as the pixel size decreases. Furthermore as the pixel sizes in image sensor continues to shrink, more technological challenge to maintain higher optical efficiency, quantum efficiency of detector and the signal-to-noise arises [54]. It is therefore necessary to find the alternative approaches to deal with such issues. In this section and next sections, we try to address and exploit the antireflection property of dielectric coatings on silicon which could be important to design sub-micron detectors with high optical efficiency and signal-to-noise ratio.

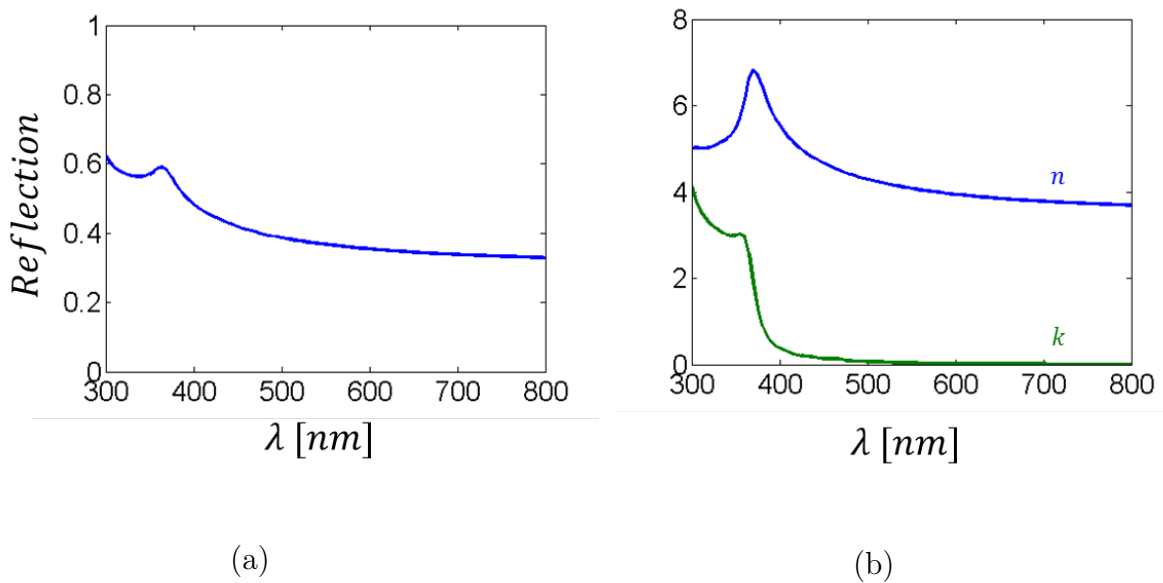
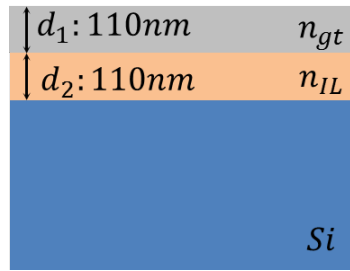


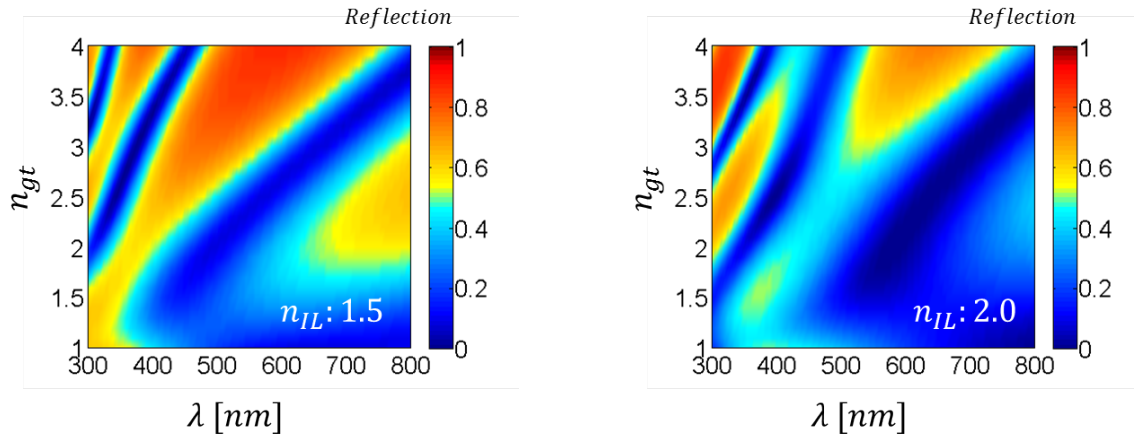
Figure 4.6: (a) Reflection as a function of wavelength of bulk silicon, (b) Real and imaginary part of refractive index of silicon as a function of wavelength

Because of its high refractive index, reflection of visible light from bulk silicon is considerably high as shown in figure 4.6(a). The index of refraction of silicon is generally complex in visible spectrum. The values of real and imaginary part of this

complex index depends on wavelength and is shown in figure 4.6(b) represented as n and k respectively. It can be seen that the reflection is flat in entire visible spectrum. However, the absorbed light is considerably wide band but not flat [53] because of its low absorption coefficient ($\alpha = \frac{4\pi k}{\lambda}$) at longer wavelengths. Using dielectric layers on top of bulk silicon, selective antireflection or in other words selective absorption of specific wavelengths could be achieved. One such system using two layers of dielectric material is shown in figure 4.7(a). In this study we will consider dielectric materials which are transparent at visible wavelengths. For simplicity first we will use constant value of refractive index without imaginary part for all the wavelengths in visible domain.



(a)



(b)

(c)

Figure 4.7: (a) Two layer dielectric structure on top of Silicon, with individual thickness of $110nm$, Reflection as a function of wavelengths and refractive index of top layer (n_{gt}) with index of second layer (b) $n_{IL} = 1.5$ and (c) $n_{IL} = 2.0$

We learned in previous section, that the reflection from the multi-layer system depends on refractive indices and thickness of dielectric layers used. We consider the thickness of both, first layer (d_1) and second dielectric layer (d_2) to have same values of $110nm$. The refractive index of first- and second- layer are denoted as n_{gt} and n_{IL} respectively. With the thickness fixed to specific values, we can vary the refractive index of dielectric layers to tune the wavelength at which anti-reflection occurs.

In figure 4.7 (b) and (c) the reflection as a function of wavelength and refractive index of first layer n_{gt} is shown when the index of second dielectric layer is kept constant at $n_{IL} : 1.5$ and $n_{IL} : 2.0$ respectively. When the refractive index of first layer is varied from $n_{gt} : 1.0$ to $n_{gt} : 4.0$ the reflection minima could be observed for the wavelengths satisfying anti-reflection condition. With increase in refractive index of first layer, the optical path length increases. This shifts the reflection minima toward longer wavelengths as visible in figure 4.7(b) and (c).

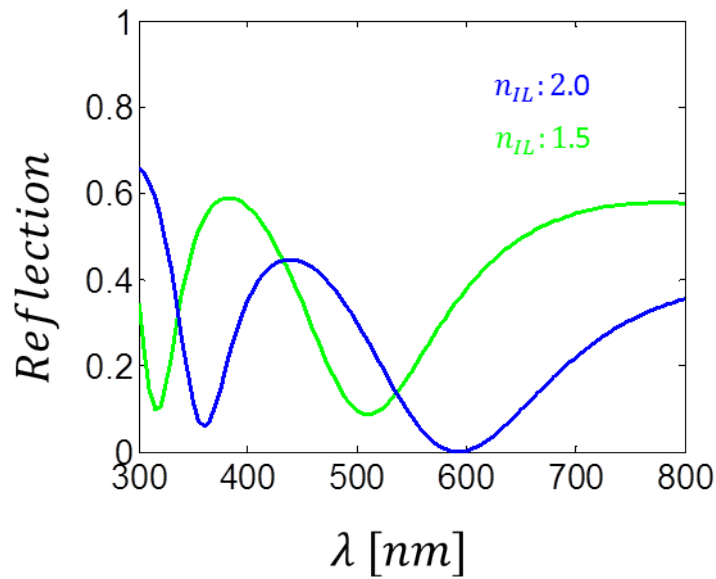


Figure 4.8: Reflection of two layer system with index of first layer $n_{gt}2.1$ and different indices for second layer

Figure 4.8 shows the reflection as a function of wavelength for a two layer system with $n_{gt} : 2.1$. Two reflection minima could be seen for both systems with $n_{IL} : 1.5$

and $n_{IL} : 2.0$. The reflection dip at longer wavelength corresponds to primary anti-reflection, while the reflection dip at shorter wavelengths are first order anti-reflection.

We see that using two layers system and appropriately choosing the refractive indices and thickness of dielectric material we could tune the wavelengths at which antireflection occurs. However, in this study we focus that the layered system designed to anti reflect two or more different wavelengths should have same material in the first layer and same thickness for both first and second dielectric layers.

With these criteria, we can then arrange different layered structure on top of silicon in periodic manner. The unit cell of such arrangement is shown in figure 4.9(a), where the top layer for both systems has same material with refractive index defined as n_{gt} and same thickness d_1 . The second layer for these systems has different materials with refractive index denoted by n_{IL-1} and n_{IL-2} but same thickness d_2 . For this study, the layer structures which have reflection spectra shown in figure 4.8 and discussed previously are considered. The size of the layered structure arranged periodically were considered to have same sizes defined as Px which is visible in figure 4.9(a). We define the silicon below the layer structure with indices n_{gt} and n_{IL-1} as $Dt1$ and that below the layer structure with indices n_{gt} and n_{IL-2} as $Dt2$ for convenience.

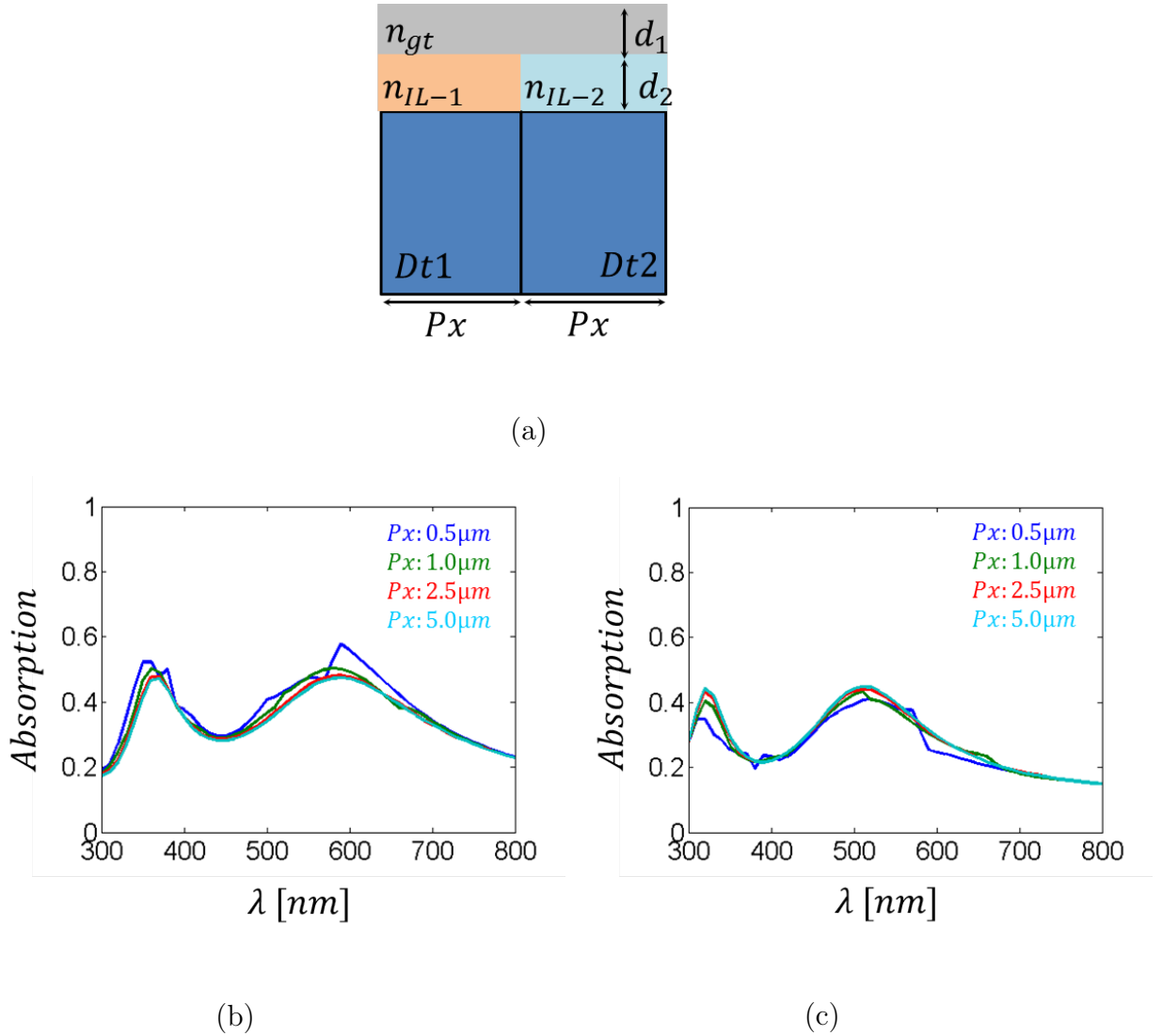


Figure 4.9: (a) Unit cell of the periodic arrangement of layered structures designed to minimize reflection at different wavelengths. Absorption spectra of silicon under the layered system with first- and second-layer made of material with indices (b) $n_{gt}2.1$ and $n_{IL-1} : 2.0$, (c) $n_{gt} : 2.1$ and $n_{IL-2} : 1.5$ for different sizes (Px) of the structure.

In such arrangement, the absorption in silicon could then be calculated for each layer structures normalized to total incidence power in a unit cell. The absorption in $Dt1$ and $Dt2$ with $n_{gt}2.1$, $n_{IL-1} : 2.0$ and $n_{IL-2} : 1.5$ is shown in figure 4.9(b) and (c) respectively for different values of Px . The thickness of both, first dielectric layer (d_1) and second dielectric layer (d_2) were considered to have same values of $110nm$ for the calculation. It can be seen that the normalized absorption in each

silicon detectors $Dt1$ and $Dt2$ remains almost unchanged when its size is decreased down to $0.5\mu m$. More over the absorption is relatively broadband, the maximum value of which is never above 50% of total incidence power.

Using many different layers of different dielectric materials, the spectra could be made narrow band, however the normalized absorption would not be higher than 50%. We conclude here that using antireflection structure with homogenous layers only, the sorting of visible light could not be achieved even for sub-micron sized structures. However, we could exploit the effective medium theory of lamellar grating to replace the first homogenous layer in the structure with dielectric gratings. We will study in next sections how the grating structures could be in-cooperated to the antireflecting structures and simultaneously facilitate the sorting of visible light.

4.3.2 Grating based anti-reflection structure

Subwavelength gratings have been widely studied for the application in antireflective surface, polarization elements and homogenous birefringent materials [55, 56, 57, 58] using effective medium theory. In effective medium theory (EMT) the subwavelength grating with period smaller than half wavelength of incidence wave are treated as homogenous medium as shown in figure 4.10(a).

As shown in figure 4.10(a) the grating with subwavelength period P , and grating width W can be represented as a homogenous layer with effective refractive index n_{eff} . The effective refractive index of such grating can be estimated for TE polarization using second order EMT [59] as:

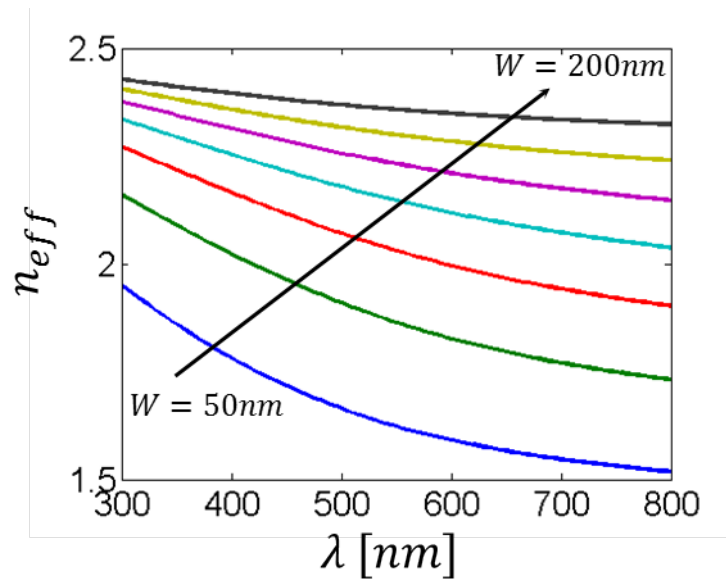
$$n_{eff}^{(2)} = \left[\left(n_{TE}^{(0)} \right)^2 + \frac{1}{3} \left(\frac{P}{\lambda} \right)^2 \pi^2 f^2 (1-f)^2 (n_g^2 - n_0^2) \right]^{1/2} \quad (4.1)$$

$$n_{TE}^{(0)} = [(1-f)n_0^2 + fn_g^2]^{1/2} \quad (4.2)$$

Where, $f = \frac{W}{P}$, n_0 and n_g are the filling factor of grating, refractive index of grating groove and grating material respectively.



(a)



(b)

Figure 4.10: (a) Homogenization of grating with subwavelength period. The effective index of homogenous layer is calculated using effective medium theory. (b) Effective index as a function of wavelength for different grating widths with grating refractive index of 2.5 and period 250nm

Figure 4.10(b) shows the effective index as a function of wavelength when the grating width W is varied from 50nm – 200nm in step of 25nm for grating with period 250nm and grating material with refractive index 2.5. The refractive index of grating groove is considered to be 1.0 for the calculation. It can be seen that the effective index could be changed just by changing the width of the grating. Also, for the known refractive index of homogenous layer, corresponding grating parameters could therefore be

calculated using effective medium theory. In this section we will apply the effective medium theory to the first dielectric layer used in multi layered antireflection system.

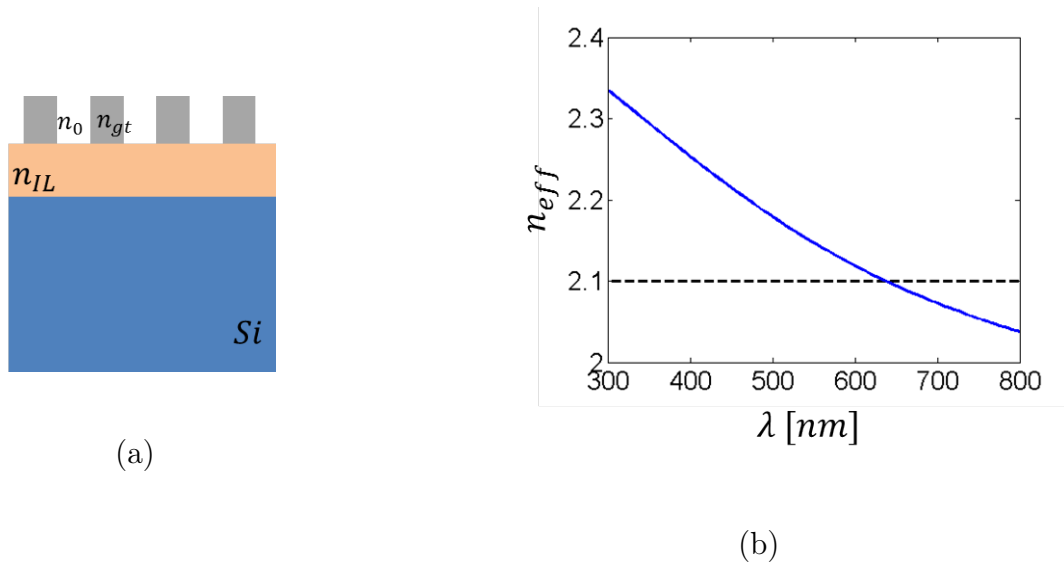


Figure 4.11: (a) Two layer system with grating as first layer, (b) effective refractive index of the grating layer calculated using effective medium theory.

For the two layers anti reflection system described in previous section, we replace the first dielectric layer with a grating structure as shown in figure 4.11 (a). The grating material and grating groove with refractive index 2.5 and 1.0 respectively are considered for the study. The grating height and thickness of homogenous second layer is both kept constant to $110nm$ as described in previous section, while the grating period of $250nm$ and grating width of $125nm$ is considered.

Figure 4.11(b) shows the effective index of the grating calculated using effective medium theory. It can be seen that the index is higher for shorter wavelengths compared to homogenous layer with refractive index 2.1 that was considered in previous section. While for longer wavelengths the effective index of the grating is comparable to that of homogenous layer. This means the wavelength of antireflection at shorter wavelength red shifts for the structure with grating compared to layered structure with homogenous first layer. Also the grating period considered in this analysis is comparable to the half wavelength of blue and green light. The grating

could therefore induce the reflection anomaly which could change the reflection minima of the system.

Figure 4.12 (a) and (b) shows the reflection spectra of the two layer system with grating on first layer and homogenous second layer with refractive indices 1.5 and 2.0 deposited on top of silicon respectively. The reflection spectrum is calculated using two different methods. First we use the TMM method, in which the grating layer is represented as the homogenous layer whose refractive index is calculated using effective medium theory. And secondly, we use RCWA method to study the effect of grating period on the reflection spectra at shorter wavelengths. For comparison the reflection spectra for the two layer system with homogenous first layer is also shown.

It can be seen that the reflection dip at shorter wavelengths red shifts when the grating is represented as homogenous layer with its calculated effective index, while that does not change for longer wavelengths. When the structure is studied more rigorously using RCWA method it can be seen that the reflection dip at longer wavelengths does not vary significantly, while at shorter wavelengths it red shifts significantly as can be viewed in figure 4.12 (a) and (b). It is interesting to see that the two reflection dips arises at $355nm$ and $420nm$ for the structure with grating first layer and homogenous second layer with refractive index 2.0.

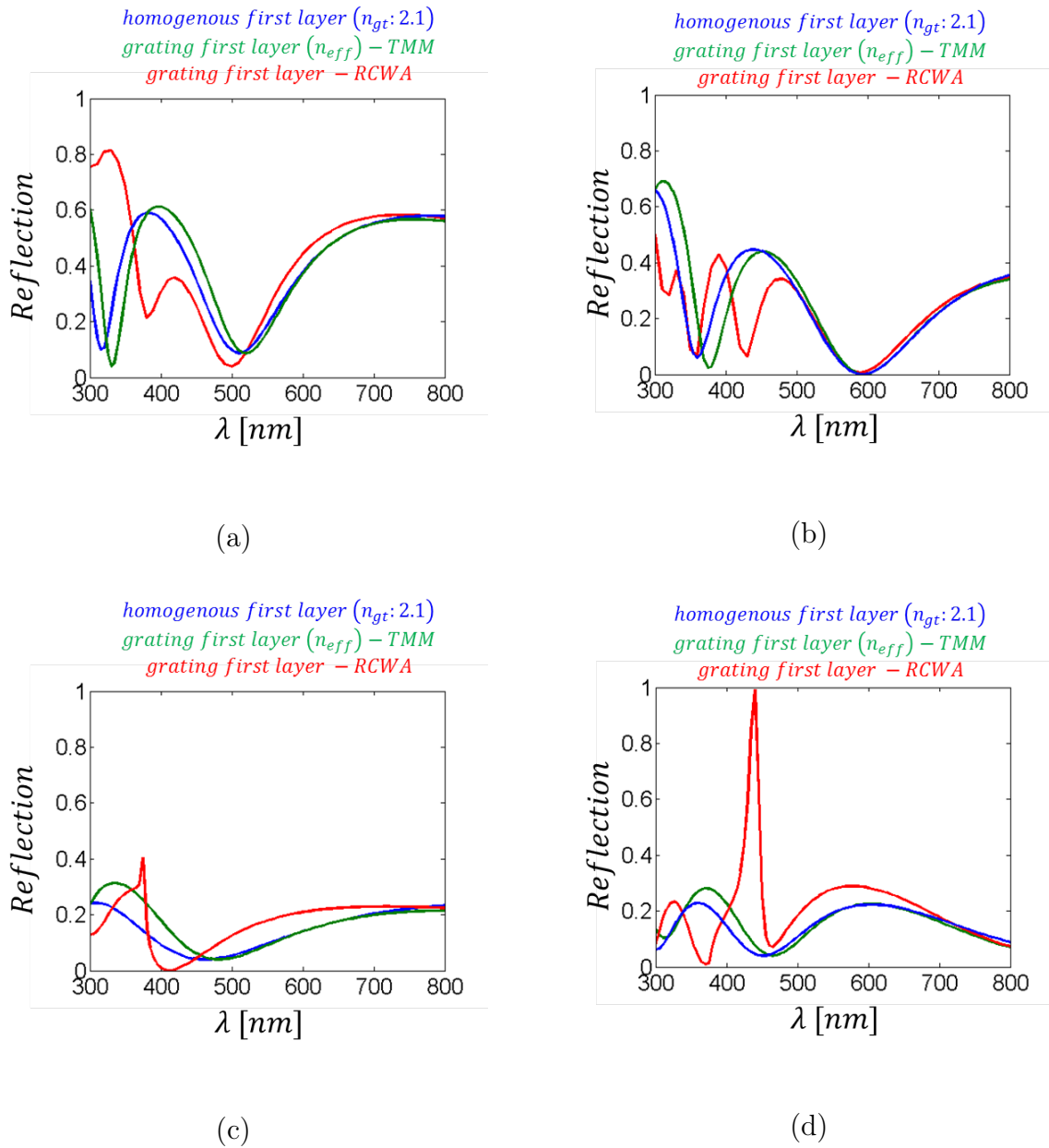


Figure 4.12: Comparison of reflection spectra for two layer system with homogenous first layer and grating first layer calculated using TMM model and RCWA method with homogenous second layer (a) $n_{IL} = 1.5$ and (b) $n_{IL} = 2.0$ deposited on silicon, (c) $n_{IL} = 1.5$ and (d) $n_{IL} = 2.0$ deposited on homogenous material with refractive index 1.5

The reflection dip at 355nm matches that to the reflection dip corresponding to two layer system with homogenous layers with refractive index 2.1 and 2.0 as first and second layer respectively. We assume the red shift of reflection dip and the reflection dip at 420nm arises because of the reflection anomaly due to the grating.

To check if this is the case, we replace the silicon substrate in our two layer system with homogenous material with constant refractive index 1.5 and calculated the reflection spectra of the new system. Since the new substrate has refractive index lower than the silicon, we expect the reflection maxima at the wavelengths where we observed reflection minima with silicon substrate.

The reflection spectra for new two layer system with grating on first layer and homogenous second layer with refractive indices 1.5 and 2.0 is shown in figure 4.12 (c) and (d) respectively. For the reference, the reflection spectra of two layer systems with homogenous first layer are also shown (blue and green curves). The spectrum in blue represents the reflection of layered structure with homogenous first layer of refractive index 2.1, while that in green represents the reflection of layered structure in which EMT is applied to the grating.

Applying EMT to the grating, the reflection anomaly could not be observed. However, using more rigorous method (RCWA) for electromagnetic simulation such anomaly could be calculated for the layered system with gratings. An abrupt change in reflection could be observed at the wavelength of $420nm$, for the layered system with grating first layer and homogenous second layer with refractive index 2.0 as visible in figure 4.12 (d). Such anomaly in reflection occurs when the guide mode is excited on the structure [60, 61, 62, 63]. Similarly, the discontinuity in reflection spectra at the wavelength of $375nm$ could be observed for the system with grating first layer and homogenous second layer with refractive index 1.5 as visible in figure 4.12 (c). However, the strength of discrepancy in reflection spectra is relatively small. Comparing the reflection spectra of two layer system with grating first layer and different substrates, we can see that the reflection maxima corresponding to reflection anomaly of the system with low index substrate ($n_s = 1.5$) coincide with reflection minima at $375nm$ and $420nm$ of system with silicon substrate. We can therefore say that the reflection dip at $375nm$ and $420nm$ for the system with silicon substrate arises because of reflection anomaly due to the grating.

In this section, we see that the sub wavelength grating could be incorporated in antireflection structure. We find that, for longer wavelength, the grating could be modeled as a homogenous layer. However more rigorous analysis should be considered to predict the reflection minima at shorter wavelengths as the grating period is comparable to the wavelength in this domain. In next section we will investigate how these antireflection structure with grating could be utilized to achieve sorting of visible light.

4.3.3 Grating assisted sorting of visible light

In section 6.2.2, we combined two different multi-layered structures periodically and study the absorption in silicon. We follow the similar approach in this section to study the absorption in silicon when two grating based antireflection structures are arranged periodically. The grating based antireflection structures discussed in previous section can be arranged in two different configurations, the unit cell of which are as shown in figure 4.13 (a) and (b). For ease, we will name the configuration shown in figure 4.13 (a) and (b) as $C1$ and $C2$ respectively. The size of the individual structures is chosen such that each structure contains atleast one grating stub or a groove. This means the individual sizes are multiple of grating period $Px = qP_g$, where $q = 1, 2, \dots$ and $P_g = 250nm$ is the grating period. It can be seen that the configuration $C2$ is the complimentary of configuration $C1$ and has one grating stub in the junction of homogenous second layer. In the figure, the homogenous second layer with refractive index 1.5 and 2.0 are denoted as n_{IL-1} and n_{IL-2} respectively and both has thickness of $110nm$. The silicon under n_{IL-1} and n_{IL-2} are used as to detect the light and are denoted as $Dt1$ and $Dt2$ respectively.

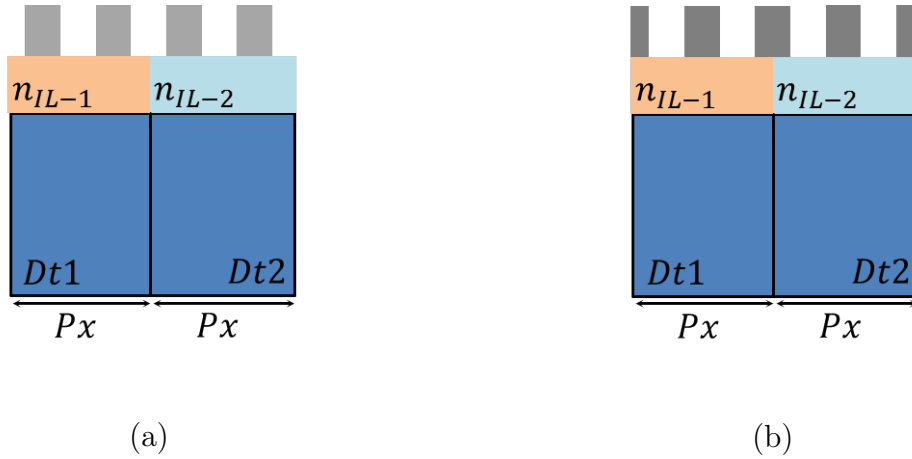


Figure 4.13: Different configuration of grating based antireflection structures (a) with grating stub on top of second layer of each antireflection structure (b) with atleast one grating stub on top of second layer of each structure and one on top of junction of second layer

We calculate the absorption in $Dt1$ and $Dt2$ normalized to the total incidence power in a unit cell for each configurations $C1$ and $C2$. Figure-4.14 (a) and (b) shows the absorption in $Dt1$ and $Dt2$ respectively for the configuration $C1$ when the size (Px) of individual detectors or structures is varied from $5\mu m$ down to $0.5\mu m$. The dotted line indicates the $NOE = 0.5$ which is the classical limit of absorption in each detectors $Dt1$ and $Dt2$. In chapter 4, we discussed that the sorting of light is the phenomenon when the absorption in each detector is higher than 0.5 when it is normalized to total incident power in the unit cell. It can be seen that the absorption in $Dt1$ is below 0.5 even when the size is decreases down to $0.5\mu m$. While the absorption in $Dt2$ is higher than 0.5 at $420nm$ for detector size as large as $2.5\mu m$. The absorption efficiency at $560nm$ in $Dt2$ remains near 0.5 even the size is increase from $0.5\mu m$ to $5\mu m$. It is visible form figure 4.14 that using configuration $C1$, only the blue light could be detected with higher efficiency, meaning we could only sort the blue light while no sorting could be achieved for green light.

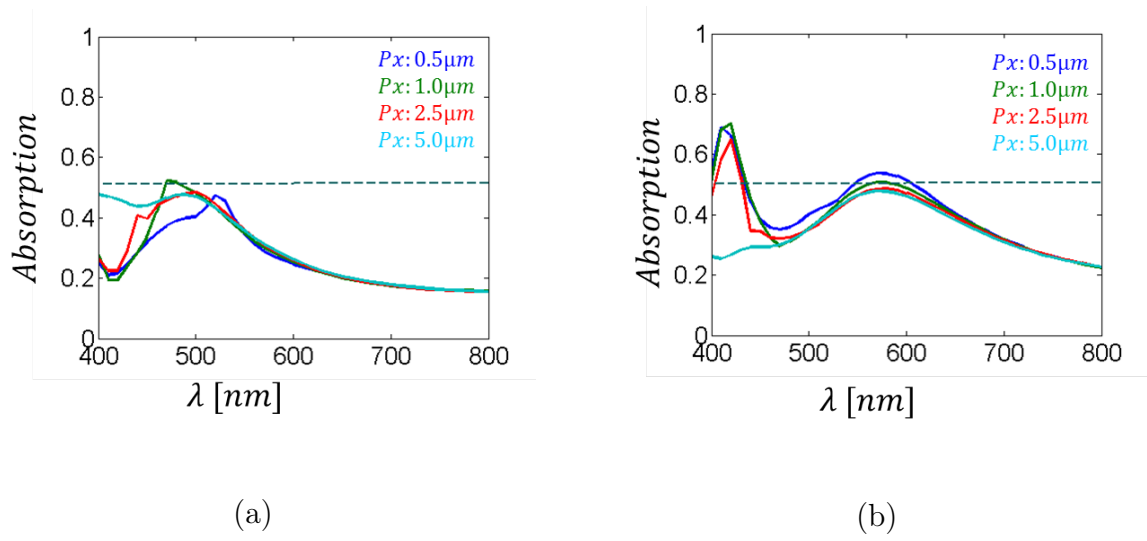


Figure 4.14: Absorption as a function of wavelength for different structure sizes ($Px : 0.5\mu m - 5\mu m$) in the silicon under (a) $n_{IL-1} : 1.5$ and (b) $n_{IL-2} : 2.0$ for configuration $C1$

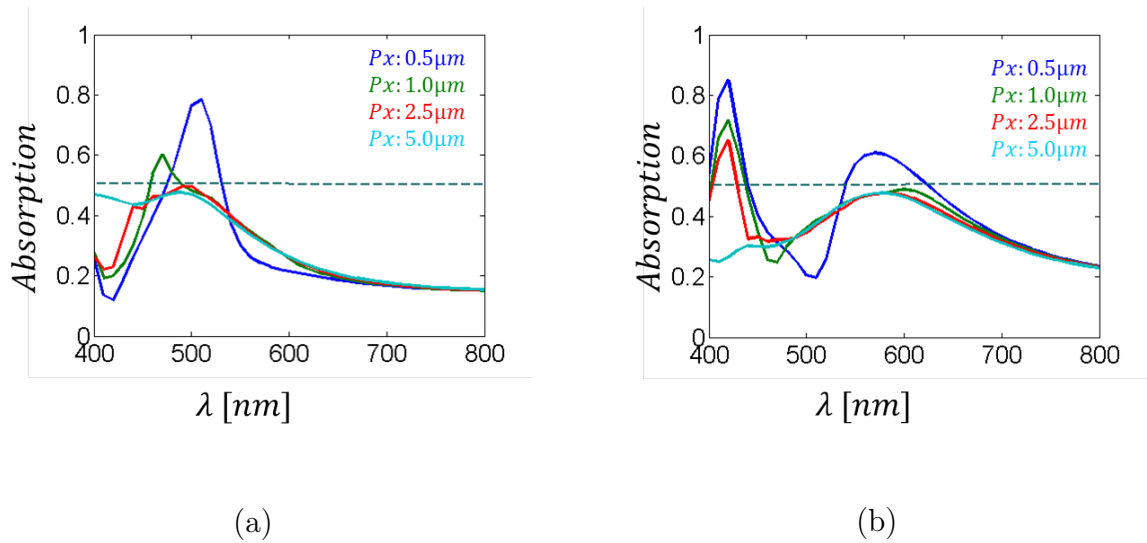


Figure 4.15: Absorption as a function of wavelength for different structure sizes ($Px : 0.5\mu m - 5\mu m$) in the silicon under (a) $n_{IL-1} : 1.5$ and (b) $n_{IL-2} : 2.0$ for configuration $C2$

Similarly, figure 4.15 (a) and (b) shows the absorption in $Dt1$ and $Dt2$ respectively for the configuration $C2$ when the size (Px) of individual detectors is varied from $5\mu m$ to $0.5\mu m$. It can be seen that the absorption of green light ($520nm$) in $Dt1$ remains lower than 0.5 for detector size as small as $1.0\mu m$, however the absorption

gets higher than 0.5 when detector size is decreased down to $0.5\mu m$. For this size, the absorption efficiency is as high as 0.8 as can be viewed in figure 4.15 (a). The absorption of blue light ($420nm$) in $Dt1$ for configuration $C2$ is much higher compared to that of configuration $C1$. It can be seen in figure 4.15 (b), the absorption at $420nm$ is higher than 0.8 for the detector size of $0.5\mu m$, while it remains higher than 0.5 for the detector size as large as $2.5\mu m$. Moreover, the absorption in red also increases when detector size is decreased to $0.5\mu m$ as can be viewed in figure 4.15 (b).

From figure 4.14 and figure 4.15, we learned that the sorting of visible light with higher absorption efficiency is possible for submicron detector size using configuration $C2$ which has atleast one grating stub on top of second layer of each structure and one on top of junction of second layer. We assume the grating stub on top of the junction of homogenous second layer has a key role for sorting which results in high absorption efficiency at wavelength of $520nm$ and $420nm$.

Figure-4.16 (a) and (b) shows the electromagnetic power dissipation in the silicon at $520nm$ and $420nm$ respectively for the configuration $C2$ calculated using COMSOL RF module. It also shows the power flow time average in the unit cell. The detector size of $0.5\mu m$ is used for the calculation. It can be seen from figure 4.16 (a) that the grating stub on top of the junction of homogenous second layer directs the portion of incidence power at adjacent structure to silicon under n_{IL-1} at the wavelength of peak absorption of $Dt1(\lambda : 520nm)$. Similarly, at $420nm$, the grating stub on top of junction directs the portion of power incident at adjacent structure to silicon ($Dt2$) under n_{IL-2} as can be viewed from figure 4.16 (b). This can be viewed as an increase in absorption cross section area of silicon detectors $Dt1$ and $Dt2$ facilitated by grating stub on top of the junction of second layer.

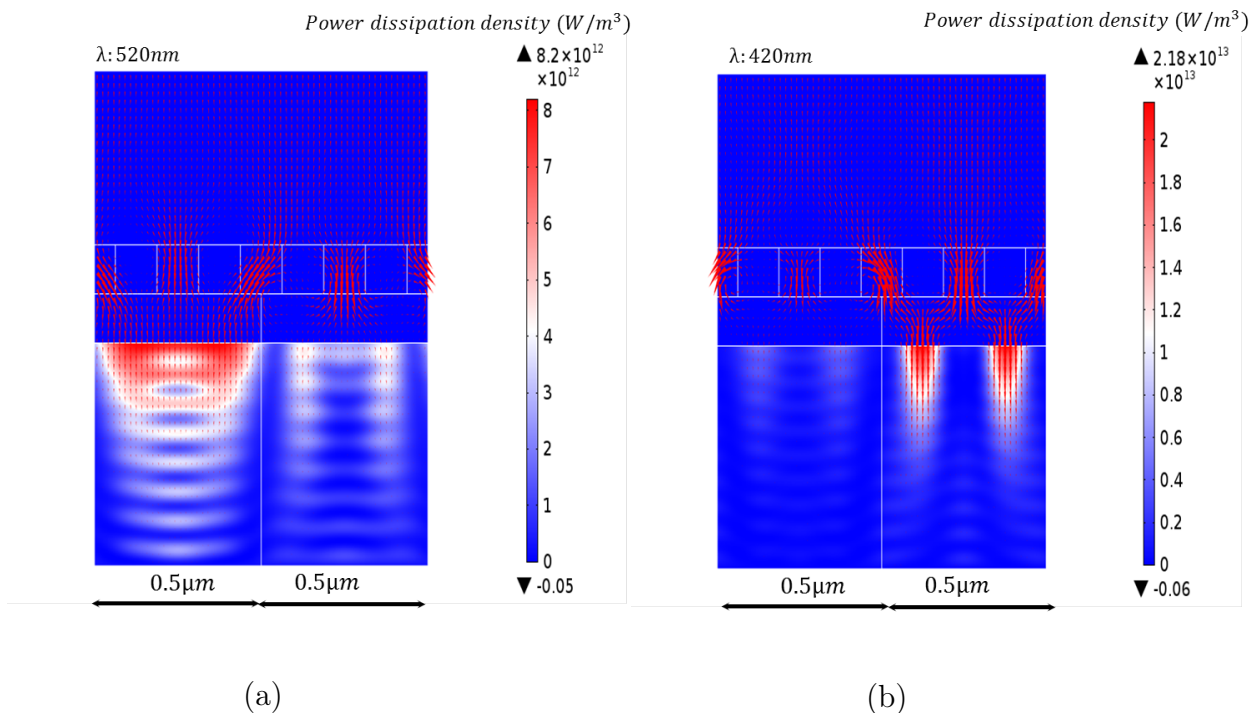


Figure 4.16: Electromagnetic power dissipation in silicon as a function of spatial position for configuration *C2* at wavelength of (a) $520nm$ and (b) $420nm$. The red arrows indicates the power flow time average in the structure

We see from figure 4.15 and figure 4.16, that using simple two layer structure, we could achieve higher absorption efficiency for the detector size as small as $0.5\mu m$. We also find that for larger detector size, grating based layered system simply acts as antireflection structure with maximum absorption limited to 50% of the total power incident on the unit cell. Therefore, we conclude that these layered systems are most efficient when the detector size is less than $1\mu m$. Such layered system can moreover be utilized to design the submicron color pixels which are difficult to achieve using conventional color filter technology. We can use the following simple steps to design submicron sized color detectors with high optical efficiency:

1. Design multilayer antireflection coating for Blue and Green or Green and Red colors.

Constraints:

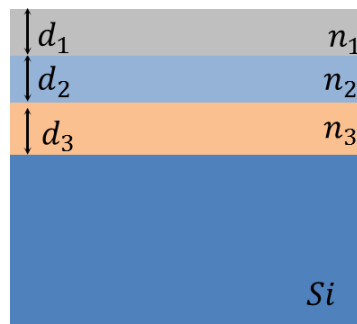
- (a) Same thickness for each layers
 - (b) Same material for top layer
2. Apply effective medium theory to translate top homogenous layer to grating structure. Such grating has same period and grating width for both antireflecting structures (Blue and Green or Green and Red).
 3. Periodically arrange antireflecting structure.

Constraint:

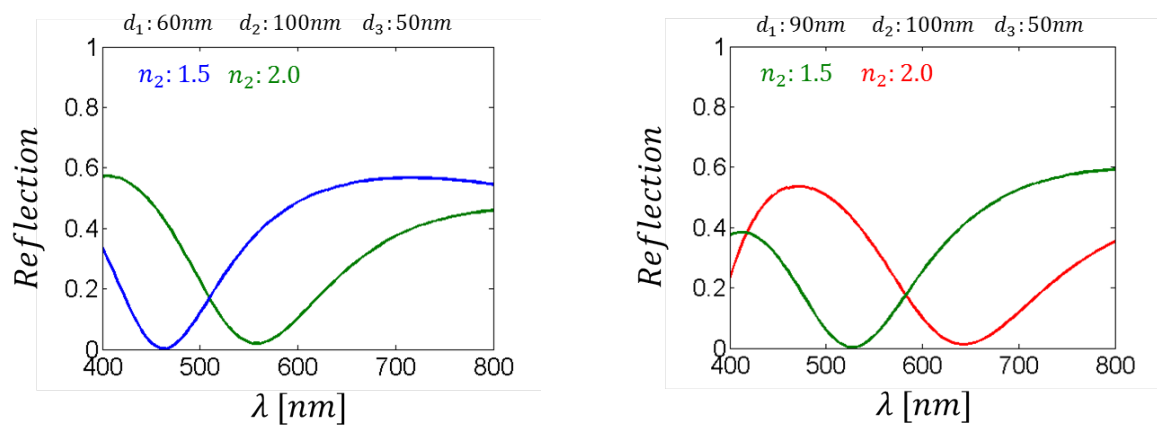
- (a) One grating stub must lie on junction of two antireflection structure

With the design guideline discussed previously, we investigate the three layer structure for sorting of visible light that could be used for color detection in imaging applications. Figure 4.17(a) shows the three layer structure on top of silicon, considered for the study. The thickness and refractive index of first, second and third layer coating is denoted as d_1 and n_1 , d_2 and n_2 , d_3 and n_3 , respectively.

First, we find the refractive index and thickness of each layers which could selectively antireflects blue and green light. The thickness of first, second and third layer coating is determined to be $d_1 : 60nm$, $d_2 : 100nm$ and $d_3 : 50nm$ respectively. The first and third homogenous layers of the structure antireflecting at blue and green light has same refractive index value of $n_1 : 2.1$ and $n_3 : 1.5$ respectively. Whereas the second layer of the structure designed to antireflect the blue light has refractive index value of $n_2 : 1.5$ and that for green light has refractive index value of $n_2 : 2.0$. Figure 4.17 (b) shows the reflection as a function of wavelength of the multilayer structure designed to antireflect blue and green light. For convenience, the layered system designed to antireflect blue and green light with these parameters will be called as $B1$ and $G1$ respectively.



(a)



(b)

(c)

Figure 4.17: (a) Three layer structure for selective antireflection of light, in which the thickness and index of first, second and third layer is denoted as d_1 and n_1 , d_2 and n_2 , d_3 and n_3 , respectively (b) Reflection as a function of wavelength of the three layer antireflection structure designed for blue-green light, with $d_1 : 60nm$, $d_2 : 100nm$ and $d_3 : 50nm$ and $n_1 : 2.1$, $n_2 : 1.5$ for blue, $n_2 : 2.0$ for green light and $n_3 : 1.5$ (c) Reflection as a function of wavelength of the three layer antireflection structure designed for green-red light, with $d_1 : 90nm$, $d_2 : 100nm$ and $d_3 : 50nm$ and $n_1 : 2.1$, $n_2 : 1.5$ for green, $n_2 : 2.0$ for red light and $n_3 : 1.5$

Secondly, we find the refractive index and thickness of each layer in multilayer structure which could selectively antireflects green and red light. Figure 4.17 (c) shows the reflection spectra of the multilayer structure designed to antireflect green and red light. Both structures have the same material with refractive index $n_1 : 2.1$ and $n_3 : 1.5$ in first and third layer respectively. Whereas the second layer of the structure designed to antireflect the green and red light has refractive index value

of $n_2 : 1.5$ and $n_2 : 2.0$ respectively. The thickness of first, second and third layer coating is determined to be $d_1 : 90nm$, $d_2 : 100nm$ and $d_3 : 50nm$ respectively. We call the structure designed to antireflect green and red light as $G2$ and $R1$ respectively.

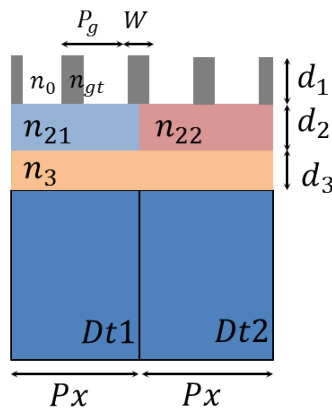
In section 6.2.3, we find that the sub wavelength grating structure could be modeled as homogenous layer with effective index determined by its period, width, and grating material and vice versa. We apply the effective medium theory to convert the first homogenous layer of the multilayer coating into the grating structure. The first homogenous layer of $B1$ and $G1$ is replaced by the periodic grating with period $P_g = 250nm$ and grating width $W = 88nm$. The thickness of this first layer is unchanged at $d_1 : 60nm$. Similarly the first homogenous layer of $G2$ and $R1$ is replaced by the grating with period $P_g = 250nm$ and grating width $W = 125nm$, while the grating thickness $d_1 : 90nm$ is unchanged. For all cases, the grating material with refractive index 2.5 is considered. The grating groove is considered to be air in the study.

Figure 4.18 (a) shows the unit cell of $B1$ and $G1$ arranged periodically, with one grating stub on the junction of second layer. The second layer of $B1$ and $G1$ are represented as n_{21} and n_{22} respectively for convenience. The silicon used in $B1$ and $G1$ are represented as $Dt1$ and $Dt2$ as can be viewed from figure 4.18 (a). The size of $Px : 0.5\mu m$ is considered for individual structure in the study.

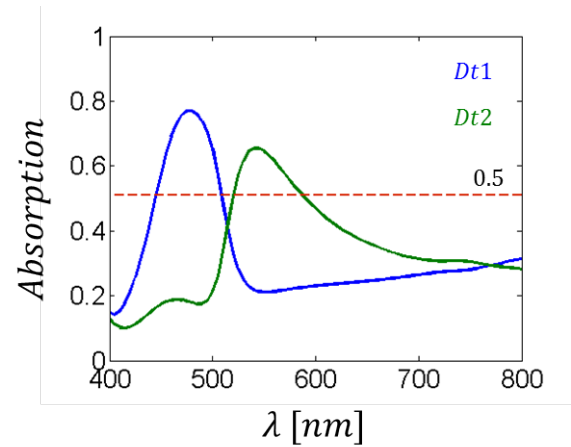
Figure 4.18 (b) shows the absorption in $Dt1$ and $Dt2$ as a function of incidence wavelength. It can be seen that the absorption peak in detectors $Dt1$ and $Dt2$ is higher than 50% (or 0.5) at $480nm$ and $540nm$ which corresponds to the reflection minima of $B1$ and $G1$ respectively. The absorption is normalized to the total power incident on a unit cell.

Figure 4.18 (c) and (d) shows the electromagnetic power dissipation along with time averaged power flow in the structure at $480nm$ and $540nm$ respectively. At

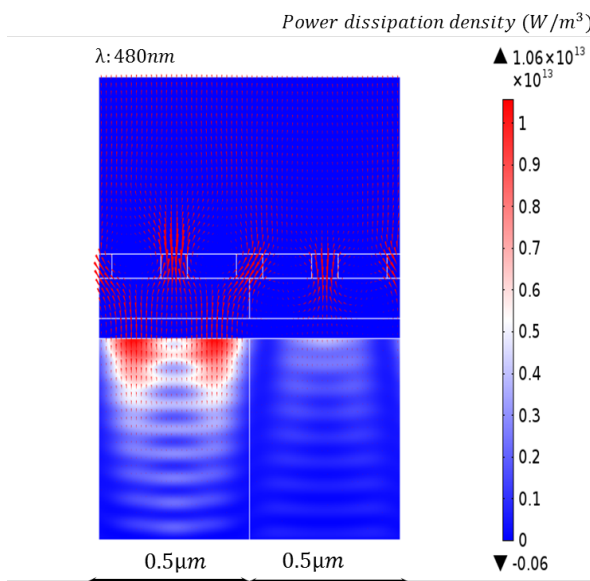
wavelength of peak absorption it can be seen that the grating stub in the junction of second layer provides the channel to direct the incidence power at adjacent structure to $Dt1$ and $Dt2$.



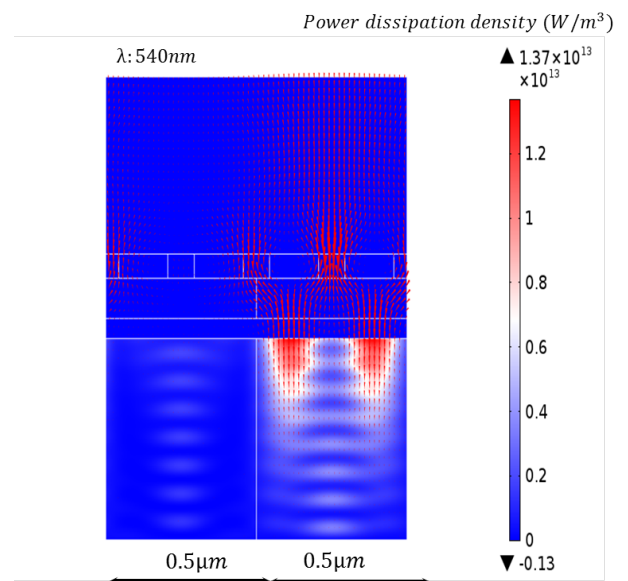
(a)



(b)

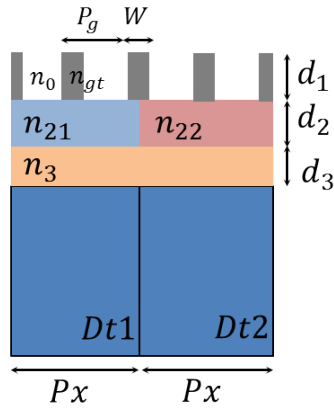


(c)

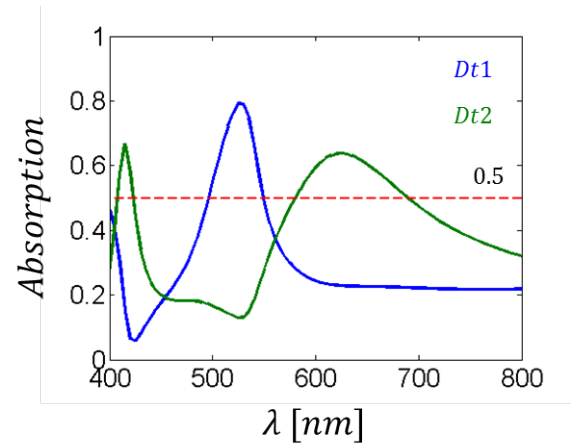


(d)

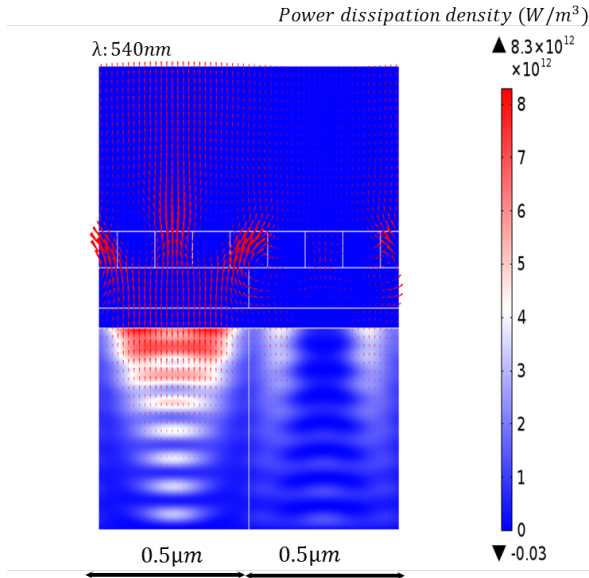
Figure 4.18: (a) Periodic arrangement of blue and green antireflecting structure ($B1$ and $G1$) with first grating layer, (b) Absorption spectra of $B1$ and $G1$ represented by blue and green curve respectively. Power dissipation in silicon as a function of spatial position at wavelength of (c) 480nm and (d) 540nm for periodic arrangement of $B1$ and $G1$ respectively



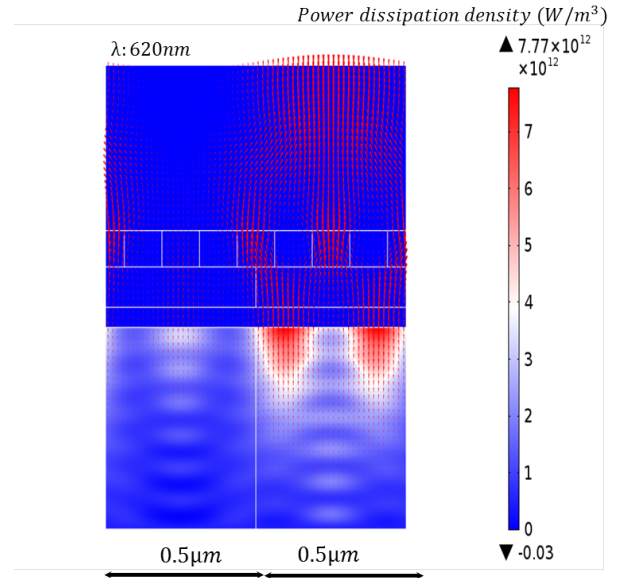
(a)



(b)



(c)



(d)

Figure 4.19: (a) Periodic arrangement of green and red antireflecting structure (*G2* and *R1*) with first grating layer, (b) Absorption spectra of *G2* and *R1* represented by blue and green curve respectively. Power dissipation in silicon as a function of spatial position at wavelength of (c) 540nm and (d) 620nm for periodic arrangement of *G2* and *R1* respectively

Similarly, figure 4.19 (a) shows the unit cell of *G2* and *R1* arranged periodically, with one grating stub on the junction of second layer. The second layer of *G2* and *R1* are represented as n_{21} and n_{22} respectively for convenience. The silicon used

in $G2$ and $R1$ are represented as $Dt1$ and $Dt2$. The size of $Px : 0.5\mu m$ is considered for individual structure in the study.

Figure 4.19(b) shows the absorption in $Dt1$ and $Dt2$ as a function of incidence wavelength. It can be seen that the absorption peak in detectors $Dt1$ and $Dt2$ is higher than 50% (or 0.5) at $540nm$ and $620nm$ which corresponds to the reflection minima of $G2$ and $R1$ respectively.

Figure 4.19 (c) and (d) shows the electromagnetic power dissipation along with time averaged power flow in the structure at $540nm$ and $620nm$ respectively. At wavelength of peak absorption it can be seen that the grating stub in the junction of second layer provides the channel to direct the incidence power at adjacent structure to $Dt1$ and $Dt2$. We find that using multilayered structure with grating; higher absorption efficiency in detector could be achieved at visible wavelengths. This could lead to development of submicron pixels for the imaging applications.

4.4 Conclusion

In this chapter, we studied the metallic and dielectric structures for sorting of visible light. Even though the metallic structures could sort the light, we found that the loss associated with metal is higher and limits the performance of the sorting structures. We also studied the dielectric based antireflection coating for localize sorting of visible light. Beginning with simple antireflection coating we developed the concept to achieve sorting of visible light. We find that using grating as the first layer could help achieve the sorting of light which results in higher absorption efficiency of detectors. We study two layer and three layer system and showed that the absorption in detector could be much higher than 50% if the first grating layer is arranged in array such that one of the grating stubs lies in the junction of second homogenous layer. Using such structures, we show the possibility of designing optically efficient submicron pixels for imaging application.

Chapter 5

Conclusion

The pixel size continues to shrink as the demand for imaging system with high density imaging pixels increases. The shrinking of pixel dimension however deteriorates the optical efficiency and therefore impose the tradeoff between the performance and minimum achievable pixel size in the imaging system. As the pixel size continues to shrink and approach the dimensions comparable to the wavelength, the spectral separation techniques used in current generation imaging system should be revised and new design methodologies have to be explored. This dissertation explored different techniques that could be used to efficiently sort the band of different wavelengths in far-infrared ($8\mu m - 12\mu m$) and visible ($0.4\mu m - 0.7\mu m$) spectrum in different spatial locations.

First we review the phase relief gratings especially binary and multilevel phase grating (Dammann grating) to efficiently split the colored light to detect complementary and fundamental colors that could be used for imaging system. We found that these structures need gratings with high aspect ratio and larger buffer layer between detector and grating thus making imaging system bulky. This necessitated exploring different techniques to make imaging system more compact. We find the optical resonator system as a good candidate for this purpose as it has higher scattering and absorption cross section at resonance. We discussed the antenna fundamentals

and antenna parameters for RF antenna which could also be applied to optical resonator system or optical antennas. We define the concept of spectral sorting based on normalized optical efficiency (*NOE*). For given number of pixels (N) or detectors, we define the phenomenon of sorting if *NOE* of individual pixels, considering incidence power from all pixel domain, is greater than $1/N$. We then numerically studied the optical patch antenna and found that arrangement of differently sized antenna could be utilized to efficiently sort the infrared light to different spatial locations. Using periodic array of such antenna arrangement we numerically and experimentally showed that the multi spectral and wide band absorption could be achieved with efficiency higher than 70%.

Finally, we analyzed the sorting of visible light. First we numerically investigated the Metal-Semiconductor-Metal (MSM) nanostructures in which semiconductor layer in the stack served as a detector. Depending on the width of MSM stripe the wavelength of absorption could be tuned to blue, green or red spectra of visible light. Arranging two differently sized MSM stripes periodically, and calculating absorption in detectors for a unit cell, we found that the absorption higher than 50% could be achieved in individual detectors. This indicated that the sorting is possible using MSM structure in visible domain. However, we also found that the losses associated with metallic layers are also significant and inevitable. The requirement of smaller dimensions and metallic losses in MSM nanostructure is found to limit the achievable optical efficiency. This necessitated the investigation of dielectric based structure to achieve sorting and increasing optical efficiency of color detector.

To find the dielectric based sorting structure; we first investigated the antireflection property of multilayer dielectric coating on silicon. We then apply effective medium theory and replaced one of the homogenous layers in multilayer coating by subwavelength grating structure and showed that high optical efficiency could be achieved for visible detectors. We found that such structures are most efficient when the

detector size is less than $1\mu m$, enabling to shrink the pixel size comparable to wavelength. The comprehensive design strategy is derived that could be used as design guideline to achieve sorting of visible light. Using those guidelines, we then studied a three layer dielectric structure to achieve sorting of blue green and red colored light. We showed that even for pixel size as less as $0.5\mu m$ high optical efficiency could be achieved.

With the miniaturization of thermal and visible imaging system, different methodologies to achieve higher optical efficiency have been continuously studied. The spectral sorting devices discussed in this dissertation have several immediate paths to the application and improvements. The optical patch antenna based sorting structure could be integrated to bolometers. This could lead to new developments in the field of thermal imaging system and CMOS compatible micro bolometer. The investigation made on dielectric structure provides an understanding of how the grating based antireflection coating could be utilized to achieve sorting of visible light and high optical efficiency in submicron sized pixels. However, the technological issues of efficient charge extraction from such small pixel have yet to be resolved. In the near future, we are convinced that these investigations will lead to optical and technological research dedicated to very high density pixel imaging system in visible domain.

Appendix A

Antenna Fundamentals

Antenna is a transducer which confines the electromagnetic wave propagating in free space into small volume and converts to electrical signal and vice versa. In transmission mode, it converts the applied electrical signal into a propagating electromagnetic wave, whereas in receiving mode an antenna converts the electromagnetic wave into an electrical signal. The antenna theory has been successfully developed and applied for radio frequency (RF) spectrum; however the theory can also be used to understand the basic characteristics of optical antenna system.

In this chapter, we review the basics of antenna theory and key antenna parameters that are required to define the antenna characteristics. We will briefly review different types of antenna systems that are commonly used.

A.1 Antenna and Electromagnetic Radiation

The electromagnetic radiation is created by the system of charged particles, when the electric dipole moment or magnetic dipole moment is varied with time. For example, two charge particles separated by distance l with individual charges $+q$ and $-q$ that oscillates as $q = q_0 \cos \omega t$ (for which the corresponding dipole moment oscillates as $p = q_0 l \cos \omega t$) as shown in figure A.1 (a), radiates an electromagnetic field with

frequency ω . Such kind of dipole can be created by applying alternating current (AC current) to an antenna as shown in figure A.1 (b). Similarly, the magnetic dipole can be created with the current loop of area A in which current varies as $I = I_0 \cos \omega t$ (magnetic dipole moment $\vec{m} = I \vec{A}$) as shown in figure A.1(c).

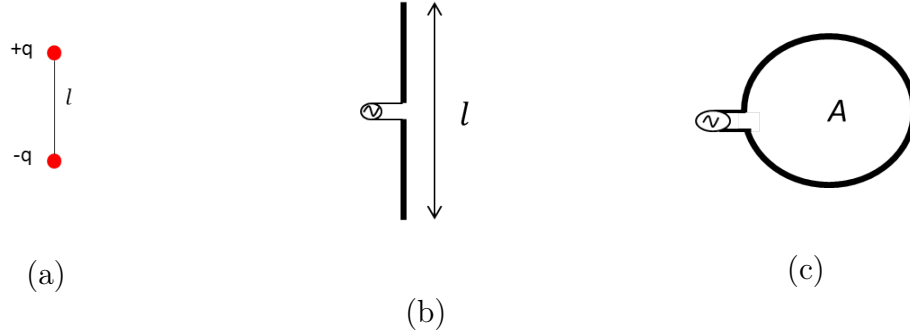


Figure A.1: (a) electric dipole (b) electric dipole antenna fed with alternating current (c) magnetic dipole with current loop of area A

The electromagnetic field radiated by such an antenna can be computed by solving the Maxwell's equations, in presence of time dependent current fed into the antenna. For an arbitrary volume V , the basic problem is to compute electric field \vec{E} and magnetic field \vec{H} for given electric current density \vec{J} [A/m^2] by solving Maxwell's equation for time harmonic fields:

$$\nabla \cdot \vec{D} = \rho_v \quad (\text{A.1})$$

$$\nabla \cdot \vec{B} = 0 \quad (\text{A.2})$$

$$\nabla \times \vec{E} = -j\omega \vec{B} - \vec{M} \quad (\text{A.3})$$

$$\nabla \times \vec{H} = j\omega \vec{D} + \vec{J} \quad (\text{A.4})$$

With constitutive relationship:

$$\vec{D} = \bar{\epsilon}\vec{E} \quad (\text{A.5})$$

$$\vec{B} = \bar{\mu}\vec{H} \quad (\text{A.6})$$

D : Electric displacement (C/m^2)

B : Magnetic flux density (*Tesla*, T)

E : Electric field (V/m)

H : Magnetic field (A/m)

J : Electric current density (A/m^2)

M : Magnetic current density (V/m^2)

ρ : Electric charge density (C/m^3)

ϵ : Permittivity (*farads/m*)

μ : Permeability (*henries/m*)

ω : Circular frequency (*rad/s*)

Using above sets of equation, we can find the wave equation for the electromagnetic wave propagating in source free environment as:

$$[\nabla^2 + \kappa^2]\vec{E} = 0 \quad (\text{A.7})$$

Where $\kappa = \frac{\omega}{c}$ is the wave number and $c = \frac{1}{\sqrt{\mu\epsilon}}$ is the speed of electromagnetic wave radiated from antenna. However, the common approach is to use the magnetic vector potential \vec{A} and electric scalar potential φ which satisfies the wave equations [64]:

$$[\nabla^2 + \kappa^2]\vec{A} = -\mu\vec{J} + \nabla[\nabla\cdot\vec{A} + j\omega\mu\epsilon\varphi] \quad (\text{A.8})$$

And using Lorenz condition

$$\nabla\cdot\vec{A} = -j\omega\mu\epsilon\varphi \quad (\text{A.9})$$

The wave equation can be written simply as:

$$[\nabla^2 + \kappa^2]\vec{A} = -\mu\vec{J} \quad (\text{A.10})$$

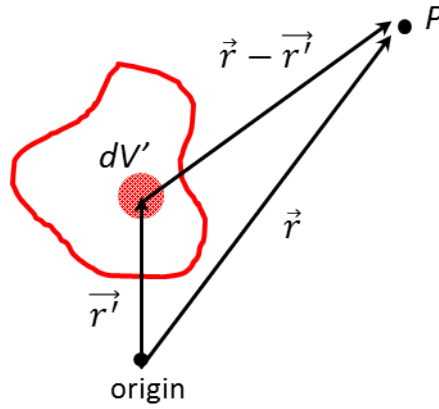


Figure A.2: Radiating object of arbitrary volume V with source \vec{J}

From the known \vec{J} we only need to compute the magnetic vector potential \vec{A} to find the radiated fields. For any observation point P at location \vec{r} from the origin as shown in figure A.2, the vector potential created due to radiating object located at (\vec{r}') with arbitrary volume V and source \vec{J} , can be found by solving wave equation A.10 and is given by:

$$\vec{A}(\vec{r}) = \frac{\mu}{4\pi} \iiint_V \vec{J}(\vec{r}') \frac{e^{-jk|\vec{r} - \vec{r}'|}}{|\vec{r} - \vec{r}'|} d\vec{r}' \quad (\text{A.11})$$

The radiated fields \vec{E} and \vec{H} can then be computed using following relations:

$$\mu \vec{H} = \nabla \times \vec{A} \quad (\text{A.12})$$

$$\vec{E} = -\nabla\varphi - j\omega \vec{A} \quad (\text{A.13})$$

A.2 Antenna Radiation Parameters

A.2.1 Radiation pattern

A Radiation pattern of an antenna is a spatial distribution of the radiation properties like radiation power density, radiation power intensity as a function of far field angles (θ, ϕ) at fixed radial location \vec{r} . For given antenna with largest dimension D the far field is defined as the region $r \geq \frac{(2D^2)}{\lambda}$ where angular field distribution is independent of distance. Radiation power density is the most common quantity used to represent the radiation pattern. It characterizes the radiated power of an antenna. In frequency domain it is calculated using following relation:

$$\vec{W} = \frac{1}{2} \text{Re} \left\{ \vec{E}(\theta, \phi) \times \vec{H}^*(\theta, \phi) \right\} \quad (\text{A.14})$$

Where \vec{E} and \vec{H}^* are electric field and complex conjugate of magnetic field respectively. The magnitude of \vec{W} represents the power radiated from an antenna per unit area in given direction. We can visualize the radiation pattern, by plotting $\vec{W}(\vec{r})$ as a function of elevation (θ) and azimuth angle (ϕ) for fixed r .

In Figure A.3 we can see some examples of antenna radiation patterns. Radiation pattern in figure A.3 (a) is an omnidirectional one in which the radiated field is constant in azimuth angles (ϕ) . It can also be directional as shown in figure A.3 (b) in which the radiated field is concentrated in some directions.

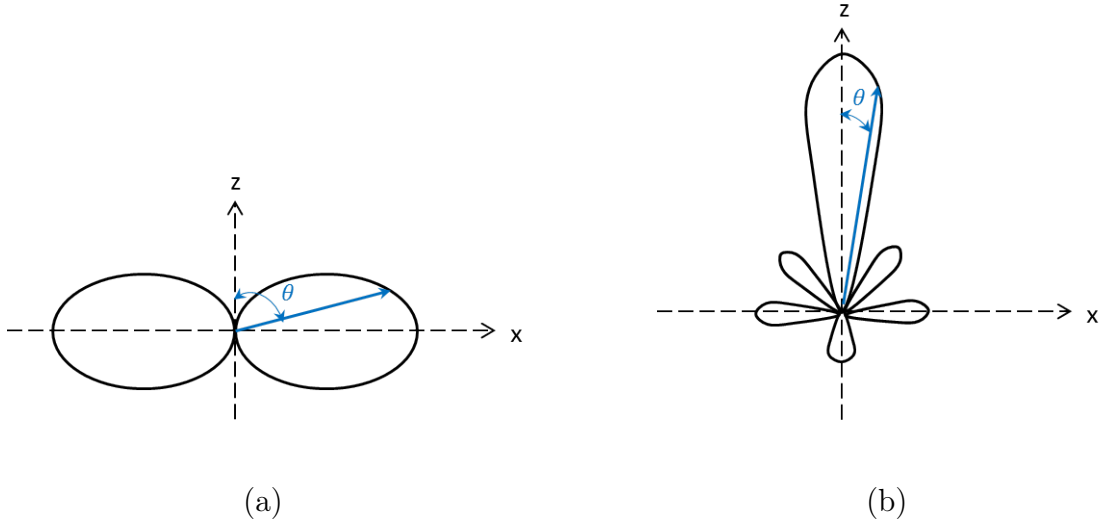


Figure A.3: (a) Omni directional antenna pattern (b) Directional antenna pattern

A.2.2 Antenna Directivity

Radiation power density \vec{W} can be normalized such that it represents the power per unit solid angle. This quantity is called radiation intensity and is given by:

$$U(\theta, \phi) = r^2 W(r, \theta, \phi) \quad (\text{A.15})$$

The ratio of maximum radiation intensity of given antenna to radiation intensity of an isotropic antenna gives another important antenna parameter called directivity $D(\theta, \phi)$. Isotropic antenna is an ideal antenna which radiates power equally in all direction for which radiation intensity is given by:

$$U_0 = \frac{P_{rad}}{4\pi} \quad (\text{A.16})$$

Using equation A.15 and A.16, directivity of an antenna can be calculated as:

$$D(\theta, \phi) = \frac{\max U(\theta, \phi)}{U_0} \quad (\text{A.17})$$

A.2.3 Antenna Gain

Antenna gain is another important parameter which describes how efficiently the power fed into an antenna is radiated. For a given antenna it relates directivity and antenna efficiency as given in equation A.18. Antenna gain is basically the power radiated by an antenna relative to isotropic antenna which radiates all input power.

$$G(\theta, \phi) = \frac{U(\theta, \phi)}{\left(\frac{P_{in}}{4\pi}\right)} = e_t D(\theta, \phi) \quad (\text{A.18})$$

Here e_t is the total antenna efficiency. It is the measure of how much input power is radiated in form of electromagnetic wave.

$$e_t = \frac{P_{rad}}{P_{in}} = \frac{R_{rad}}{R_{rad} + R_{ohm}} \quad (\text{A.19})$$

In equation A.19 R_{rad} is the radiation resistance and R_{ohm} is the Ohmic resistance of an antenna which can be expressed as:

$$R_{rad} = \frac{2P_{rad}}{|I|^2} \quad (\text{A.20})$$

$$R_{ohm} = \frac{2(P_{in} - P_{rad})}{|I|^2} \quad (\text{A.21})$$

Where I is the current fed in an antenna. All the antenna parameters discussed in previous sections are based on transmitting antenna, however because of reciprocity theorem; it also applies to receiving antennas. For example, the radiation pattern of a reciprocal antenna is identical to its reception pattern. In short, the reciprocity theorem for antenna implies that the response will be the same if we interchange the roles of transmitter and receiver antenna. Because of this reciprocity, we can predict the behavior of receiving antenna, with the information of its radiation characteristics when operated in transmitting mode.

A.2.4 Friis transmission equation and antenna aperture

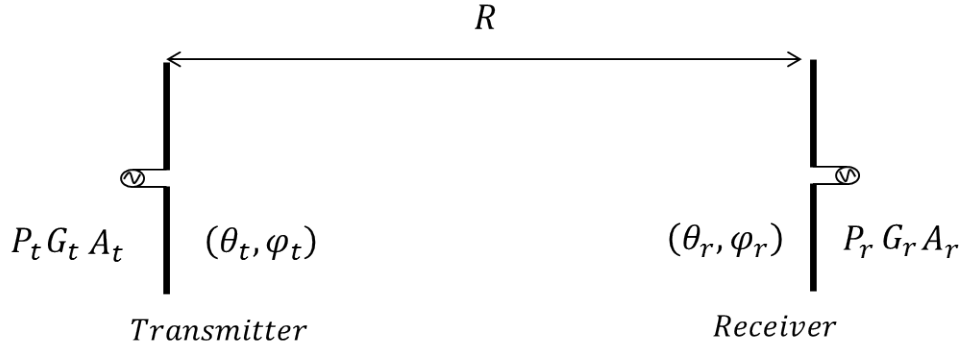


Figure A.4: Transmitting and receiving antennas separated by distance R

Friis transmission equation relates the power received by a receiving antenna to the power transmitted by a transmitting antenna. The notion of aperture or effective collection area is introduced to get an idea of how much power is collected by a receiving antenna. It is defined as the ratio of power absorbed by a receiving antenna to power density of the incident electromagnetic wave:

$$A_r = \frac{P_r}{W_t} \quad (\text{A.22})$$

Consider the antenna system shown in figure A.4, in which transmitting and receiving antennas are separated by distance R . P_t , G_t , A_t are the transmitted power, transmit gain and transmit aperture of a transmitting antenna, then the radiated power density at receiving antenna due to transmitting antenna is:

$$W_t = \frac{P_t G_t(\theta_t, \phi_t)}{4\pi R^2} \quad (\text{A.23})$$

If A_r is the effective collection area from which the incident power is captured by receiving antenna then the received power is given by:

$$P_r = A_r W_t = \frac{P_t G_t A_r}{4\pi R^2} \quad (\text{A.24})$$

Rearranging equation A.24, we get

$$G_t A_r = \frac{4\pi R^2 P_r}{P_t} \quad (\text{A.25})$$

If we interchange the role of transmitting and receiving antennas, then from reciprocity theorem we can say that the received power will be the same:

$$P_r = \frac{P_t G_r A_t}{4\pi R^2} \quad (\text{A.26})$$

Rearranging equation A.26, we get

$$G_r A_t = \frac{4\pi R^2 P_r}{P_t} = G_t A_r \quad (\text{A.27})$$

This gives the relation between the gain and effective absorption area of an antenna as:

$$\frac{G_r}{A_r} = \frac{G_t}{A_t} \quad (\text{A.28})$$

Since we have considered arbitrary antennas for transmitter and receiver, and do not specify the type of antenna used for the analysis, the relation in equation A.28 should hold for any kind of antenna. This means for any given antenna:

$$\frac{G}{A} = \text{constant} \quad (\text{A.29})$$

To find this constant, we consider an infinitesimal dipole antenna whose gain and aperture is already known to have values of 1.5 and $\frac{3\lambda^2}{8\pi}$ respectively. Then the constant in equation A.29 can be calculated:

$$\frac{G}{A} = \frac{3/2}{3\lambda^2/8\pi} = \frac{4\pi}{\lambda^2} \quad (\text{A.30})$$

Therefore the effective absorption area or aperture of any antenna can have maximum value of:

$$A = \frac{G\lambda^2}{4\pi} \quad (\text{A.31})$$

We can see that the aperture of given antenna is solely depends on gain of an antenna. From equation A.18 we see that gain is dependent on the directivity and total efficiency of an antenna. Therefore we can say that an antenna has maximum collection area if the radiation pattern or directivity of a receiving antenna is matched with that of incident wave or transmitting antenna.

A.2.5 Antenna Bandwidth and Quality factor

Antenna is designed to transmit or receive over specific wavelengths. The range of frequencies or wavelengths over which antenna works well to some specified standard like gain, efficiency, beam width is known as antenna bandwidth. If f_{max} and f_{min} are the maximum and minimum frequencies of operation for given antenna; bandwidth of an antenna is expressed as [64, 65, 66]:

$$BW = \frac{f_{max} - f_{min}}{f_c} \quad (\text{A.32})$$

The quality factor (Q) of an antenna is another parameter to quantify the bandwidth of an antenna [65, 66, 67], which is inverse of BW given in equation A.32:

$$Q = \frac{1}{BW} = \frac{f_c}{f_{max} - f_{min}} \quad (\text{A.33})$$

Appendix B

Dielectric Properties of Metal:

Drude model

Optical properties of a metal can be described using plasma model. Electrons are treated as quasi free particles of which equation of motion subjected to electric field \vec{E} is given by:

$$m\ddot{x} + m\gamma\dot{x} = -e\vec{E} \quad (\text{B.1})$$

Where, m , γ and e are the effective mass, the collision frequency of free electron gas and electron charge respectively. Electron-electron interaction, inter band transition and lattice potentials are not considered in this model. For time harmonic field oscillating at angular frequency ω , $E(t) = E_0e^{-i\omega t}$ the solution for equation of motion B.1 is given by $x(t) = x_0e^{-i\omega t}$, where x_0 is complex amplitude. Incorporating the phase shifts between driving field and response to applied field, the solution to B.1 can be written as:

$$x(t) = \frac{e}{m(\omega^2 + i\gamma\omega)} \vec{E} \quad (\text{B.2})$$

The displaced electron in response to driving field induces a dipole leading to macroscopic polarization $\vec{P} = -nex$, where n is the number of electrons per unit volume. Using B.2 it can be written as:

$$\vec{P} = -\frac{ne^2}{m(\omega^2 + i\gamma\omega)}\vec{E} \quad (\text{B.3})$$

Then electric displacement is given by:

$$\vec{D} = \vec{P} + \epsilon_0\vec{E} = \epsilon_0\left(1 - \frac{\omega_p^2}{\omega^2 + i\gamma\omega}\right)\vec{E} \quad (\text{B.4})$$

Where, $\omega_p^2 = \frac{ne^2}{m\epsilon_0}$ is the plasma frequency of free electron gas and ϵ_0 is the electric permittivity of free space. The dielectric function of a metal is then given by:

$$\epsilon(\omega) = \epsilon'(\omega) + i\epsilon''(\omega) = 1 - \frac{\omega_p^2}{\omega^2 + i\gamma\omega} \quad (\text{B.5})$$

The real and imaginary parts of dielectric function B.5 are:

$$\epsilon'(\omega) = 1 - \frac{\omega_p^2}{\omega^2 + \gamma^2} \text{ and } \epsilon''(\omega) = \frac{\omega_p^2\gamma}{\omega^2 + \gamma^2\omega} \quad (\text{B.6})$$

The metal behaves differently depending on the frequency of driving field [68]. For $\omega \ll \gamma$, the metals are absorbing and field penetrates into metal. This effect is called skin effect. The characteristic depth of field penetration is called skin depth and is given by $\delta_{skin} = \sqrt{\frac{2\rho}{\omega\mu_0}}$, where ρ , μ_0 are resistivity and free space magnetic permeability respectively. When $\gamma \ll \omega < \omega_p$, the dielectric function is negative. The refractive index is imaginary which means in this regime metals are highly reflective. In frequency regime $\omega > \omega_p > \gamma$, the dielectric function is positive and the metal becomes transparent at this regime.

Appendix C

Experimental Setup-Total Reflection

For total reflection measurement of the fabricated antenna array, FTIR Bruker A 562-G with integrated Sphere is used. The vertical plane schematic for the arrangement is shown in figure C.1.

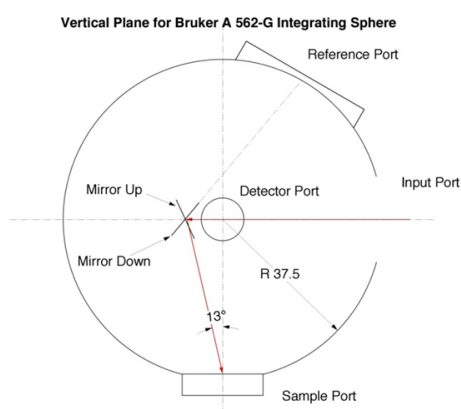


Figure C.1: Experimental setup for total reflection measurement of antenna array

The sphere has the input port diameter 2cm, sample port diameter 1.9cm and reference port diameter of 3.2cm. The MCT detector and global source is used in the measurement.

Appendix D

Review: Far Field Spectral Sorting

D.1 Fundamental color sorting- complementary color detection: Binary Phase Grating

Binary phase grating has been widely used for imaging and beam splitting of monochromatic incident light [69, 70]. Here, we consider a periodic binary phase grating as shown in figure D.1. The grating period is represented by P and the width of grating is represented by fP where f is the filling factor of grating. The grating relief height is represented by h . n_g and n_0 are refractive indices of incident medium and grating respectively.

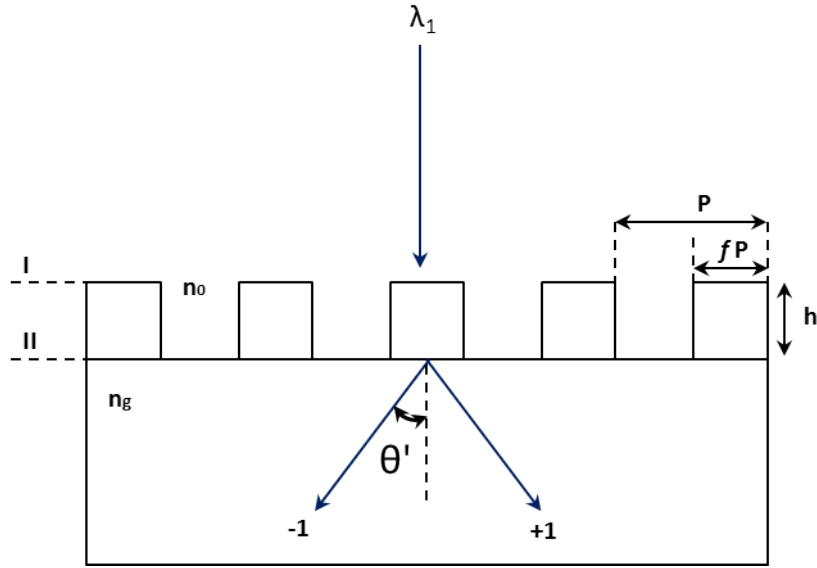


Figure D.1: Binary grating structure for beam splitting

Here, we choose $n_0 = 1.0$ and $n_g = 1.5$. The substrate has the same refractive index as the grating. To split the waves with wavelengths λ_1 into positive first order and negative first order, grating height could be appropriately chosen such that the incident plane waves propagating in grating relief and groove, experiences the phase difference of π radian (or $\lambda_{1/2}$ delays) at interface II. The grating height can be calculated using scalar diffraction theory, as given in equation D.1.

$$\frac{n_g - n_0}{\lambda_1} h = p + \varphi \quad (\text{D.1})$$

Where φ is either 0 (for 0 or 2π phase difference) or $\frac{1}{2}$ (for π phase difference), and p is an integer. With $\varphi = \frac{1}{2}$, $p = 1$, and choosing $\lambda_1 = 450nm$, grating height of $1350nm$ is calculated using above equations. Wavelength dependent diffraction efficiency for normal incidence is then calculated for grating period of $10\mu m$ with filling factor f of 0.5. Figure D.2 shows the diffraction efficiency of the grating.

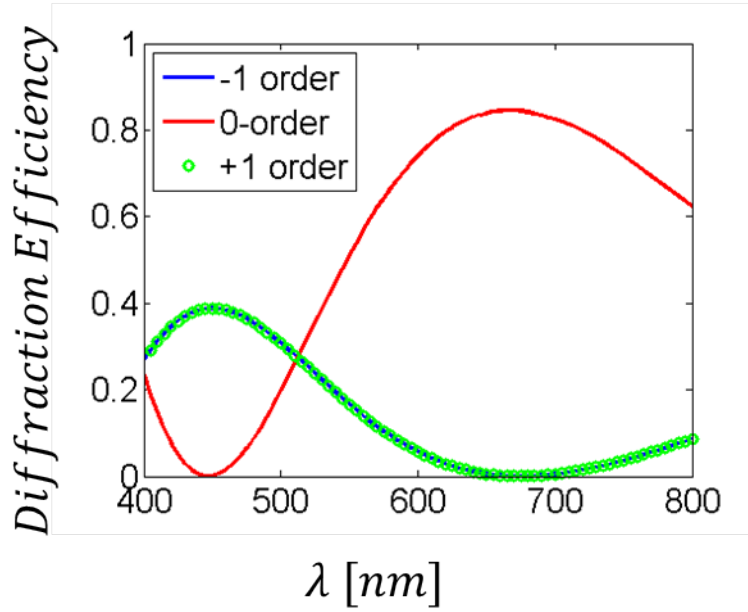


Figure D.2: Diffraction efficiency of grating with $h = 1350nm$, $P = 10\mu m$ and $f = 0.5$

It can be seen that using binary grating which split blue light into first diffraction order, we get yellow (white minus blue) in zero order diffraction. Utilizing three different binary gratings which could split blue, green and red light into first diffraction order, we can achieve multicolor scheme of complementary colors cyan (white minus red), magenta (white minus green) and yellow (white minus blue) in zero order diffraction of the grating. However for larger grating period ($P > 5\mu m$) the angle for first order diffraction is less than 5° as can be seen in figure D.3. This sets the condition to have thicker buffer layer ($> 50\mu m$) between grating and detector. For the grating period less than $2\mu m$, the diffraction angle as high as 20° could be obtained. This provides good spatial separation of diffracted first and zero order lights. It is therefore interesting to study and design the binary grating with period less than $2\mu m$. However, more rigorous grating analysis is required for the analysis and design of binary grating in this region since the scalar grating theory cannot predict the accurate diffraction behavior of the grating structure [51].

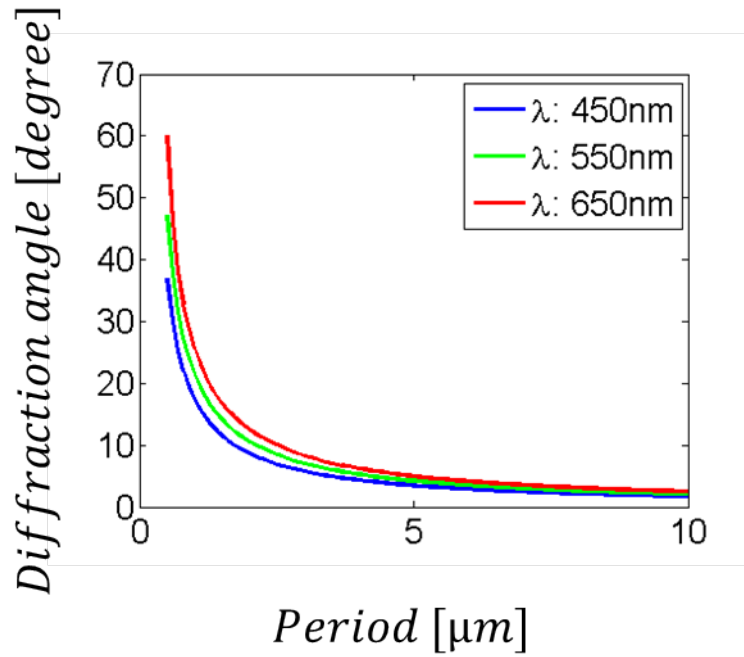


Figure D.3: Diffraction angle of first order diffracted light as a function of grating period

Using Rigorous Coupled Wave Analysis (RCWA) we studied the wavelength dependent diffraction efficiency of binary grating with grating period less than $2\mu\text{m}$ for TM polarized light at normal incidence. Silicon dioxide (SiO_2) is used as grating and substrate material while incidence medium of air is considered for the study. The equation D.1 for calculating grating height still applies for period less than $2\mu\text{m}$ however for optimal diffraction efficiency optimization has to be done. Figure D.4(a) shows the diffraction efficiency of grating ($G1$) with period (P) 800nm , and grating height (h) of 2884nm . For these grating parameters the blue light is diffracted into positive first order and negative first order with angle of 23° , while yellow light is transmitted in zero order normally. Figure D.4(b) shows the diffraction efficiency of grating ($G2$) with period 1000nm and grating height of 3522nm . The green light is diffracted into positive first order and negative first order with angle of 22° , while magenta light is transmitted in zero order. Similarly figure D.4(c) shows the diffraction efficiency for grating ($G3$) with period 1200nm and grating height of 4374nm .

In this case the red light is diffracted into first orders with diffraction angle of 23° and cyan light is transmitted in zero order. The grating filling factor (f) of 0.5 is used for all the gratings in this study. Since the diffraction angle for all three fundamental colors using these grating structures are nearly same ($\sim 23^\circ$), the buffer layer thickness of $5\mu\text{m}$ between grating and detector is sufficient to spatially separate the separated lights.

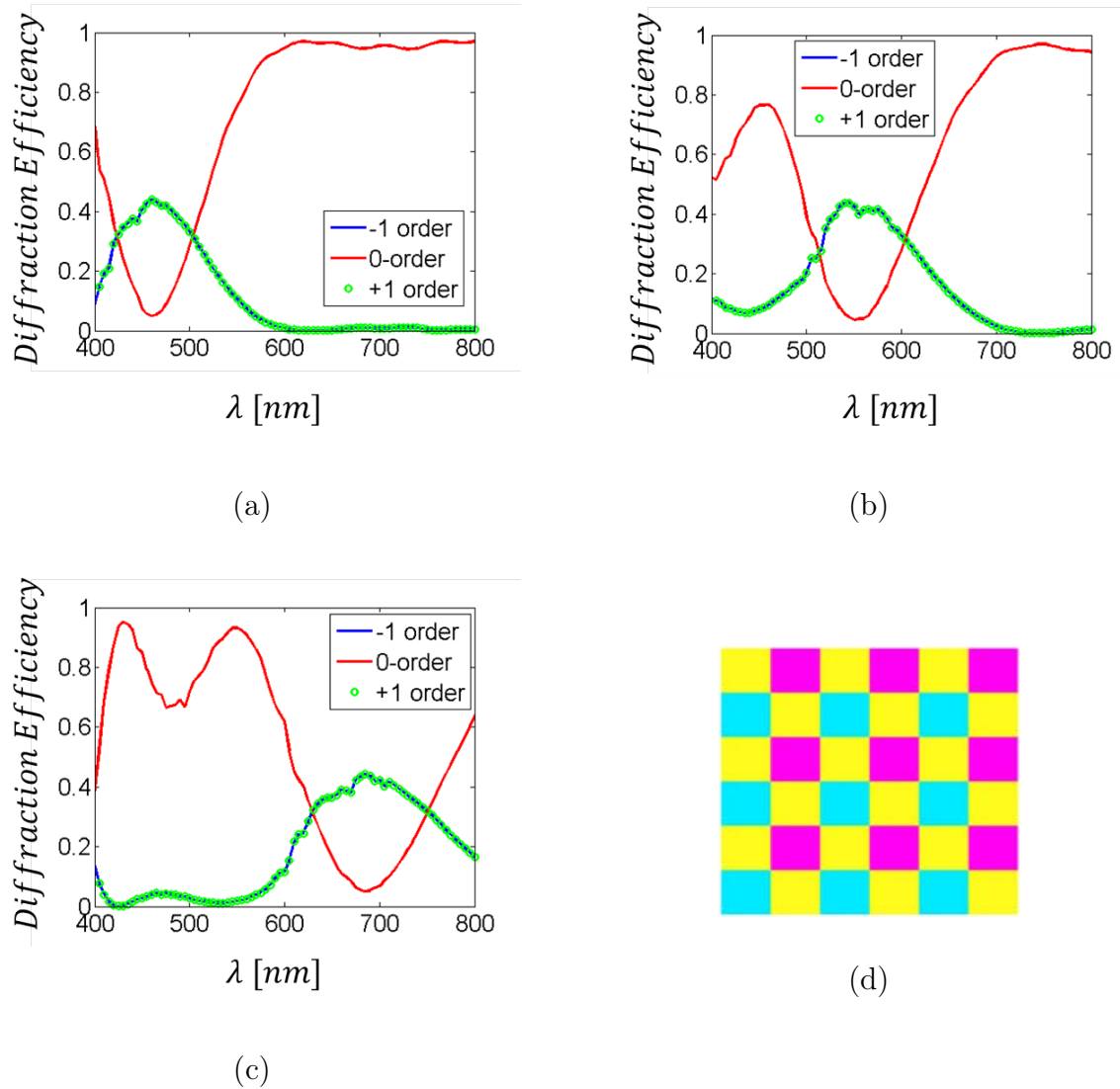


Figure D.4: Diffraction efficiency of grating with (a) $P : 800\text{nm}$, $h : 2884\text{nm}$, (b) $P : 1000\text{nm}$, $h : 3522\text{nm}$, (c) $P : 1200\text{nm}$, $h : 4374\text{nm}$ (d) mosaic to detect complementary colors

Combining these three gratings we can make the mosaic to detect the complementary colors as shown in figure D.4(d). The first two gratings $G1$ and $G2$ which diffract blue and green light into first diffraction order can be put adjacent to each other to filter yellow and magenta colored light. Size of buffer layer between grating and detector associated with yellow and magenta color can be adjusted such that, the blue color diffracted by $G1$ is also detected by magenta detector and green color diffracted by $G2$ is detected by yellow detector as shown in figure D.5(a). Similarly two gratings $G1$ and $G3$ can be combined to filter yellow and cyan colored light.

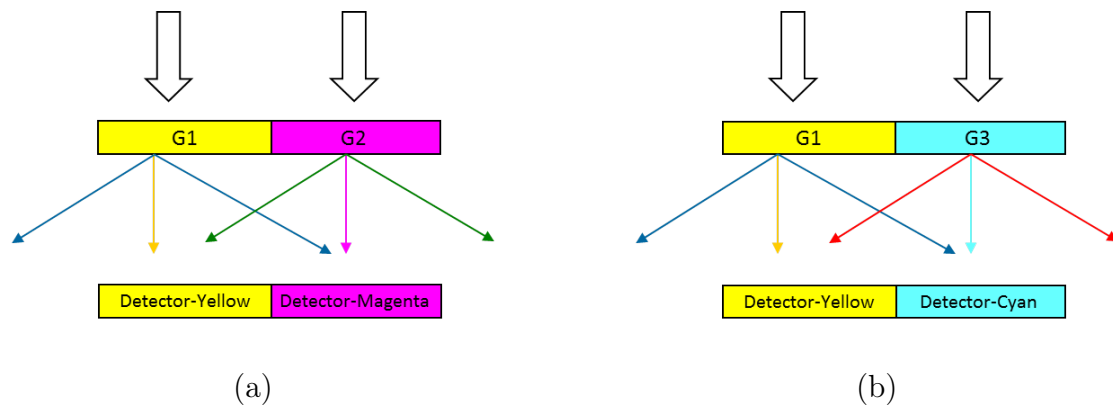


Figure D.5: Color detection scheme for complimentary color (a) Combination $G1$ and $G2$, (b) Combination of $G1$ and $G3$

The buffer layer can be adjusted such that, the blue light diffracted by $G1$ is also detected by cyan detector and red light diffracted by $G3$ is also detected by yellow detector as shown in figure D.5(b). It is to be noticed that the additional color light coming from adjacent grating array does not change the detected colors. Using binary grating, we can therefore spatially sort the fundamental color components, red, green, blue and combine them with the zero diffraction order light of adjacent gratings to detect complementary colors, yellow, magenta and cyan.

D.2 Fundamental color sorting-Fundamental color detection: Multilevel Phase Grating

In this section the multilevel phase grating concept developed by Dammann for fundamental color separation is discussed. The grating is designed such that the fundamental color components blue, green and red are distributed to central diffraction orders, $+1$, 0 , -1 , of the grating. For that the stepped-phase functions are proposed on the basis of blazed synthetic phase-only holograms [50], considering the fact that the phase is different for different wavelength when it propagates through the medium. Figure D.6 shows the simple 3-step grating designed for color separation. The grating can be designed to perform optimally by adding different phase delays of integral multiples of 2π to diffract red light to negative first order, green light to zero order and blue light to positive first order. The relation between the groove height h_k and the k level phase of the grating φ_k is then given by [50, 71]:

$$h_k = \frac{(\lambda_{design} * \varphi_k(\lambda_{design}))}{(2\pi(n - 1))} \quad (D.2)$$

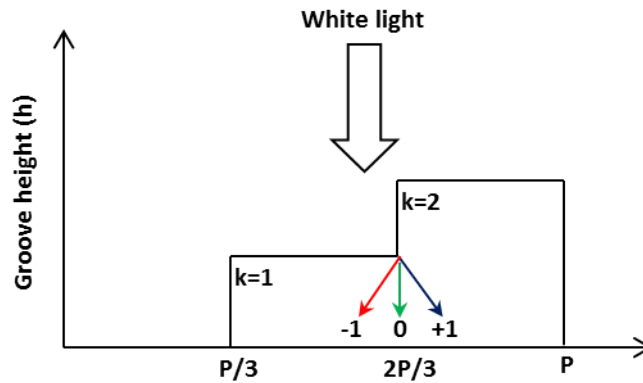


Figure D.6: 3- level color separation grating (two phase levels + ground level)

Where h is the groove height, λ_{design} is the wavelength, φ is the phase and n is the refractive index of grating and substrate. To diffract red light (R) into negative first

order, green (G) into zero order and blue (B) into positive first order, the phases corresponding to R, G, B should satisfy:

$$\varphi_{Bk} = \frac{2k\pi}{L}(L - 1) + 2qk\pi \quad (\text{D.3})$$

$$\varphi_{Gk} = 2qk\pi \quad (\text{D.4})$$

$$\varphi_{Rk} = \frac{2k\pi}{L} + 2qk\pi \quad (\text{D.5})$$

Where L is the number of grating levels and q is the integer number. Figure D.7 (a) shows the efficiency of central diffraction orders as a function of incident wavelengths for normal incidence. It is calculated for three-level grating and TM polarization using rigorous coupled wave analysis. The grating period of $18\mu\text{m}$ is used for study. The refractive index of $n = 1.5$ is used for grating and substrate. The incidence medium of air is considered. With q fixed to 2 in equation-D.3 to D.5, the groove height h_k of 2100nm is calculated using equation-D.2 for designed wavelength of 550nm . It can be seen that the grating splits the white light into three color components blue, green and red into central diffraction orders of $+1, 0, -1$ respectively. Using such grating, one can generate stripe of red, green and blue colors which could be used for color Liquid-crystal-spatial light modulator [72], color imaging devices, wavelength division multiplexing [15] and other potential applications.

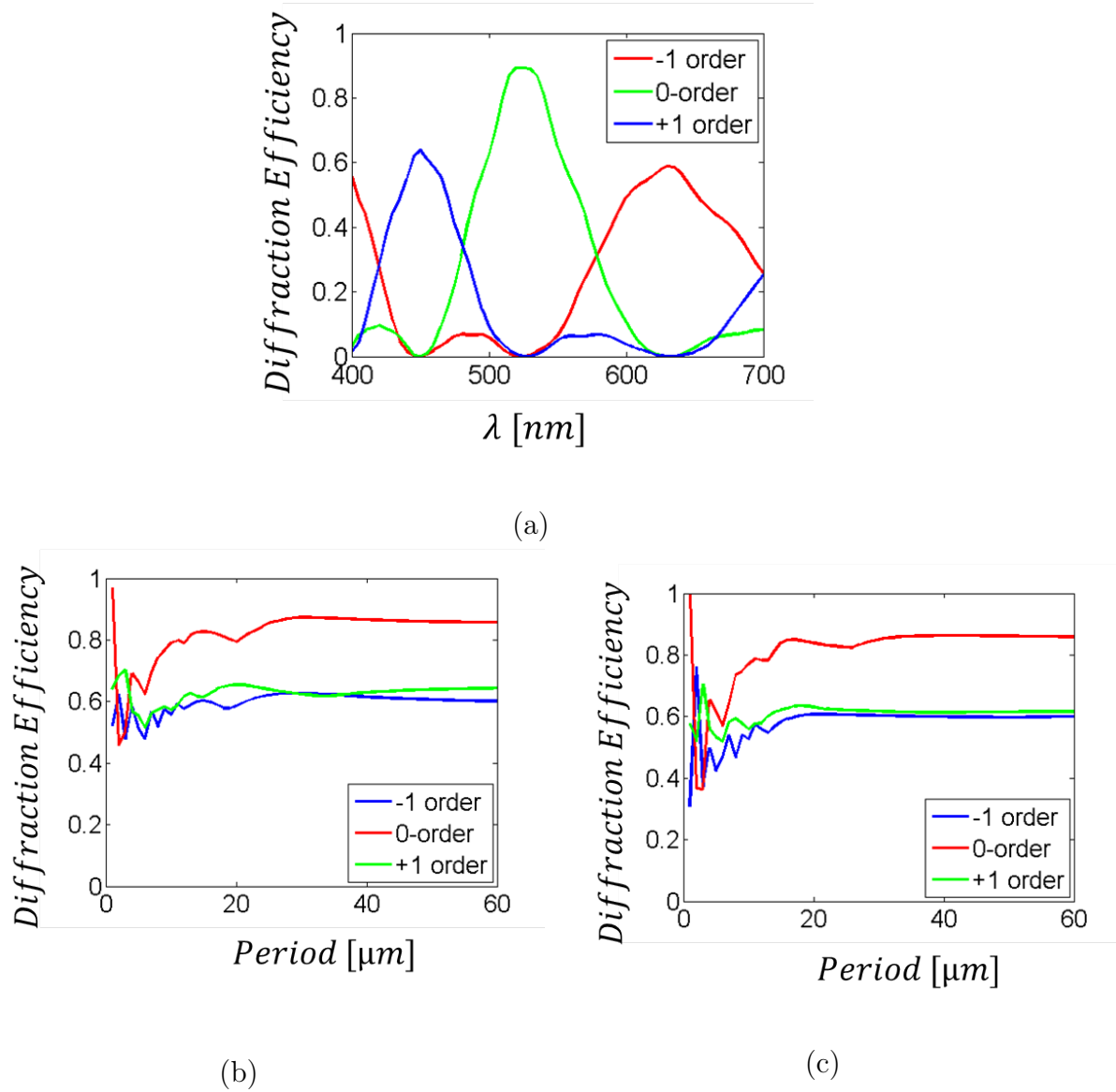


Figure D.7: (a) Diffraction efficiency as a function of wavelength for central diffraction orders, -1, 0, and +1. Diffraction efficiency as a function of grating period, (b) TE illumination (c) TM illumination.

Figure D.7(b) and (c) shows the maximum diffraction efficiency achievable for central diffraction orders for 3-level grating as a function of grating period for TE and TM illumination respectively. The groove height h_k of 2100nm is considered for the study. For grating period higher than 20 μm , the efficiency is quite stable, with highest efficiency ($\sim 80\%$) achieved for light diffracted in zero order. For light diffracted in positive first order and negative first order, the maximum achievable efficiency

using 3-level grating is 60%. However, for lower grating period, the diffraction efficiency could decrease to 40% as can be seen in figure D.7 (c). As shown in [71], the efficiency can decrease to value as low as 10% for lower grating periods even with higher numbers of phase levels. Such grating can therefore be used for diffractive optic application which requires higher grating period.

We see that the two types of gratings, binary phase grating and multilevel phase grating, discussed in above sections could be used for efficient color separation to detect complementary color and fundamental color respectively for plane wave excitation. However, for binary phase grating, higher aspect ratio ($\frac{h}{fP}$) is required for efficient color separation, if we use lower grating period. This could impose the technological challenge to build such grating structure. For color separation grating based on Dammann's method, the diffraction efficiency decreases as the grating period decreases. These gratings can therefore only be used for imaging system with larger pixel sizes ($> 5\mu m$).

Overall, the basic idea is to introduce phase delay to desired wavelength, which is diffracted into central diffraction order of the grating. This concept still applies if we use single grating ridge and shine that ridge with focused light using micro lens. In case of single wavelength splitter similar to binary grating discussed above, the single grating ridge will introduce the phase delay (odd multiple of π) to incident wavelength which is then splitted into two components as it propagates toward detector. This concept has been applied by Seiji Nishiwaki et al to efficiently split colored light [15].

Figure D.8 shows the principle used by Seiji Nishiwaki et al to split the specific wavelengths by using single grating ridge. The micro lens collects the ambient light and focuses on the top of beam splitter. Figure D.8 (a) shows the single ridge used to split single wavelength (λ_1), where the height of splitter d , introduces the phase shift (δ) of π (or odd multiple of π). The designed phase shift is experienced by this wavelength propagating through the splitter and through the surrounding volume

of the splitter. It is therefore splitted into positive first and negative first order, whereas other wavelengths ($white - \lambda_1$) are transmitted into zero order. Using only two such grating ridge which splits blue and red light into first order, Seiji Nishiwaki et al was able to obtain Red, Green, Blue colors using specific color combination described in [15]. Figure D.8 (b) shows the single ridge with multiple levels similar to Dammann Grating. As the light enters the splitter with height d_1 and d , and width w and w_1 , the phase difference of δ_1 and δ is developed between the light propagating through the splitter and that propagating in the surrounding volume of the splitter. This splits the incidence white light into fundamental color components, Red, Green and Blue. The method employed by Seiji Nishiwaki et al is based on self-interference caused by the phase delay introduced by the splitter. This makes it different from the classical grating based light separation techniques.

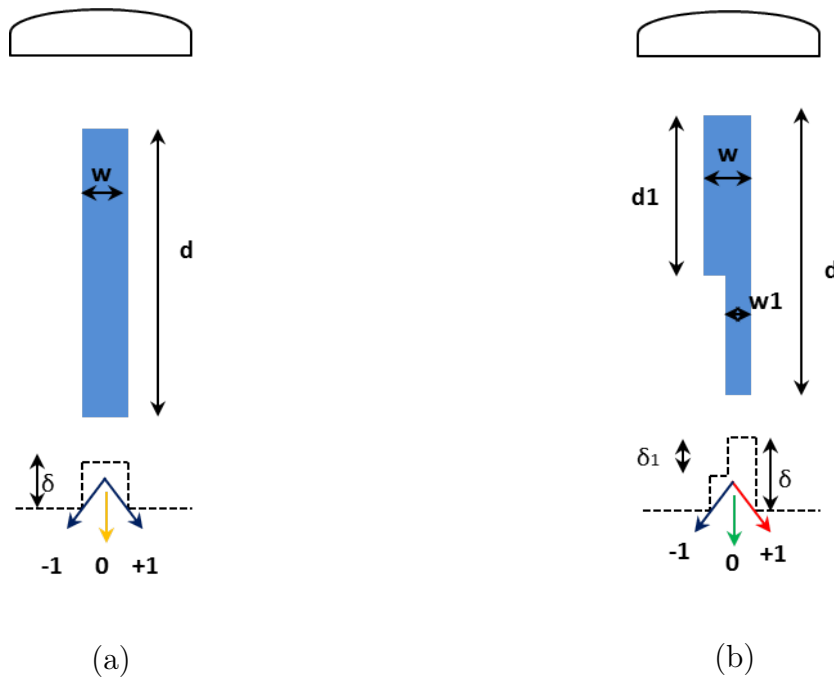


Figure D.8: (a) Single wave splitter (b) multiple wave splitter

The color separation techniques utilizing binary phase grating, multilevel phase grating and single ridge with focused light separates the light efficiently given the right design. The color separation efficiency is highest for normal incidence; however

there is a limit in incidence angle for which the colored light could be separated efficiently.

In figure D.9, we consider a single ridge of grating to calculate maximum acceptable incidence angle for efficient color separation, depending on ridge parameters. We consider the incidence and surrounding medium with refractive index n_i and splitter index of n_g . Within the small angle limit, we consider the light propagating from incidence medium to the splitter, which follows the Snell's law of refraction:

$$n_i \sin(\theta_{i_{max}}) = n_g \sin(\theta_d) \quad (\text{D.6})$$

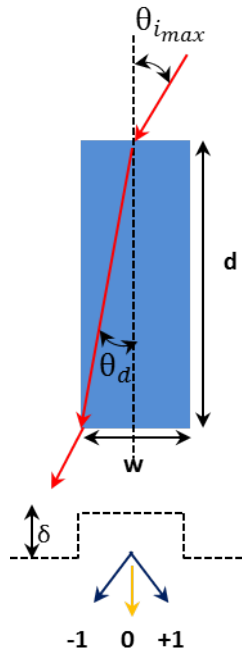


Figure D.9: Maximum incidence angle for efficient color separation

To separate the light with wavelength λ_1 using such splitter, the phase difference between the light propagating in the splitter and light propagating in surrounding should be odd multiple of π . This can only be achieved for the normal incidence. If the angle of incidence is not normal, the splitting could still be achieved for limited incidence angle, which maintains the phase difference close to π , for the

wave propagating in the splitter and in the surrounding of splitter. In figure D.9, we consider the angle of refraction θ_d such that the wave re-refracts to surrounding medium from the corner of bottom splitter-surrounding interface and maintain the phase difference close to π . Then using cosine law, we get:

$$\sin(\theta_d) = \frac{(w/2)}{\sqrt{(d^2 + w^2/4)}} \quad (\text{D.7})$$

Where w and d are the width and the height of splitter respectively used for analysis. Inserting equation D.7 in equation D.6 we get:

$$\theta_{i_{max}} = \sin^{-1} \left(\frac{n_g}{n_i} \frac{(w/2)}{\sqrt{(d^2 + w^2/4)}} \right) \quad (\text{D.8})$$

Equation D.8 gives the limit of maximum incidence angle which could split light efficiently within small angle approximation. The equation could be used to calculate the maximum acceptance incidence angle for the splitter which has sub-micron width. However for splitter with higher width the equation cannot be used to predict the acceptance angle. For the incidence angle larger than that predicted by equation D.8 the color separation equation given by equation D.1 does not strictly hold for designed wavelength and therefore light could not be splitted. For the binary grating with grating height $2880nm$ and grating width $400nm$, the maximum angle of incidence that could split the blue light into positive first and negative first diffraction order is, 6° . For the beam splitter with height $1200nm$ and width $280nm$ discussed in [15], the maximum incidence angle that can split blue light is $\sim 9^\circ$ which is in agreement with the results shown in [15]. Such kind of splitters can therefore be used only within small angle approximation, where splitter width is sub-micron in size. However, for practical imaging devices the acceptance angle should be as high as 30° . Using splitter based on phase delay and phase grating, the requirement of higher acceptance angle could not be achieved. It is therefore

necessary to find new structures which can separate light efficiently and has higher angular tolerance.

We present the binary phase grating and multilevel phase grating in prospect of color separation. We find that more rigorous analysis is required for the grating period below $5\mu m$ for both binary and multilevel phase grating used for color separation. Even though the colored light could be separated using Binary Phase grating and multilevel phase grating, larger buffer layer is required for efficient spatial separation of these lights. We further made a brief review about the splitter based on phase difference discussed by Seiji Nishiwaki et al in [15]. We see that all the splitters discussed in this chapter can only be used within small angle limit. The splitter ceases to work for higher incidence angle. In addition, these structures require higher aspect ratio (*height of splitter / width of splitter*) and larger buffer size between splitter and detector, which makes the color separation device more bulky. Higher aspect ratio required for efficient color separation could also impose technological challenges for fabrication. It is therefore necessary to find alternative structures which is more compact and which could separate the lights efficiently and has higher angular tolerance. Optical resonator system which has higher effective scattering (or absorbing) cross section area compared to physical cross section at resonance could collect more amount of light in small area (volume). It is interesting to explore such system as it could lead to compact and efficient light collection system.

Appendix E

Transfer Matrix Method

Transfer matrix method has been widely used [73, 74, 75, 76] to calculate reflectance and transmittance of multilayer structure. It is the method to solve Maxwell's equation in multilayer system subjected to uniform incidence electric field, in which the field is divided into forward component (transmitted) and backward component (reflected) as shown in figure E.1.

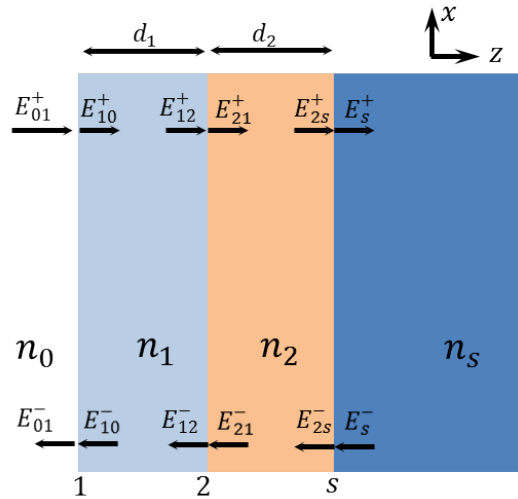


Figure E.1: Multilayer structure with complex refractive index. The electric field is divided to forward (with + sign) and backward (with - sign) components in TMM

In this section, we will calculate the reflection coefficient of multilayer coating on silicon using TMM model. For simplicity we show two layer dielectric stacks of

thickness d_1 and d_2 with refractive index n_1 and n_2 respectively on top of semi-infinite substrate with refractive index n_s as shown in figure E.1. We consider the TE polarized coherent light propagation to z-axis. At the interface, the fields in left- and right-hand side are related by Fresnel's coefficient, while the field in right-hand side of each layer experiences the phase shift relative to field in left-hand side, due to propagation through the film. We can therefore relate the electric field E_{01}^+ and E_{01}^- as shown in figure E.1 to electric fields E_s^+ and E_s^- . The total reflection from the multilayer can then be evaluated using $\frac{E_{01}^-}{E_{01}^+}$.

To find the matrix formulation of multilayer structure, we relate the fields in left- and right-hand side of interface S and gradually move towards interface 1. At the interfaces, the tangential components of field should be continuous, therefore we can write at interface S :

$$E_{2S}^+ + E_{2S}^- = E_S^+ + E_S^- \quad (\text{E.1})$$

$$n_2 (E_{2S}^+ - E_{2S}^-) = n_{si} (E_S^+ - E_S^-) \quad (\text{E.2})$$

Adding equations E.1 and E.2 we get,

$$\frac{2n_2}{n_2 + n_{si}} E_{2S}^+ = E_S^+ + \frac{n_2 - n_{si}}{n_2 + n_{si}} E_S^- \quad (\text{E.3})$$

Subtracting E.2 from E.1 we get,

$$\frac{2n_2}{n_2 + n_{si}} E_{2S}^- = \frac{n_2 - n_{si}}{n_2 + n_{si}} E_S^+ + E_S^- \quad (\text{E.4})$$

In above equations $\frac{2n_2}{n_2+n_{si}}$ and $\frac{n_2-n_{si}}{n_2+n_{si}}$ are the Fresnel coefficient of transmission and reflections for normal incidence. Representing these terms as $t_{2,S}$ and $r_{2,S}$ respectively and re-arranging the equations, we can find the matrix form to relate the fields in left- and right-hand side of interface S as:

$$\begin{pmatrix} E_{2S}^+ \\ E_{2S}^- \end{pmatrix} = \frac{1}{t_{2,S}} \begin{pmatrix} 1 & r_{2,S} \\ r_{2,S} & 1 \end{pmatrix} \begin{pmatrix} E_S^+ \\ E_S^- \end{pmatrix} \quad (\text{E.5})$$

At interface 2, we can write:

$$E_{12}^+ + E_{12}^- = E_{21}^+ + E_{21}^- \quad (\text{E.6})$$

$$n_1 (E_{12}^+ - E_{12}^-) = n_2 (E_{21}^+ - E_{21}^-) \quad (\text{E.7})$$

E_{21}^+ and E_{21}^- are related to E_{2S}^+ and E_{2S}^- respectively by following relation:

$$E_{21}^+ = E_{2S}^+ \exp(j\varphi_2) \quad (\text{E.8})$$

$$E_{21}^- = E_{2S}^- \exp(-j\varphi_2) \quad (\text{E.9})$$

Where $\varphi_2 = \frac{2\pi d_2 n_2}{\lambda}$ is the phase difference between the wave in interface 2 and S. Substituting E.8 and E.9 in relations E.6 and E.7 and following similar procedure we used to find the relation between the fields at interface S , we get:

$$\begin{pmatrix} E_{12}^+ \\ E_{12}^- \end{pmatrix} = \frac{1}{t_{1,2}} \begin{pmatrix} \exp(j\varphi_2) & r_{1,2} \exp(-j\varphi_2) \\ r_{1,2} \exp(j\varphi_2) & \exp(-j\varphi_2) \end{pmatrix} \begin{pmatrix} E_{2S}^+ \\ E_{2S}^- \end{pmatrix} \quad (\text{E.10})$$

Separating matrix coefficients for interface and thin film, equation E.10 can also be written as:

$$\begin{pmatrix} E_{12}^+ \\ E_{12}^- \end{pmatrix} = \frac{1}{t_{1,2}} \begin{pmatrix} 1 & r_{1,2} \\ r_{1,2} & 1 \end{pmatrix} \begin{pmatrix} \exp(j\varphi_2) & 0 \\ 0 & \exp(-j\varphi_2) \end{pmatrix} \begin{pmatrix} E_{2S}^+ \\ E_{2S}^- \end{pmatrix} \quad (\text{E.11})$$

Similarly for interface 1, the matrix form relating the fields can be derived as:

$$\begin{pmatrix} E_{01}^+ \\ E_{01}^- \end{pmatrix} = \frac{1}{t_{0,1}} \begin{pmatrix} 1 & r_{0,1} \\ r_{0,1} & 1 \end{pmatrix} \begin{pmatrix} \exp(j\varphi_1) & 0 \\ 0 & \exp(-j\varphi_1) \end{pmatrix} \begin{pmatrix} E_{12}^+ \\ E_{12}^- \end{pmatrix} \quad (\text{E.12})$$

Where $\varphi_1 = \frac{2\pi d_1 n_1}{\lambda}$ is the phase difference induced due to film thickness d_1 . Using relations E.12, E.11 and E.5, the fields E_s^+ and E_s^- can be related to E_{01}^+ and E_{01}^- as:

$$\begin{pmatrix} E_{01}^+ \\ E_{01}^- \end{pmatrix} = I_{0,1} P_1 I_{1,2} P_2 I_{2,S} \begin{pmatrix} E_s^+ \\ E_s^- \end{pmatrix} \quad (\text{E.13})$$

where,

$$I_{0,1} = \frac{1}{t_{0,1}} \begin{pmatrix} 1 & r_{0,1} \\ r_{0,1} & 1 \end{pmatrix}$$

$$I_{1,2} = \frac{1}{t_{1,2}} \begin{pmatrix} 1 & r_{1,2} \\ r_{1,2} & 1 \end{pmatrix}$$

$$I_{2,S} = \frac{1}{t_{2,S}} \begin{pmatrix} 1 & r_{2,S} \\ r_{2,S} & 1 \end{pmatrix}$$

$$P_1 = \begin{pmatrix} \exp(j\varphi_1) & 0 \\ 0 & \exp(-j\varphi_1) \end{pmatrix}$$

$$P_2 = \begin{pmatrix} \exp(j\varphi_2) & 0 \\ 0 & \exp(-j\varphi_2) \end{pmatrix}$$

We define system transfer matrix $M_{0,S}$ as:

$$M_{0,S} = I_{0,1}P_1I_{1,2}P_2I_{2,S} = \begin{pmatrix} M_{11} & M_{12} \\ M_{21} & M_{22} \end{pmatrix} \quad (\text{E.14})$$

The matrix transformation can be generalized for multiple layer system with N different layers of thin film and $N+1$ interface as:

$$\begin{pmatrix} E_{01}^+ \\ E_{01}^- \end{pmatrix} = I_{0,1}P_1I_{1,2}P_2I_{2,S} \dots P_N I_{N,N+1} \begin{pmatrix} E_{N+1}^+ \\ E_{N+1}^- \end{pmatrix} = \begin{pmatrix} M_{11} & M_{12} \\ M_{21} & M_{22} \end{pmatrix} \begin{pmatrix} E_{N+1}^+ \\ E_{N+1}^- \end{pmatrix} \quad (\text{E.15})$$

Using elements of system transfer matrix, we can calculate the reflection and transmission coefficients as:

$$r = \frac{E_{01}^-}{E_{01}^+} = \frac{M_{21}}{M_{11}} \quad (\text{E.16})$$

$$t = \frac{E_S^+}{E_{01}^+} = \frac{1}{M_{11}} \quad (\text{E.17})$$

Having calculated the reflection and transmission coefficient for multilayer system, the reflectance from the multilayer structure and transmittance to the substrate can then be calculated using relations:

$$R = |r|^2 \quad (\text{E.18})$$

$$T = \frac{n_S}{n_0} |t|^2 \quad (\text{E.19})$$

It can be seen that the reflection from the multilayer system depends on the layer thickness and the refractive index of each layers used. Using such multilayer system on top of silicon we can therefore design the antireflection coating for different wavelengths.

Bibliography

- [1] Peter B Catrysse and Brian A Wandell. Integrated color pixels in 0.18- μm complementary metal oxide semiconductor technology. *JOSA A*, 20(12):2293–2306, 2003.
- [2] Charlie Koechlin, Patrick Bouchon, Fabrice Pardo, Julien Jaeck, Xavier Lafosse, Jean-Luc Pelouard, and Riad Haïdar. Total routing and absorption of photons in dual color plasmonic antennas. *Applied Physics Letters*, 99(24):–, 2011.
- [3] J. Le Perchec, Y. Desieres, N. Rochat, and R. Espiau de Lamaestre. Sub-wavelength optical absorber with an integrated photon sorter. *Applied Physics Letters*, 100(11):–, 2012.
- [4] Yijie Huo, Christian C Fesenmaier, and Peter B Catrysse. Microlens performance limits in sub- $2\mu\text{m}$ pixel cmos image sensors. *Optics express*, 18(6):5861–5872, 2010.
- [5] A Rogalski. Optical detectors for focal plane arrays. *OPTOELECTRONICS REVIEW*, 12(2):221–246, 2004.
- [6] Antoni Rogalski. Progress in focal plane array technologies. *Progress in Quantum Electronics*, 36(2):342–473, 2012.
- [7] HIROSHI Iwai. Roadmap for 22nm and beyond. *Microelectronic Engineering*, 86(7):1520–1528, 2009.

- [8] Albert Theuwissen. Cmos image sensors: State-of-the-art and future perspectives. In *Solid State Circuits Conference, 2007. ESSCIRC 2007. 33rd European*, pages 21–27. IEEE, 2007.
- [9] Rino Marinelli and Elia Palange. Optical performances of lensless sub-2micron pixel for application in image sensors. *Progress In Electromagnetics Research B*, 31:1–14, 2011.
- [10] Christian C Fesenmaier, Yijie Huo, and Peter B Catrysse. Optical confinement methods for continued scaling of cmos image sensor pixels. *Optics express*, 16(25):20457–20470, 2008.
- [11] Ting Chen, Peter B Catrysse, Abbas El Gamal, and Brian A Wandell. How small should pixel size be? In *Electronic Imaging*, pages 451–459. International Society for Optics and Photonics, 2000.
- [12] RK Bhan, RS Saxena, CR Jalwania, and SK Lomash. Uncooled infrared microbolometer arrays and their characterisation techniques (review paper). *Defence Science Journal*, 59(6):580–589, 2009.
- [13] Antoni Rogalski. Infrared detectors: status and trends. *Progress in quantum electronics*, 27(2):59–210, 2003.
- [14] JungChak Ahn, Bumsuk Kim, Kyungho Lee, Sangjun Choi, Heegeun Jeong, Hongki Kim, Goto Hiroshige, Chi-Young Choi, and Duckhyung Lee. Snr metric and crosstalk in color image sensor of small size pixel. In *VLSI Technology, Systems, and Applications (VLSI-TSA), 2013 International Symposium on*, pages 1–2. IEEE, 2013.
- [15] Seiji Nishiwaki, Tatsuya Nakamura, Masao Hiramoto, Toshiya Fujii, and Masaki Suzuki. Efficient colour splitters for high-pixel-density image sensors. *Nature Photonics*, 7(3):240–246, 2013.

- [16] Eric Laux, Cyriaque Genet, Torbjorn Skauli, and Thomas W Ebbesen. Plasmonic photon sorters for spectral and polarimetric imaging. *Nature Photonics*, 2(3):161–164, 2008.
- [17] Timur Shegai, Si Chen, Vladimir D Miljković, Gülis Zengin, Peter Johansson, and Mikael Käll. A bimetallic nanoantenna for directional colour routing. *Nature communications*, 2:481, 2011.
- [18] J. Le Perchec, Y. Desieres, and R. Espiau de Lamaestre. Plasmon-based photosensors comprising a very thin semiconducting region. *Applied Physics Letters*, 94(18):–, 2009.
- [19] Patrick Bouchon, Charlie Koechlin, Fabrice Pardo, Riad Haïdar, and Jean-Luc Pelouard. Wideband omnidirectional infrared absorber with a patchwork of plasmonic nanoantennas. *Opt. Lett.*, 37(6):1038–1040, Mar 2012.
- [20] Tae Joon Seok, Arash Jamshidi, Myungki Kim, Scott Dhuey, Amit Lakhani, Hyuck Choo, Peter James Schuck, Stefano Cabrini, Adam M Schwartzberg, Jeffrey Bokor, et al. Radiation engineering of optical antennas for maximum field enhancement. *Nano letters*, 11(7):2606–2610, 2011.
- [21] Elizabeth J Smythe, Michael D Dickey, Jiming Bao, George M Whitesides, and Federico Capasso. Optical antenna arrays on a fiber facet for in situ surface-enhanced raman scattering detection. *Nano letters*, 9(3):1132–1138, 2009.
- [22] Dongxing Wang, Wenqi Zhu, Yizhuo Chu, and Kenneth B Crozier. High directivity optical antenna substrates for surface enhanced raman scattering. *Advanced Materials*, 24(32):4376–4380, 2012.
- [23] Lukas Novotny. Effective wavelength scaling for optical antennas. *Physical Review Letters*, 98(26):266802, 2007.

- [24] Rafif E Hamam, Aristeidis Karalis, JD Joannopoulos, and Marin Soljačić. Coupled-mode theory for general free-space resonant scattering of waves. *Physical review A*, 75(5):053801, 2007.
- [25] Xianliang Liu, Tatiana Starr, Anthony F. Starr, and Willie J. Padilla. Infrared spatial and frequency selective metamaterial with near-unity absorbance. *Phys. Rev. Lett.*, 104:207403, May 2010.
- [26] nannan wu, Huiping Tian, Hongzhan Liu, and Yuefeng Ji. Infrared perfect metamaterial absorber and its potential application as strain sensor. In *Asia Communications and Photonics Conference 2013*, page AW4J.8. Optical Society of America, 2013.
- [27] Wei Ma, Yongzheng Wen, and Xiaomei Yu. Broadband metamaterial absorber at mid-infrared using multiplexed cross resonators. *Opt. Express*, 21(25):30724–30730, Dec 2013.
- [28] Hao Wang and Liping Wang. Perfect selective metamaterial solar absorbers. *Opt. Express*, 21(S6):A1078–A1093, Nov 2013.
- [29] Michael G. Nielsen, Dmitri K. Gramotnev, Anders Pors, Ole Albrektsen, and Sergey I. Bozhevolnyi. Continuous layer gap plasmon resonators. *Opt. Express*, 19(20):19310–19322, Sep 2011.
- [30] Cristian Ciraci, J Britt Lassiter, Antoine Moreau, and David R Smith. Quasi-analytic study of scattering from optical plasmonic patch antennas. *Journal of Applied Physics*, 114(16):163108, 2013.
- [31] William L. Barnes, Alain Dereux, and Thomas W. Ebbesen. Surface plasmon subwavelength optics. *Nature*, 424:824–830, 2003.
- [32] Stefan Alexander Maier. *Plasmonics: Fundamentals and Application*. Springer, 2007.

- [33] Y. Todorov, L. Tosetto, J. Teissier, A. M. Andrews, P. Klang, R. Colombelli, I. Sagnes, G. Strasser, and C. Sirtori. Optical properties of metal-dielectric-metal microcavities in the thz frequency range. *Opt. Express*, 18(13):13886–13907, Jun 2010.
- [34] Cheryl Feuillet-Palma, Yanko Todorov, Robert Steed, Angela Vasanelli, Giorgio Biasiol, Lucia Sorba, and Carlo Sirtori. Extremely sub-wavelength thz metal-dielectric wire microcavities. *Opt. Express*, 20(27):29121–29130, Dec 2012.
- [35] M Zohrabi. Electric field enhancement of gold tip optical antenna with special geometry.
- [36] Vladimir M. Shalaev, Wenshan Cai, Uday K. Chettiar, Hsiao-Kuan Yuan, Andrey K. Sarychev, Vladimir P. Drachev, and Alexander V. Kildishev. Negative index of refraction in optical metamaterials. *Opt. Lett.*, 30(24):3356–3358, Dec 2005.
- [37] Hermann A Haus. *Waves and fields in optoelectronics*, volume 464. Prentice-Hall Englewood Cliffs, NJ, 1984.
- [38] Tae Joon Seok. *Engineering Optical Antenna for Efficient Local Field Enhancement*. PhD thesis, UC-Berkeley, 2012.
- [39] Kartik Srinivasan, Matthew Borselli, Oskar Painter, Andreas Stintz, and Sanjay Krishna. Cavity q, mode volume, and lasing threshold in small diameter algaas microdisks with embedded quantum dots. *Opt. Express*, 14(3):1094–1105, Feb 2006.
- [40] Filippo Capolino. *Theory and phenomena of metamaterials*. CRC Press, 2009.
- [41] Edward D Palik. *Handbook of optical constants of solids*, volume 3. Academic press, 1998.

- [42] Anne-Laure Fehrembach, Daniel Maystre, and Anne Sentenac. Phenomenological theory of filtering by resonant dielectric gratings. *J. Opt. Soc. Am. A*, 19(6):1136–1144, Jun 2002.
- [43] TV Raziman and Olivier JF Martin. Polarisation charges and scattering behaviour of realistically rounded plasmonic nanostructures. *Optics express*, 21(18):21500–21507, 2013.
- [44] Rong-Jer Lee, Jr-Cheng Fan, Tzong-Shing Cheng, and Jung-Lung Wu. Pigment-dispersed color resist with high resolution for advanced color filter application. In *Information Display, 1999. ASID '99. Proceedings of the 5th Asian Symposium on*, pages 359–363, 1999.
- [45] U. PALANCHOKE, S. BOUTAMI, and J. Hazart. Spectral filtering device in the visible and infrared ranges, February 20 2014. US Patent App. 13/950,691.
- [46] Romain Girard-Desprolet, Salim Boutami, Sandrine Lhostis, and Guy Vitrant. Angular and polarization properties of cross-holes nanostructured metallic filters. *Opt. Express*, 21(24):29412–29424, Dec 2013.
- [47] Guangyuan Si, Yanhui Zhao, Jiangtao Lv, Mengqian Lu, Fengwen Wang, Hailong Liu, Ning Xiang, Tony Jun Huang, Aaron J. Danner, Jinghua Teng, and Yan Jun Liu. Reflective plasmonic color filters based on lithographically patterned silver nanorod arrays. *Nanoscale*, 5:6243–6248, 2013.
- [48] Qin Chen and David R. S. Cumming. High transmission and low color cross-talk plasmonic color filters using triangular-lattice hole arrays in aluminum films. *Opt. Express*, 18(13):14056–14062, Jun 2010.
- [49] L.J. Guo and T. Xu. Display device having plasmonic color filters and photovoltaic capabilities, October 1 2013. US Patent 8,547,504.

- [50] H Dammann. Color separation gratings. *Applied Optics*, 17(15):2273–2279, 1978.
- [51] K Knop. Diffraction gratings for color filtering in the zero diffraction order. *Applied optics*, 17(22):3598–3603, 1978.
- [52] Torbjorn Skauli Eric Laux, Cyriaque Genet and Thomas W. Ebbesen. Plasmonic photon sorters for spectral and polarimetric imaging. *Nature Photonics*, 2:161–164, Feb 2008.
- [53] Ujwol Palanchoke, Vladislav Jovanov, Henning Kurz, Philipp Obermeyer, Helmut Stiebig, and Dietmar Knipp. Plasmonic effects in amorphous silicon thin film solar cells with metal back contacts. *Optics express*, 20(6):6340–6347, 2012.
- [54] Peter B Catrysse and Brian A Wandell. Optical efficiency of image sensor pixels. *JOSA A*, 19(8):1610–1620, 2002.
- [55] Dale C Flanders. Submicrometer periodicity gratings as artificial anisotropic dielectrics. *Applied Physics Letters*, 42(6):492–494, 1983.
- [56] Rong-Chung Tyan, Atul A Salvekar, Hou-Pu Chou, Chuan-Cheng Cheng, Axel Scherer, Pang-Chen Sun, Fang Xu, and Yeshayahu Fainman. Design, fabrication, and characterization of form-birefringent multilayer polarizing beam splitter. *JOSA A*, 14(7):1627–1636, 1997.
- [57] Philippe Lalanne and G Michael Morris. Antireflection behavior of silicon sub-wavelength periodic structures for visible light. *Nanotechnology*, 8(2):53, 1997.
- [58] Y Kanamori, M Sasaki, and K Hane. Broadband antireflection gratings fabricated upon silicon substrates. *Optics letters*, 24(20):1422–1424, 1999.
- [59] SM Rytov. Electromagnetic properties of a finely stratified medium. *SOVIET PHYSICS JETP-USSR*, 2(3):466–475, 1956.

- [60] E Popov, L Mashev, and D Maystre. Theoretical study of the anomalies of coated dielectric gratings. *Journal of Modern Optics*, 33(5):607–619, 1986.
- [61] Ildar F Salakhutdinov, Vladimir A Sychugov, Alexander V Tishchenko, Boris A Usievich, Olivier Parriaux, and Fedor A Pudonin. Anomalous light reflection at the surface of a corrugated thin metal film. *IEEE journal of quantum electronics*, 34(6):1054–1060, 1998.
- [62] L Pilozzi, D Schiumarini, N Tomassini, and A D’Andrea. Giant reflection band and anomalous negative transmission in a resonant dielectric grating slab: Application to a planar cavity. *Physical Review B*, 86(4):045301, 2012.
- [63] E Popov and L Mashev. Diffraction anomalies of coated dielectric gratings in conical diffraction mounting. *Optics communications*, 59(5):323–326, 1986.
- [64] Constantine A Balanis. *Antenna theory: analysis and design*. John Wiley & Sons, 2012.
- [65] Arthur D Yaghjian and Steven R Best. Impedance, bandwidth, and Q of antennas. *Antennas and Propagation, IEEE Transactions on*, 53(4):1298–1324, 2005.
- [66] Lan Jen Chu. Physical limitations of omni-directional antennas. *Journal of applied physics*, 19(12):1163–1175, 1948.
- [67] David R Jackson and Nicolaos G Alexopoulos. Simple approximate formulas for input resistance, bandwidth, and efficiency of a resonant rectangular patch. *IEEE Transactions on Antennas and Propagation*, 39(3):407–410, 1991.
- [68] Stefan Alexander Maier. *Plasmonics: Fundamentals and Applications: Fundamentals and Applications*. Springer, 2007.
- [69] Wai-Hon Lee. High efficiency multiple beam gratings. *Applied optics*, 18(13):2152–2158, 1979.

- [70] FB McCormick. Generation of large spot arrays from a single laser beam by multiple imaging with binary phase gratings. *Optical Engineering*, 28(4):284299–284299, 1989.
- [71] Mayumi Nagayoshi, Keiko Oka, Werner Klaus, Yuki Komai, and Kashiko Kodate. Design and evaluation of color separation grating using rigorous coupled wave analysis. *Japanese journal of applied physics*, 45(8S):6670, 2006.
- [72] Ben Layet, Iain G Cormack, and Mohammad R Taghizadeh. Stripe color separation with diffractive optics. *Applied optics*, 38(35):7193–7201, 1999.
- [73] M Claudia Tropicovsky, Adrian S Sabau, Andrew R Lupini, and Zhenyu Zhang. Transfer-matrix formalism for the calculation of optical response in multilayer systems: from coherent to incoherent interference. *Optics express*, 18(24):24715–24721, 2010.
- [74] OS Heavens. Optical properties of thin solid films. 1965. *Dover, New York*.
- [75] Tianrong Zhan, Xi Shi, Yunyun Dai, Xiaohan Liu, and Jian Zi. Transfer matrix method for optics in graphene layers. *Journal of Physics: Condensed Matter*, 25(21):215301, 2013.
- [76] Koji Ohta and Hatsuo Ishida. Matrix formalism for calculation of electric field intensity of light in stratified multilayered films. *Applied optics*, 29(13):1952–1959, 1990.